

Reconstruction of group-IV semiconductor surfaces: Origin, energetics and consequences

Dissertation

zur Erlangung des akademischen Grades
doctor rerum naturalium (Dr. rer. nat.)

vorgelegt dem Rat der Physikalisch-Astronomischen Fakultät
der Friedrich-Schiller-Universität Jena

von Dipl.-Ing. Andrey Stekolnikov
geboren am 25. Januar 1977 in Minsk

Gutachter:

1. Prof. Dr. Friedhelm Bechstedt, Jena.
2. Prof. Dr. GP Srivastava, Exeter.
3. Prof. Dr. Peter Krüger, Münster.

Tag der letzten Rigorosumsprüfung: 22. Februar 2005.

Tag der öffentlichen Verteidigung: 19. April 2005.

To my family

Contents

1	Introduction	3
2	Theoretical background and numerical approaches	12
2.1	Many-body problem and steps for the solution	12
2.2	Density-functional theory	13
2.2.1	Hohenberg-Kohn theorem	13
2.2.2	Kohn-Sham method	14
2.2.3	Local density approximation and limitations	15
2.3	Total energy and forces	17
2.4	Plane-wave expansion	17
2.5	Pseudopotentials	18
2.6	Implementation and minimization algorithms	20
2.7	Thermodynamical relations for surfaces	21
2.7.1	Thermodynamical potentials and modification for surfaces	21
2.7.2	Surface energy	23
2.7.3	Wulff construction	24
2.8	Modeling of surfaces	25
2.9	Two-dimensional Brillouin zones	29
3	Low-index surfaces I – (100) and (111)	32
3.1	(100) surface orientation	32
3.2	(111) surface orientation	35
3.2.1	Energetics	35
3.2.2	Geometry	38
3.2.3	Band structures	40
4	High-index surfaces – (113)	44
4.1	Reconstruction models and structural parameters	44
4.2	Energetics and geometries	46
4.3	Band structures and electronic states	49
4.4	STM images	56
5	Low-index surfaces II – (110)	58
5.1	Translational symmetry of (110) 16×2 surfaces	58
5.2	Bond-rotation/bond-contraction relaxation mechanism	58
5.3	Adatoms	64
5.4	Adclusters	68

5.5	Missing rows and adatoms	69
5.6	Tetramers and interstitials	70
6	Shape of free and constrained crystallites:	
	Influence of surface energies	76
6.1	Absolute Surface Energies	76
6.1.1	Dependence on orientation and reconstruction	76
6.1.2	Extrapolation	78
6.2	Equilibrium Crystal Shape	78
6.2.1	Shape of diamond crystallites	78
6.2.2	Shape of Si and Ge crystallites	80
6.3	Shape of Pyramidal Nanocrystals	81
6.3.1	Total energy and surface energy	81
6.3.2	Deformation of pyramids	82
7	Summary and conclusions	86
	Bibliography	91
	Publications	99
	Zusammenfassung	100

Chapter 1

Introduction

Due to the extreme downscaling in modern semiconductor technology one has to deal with elements in nanometer range. A compromise between performance and cost requires a transformation of microelectronics to nanoelectronics. The definition of “nanotechnology” covers multidisciplinary interest to objects and means working at an atomic, molecular or supramolecular level, in the length scale range of approximately 1–100 nm, in order to understand and create materials, devices and systems with fundamentally new properties and functions because of their small characteristic lengths. Silicon as the basic material of microelectronics provides the ideal platform for the integration of nanotechnology. The evolution is based on continued nanoscaling of Complementary Metal-Oxide-Semiconductor (CMOS) technology which includes materials and lithography innovations at this stage. New architectures and structures should be implemented to a non-classical CMOS technology and finally transition to novel devices could take place (see e.g. <http://www.intel.com>).

The request of transmission of information between electronic elements in one integrated system as fast, and as cheap as possible led to intensive investigations of possible silicon-based optoelectronic devices. Optoelectronic integration on a chip, which is based on silicon photonics, can be characterized as the utilization of silicon-based materials for the generation (electrical-to-optical conversion), guidance, control, and detection (optical-to-electrical conversion) of light to communicate information over certain distances. The difficulty in making a silicon light emitter arises from the indirect band-gap of the material. This indirect band gap results in radiative (light emitting) decay being less likely compared to other non-radiative (e.g., Auger recombination) channels, and thus in a less-efficient corresponding light emission. Forming a laser or even a light emitter from silicon is, therefore, difficult, although not impossible. Research worldwide has shown light emission from silicon and silicon-based materials by a wide variety of different methods. Intensive photoluminescence has been demonstrated for textured bulk Si [1], fabricated nano-scale Si [2], porous Si [3], crystalline Si with defects [4] or doped by exotic ions [5].

One approach to enhance the efficiency of light emission in silicon is to reduce the other non-radiative mechanisms for electron-hole recombination and to increase the oscillator strength of the lowest optical transitions. This can be done by restricting carrier diffusion to the non-radiative recombination centers in the lattice. The confinement also increases the probability

for radiative transitions and hence increases the light emission efficiency. The achievement of carrier confinement means the use of nanocrystals which is compatible to Very Large Scale Integration (VLSI). Silicon nanocrystals suspended in silicon-rich oxide matrices restrict carrier movement while still allowing electrical pumping [6]. Pavesi et al. have shown optical gain in these structures [2]. Franzo et al. have doped silicon nanocrystals with erbium to achieve electroluminescence (EL) in the infrared region of the optical spectrum [7].

In recent years Ge/Si systems have attracted great attention. Ge has only 4.2 % lattice mismatch, and is chemically similar, to Si. Carrier confinement and efficient light emission have been achieved by Ge (Ge/Si) quantum dots [8]. Detection of light for wavelengths typically used for optical communications (1.31–1.55 μm) is also not possible in bulk silicon, which is transparent in this region. Therefore, SiGe detectors have been developed in order to push the responsivity out to longer wavelengths to achieve efficient operation.

One of the fascinating problems concerns the equilibrium shape of nanocrystallites fabricated from germanium and silicon or, in general, the shape of nanocrystallites grown epitaxially on certain substrates. This topic is strongly related to the formation of self-assembled islands, or quantum dots, during epitaxial growth [9–11]. The results of self-assembly and possible Ostwald ripening are characterized by several distinct island shapes, size distributions, and island arrangements. There is an understanding of island nucleation [12] and subsequent coarsening (Ostwald ripening) [13] for the simple case where islands grow with a fixed shape. However, the island shape, the change in the shape of growing islands, and the precise nature of shape transitions are the subject of intense discussions [14]. Theories of elastic relaxation at surfaces predict the formation and stabilization of periodic structures with defined sizes [15]. In these analyses, the island size is determined by balancing the elastic energy gain associated with the relaxation at the phase boundary against the energy cost of creating the boundary. However, it is difficult to establish the link between stress and morphology, because key kinetic or thermodynamic parameters necessary for a quantitative interpretation are often unknown. Furthermore, the microscopic rearrangement of the atoms on the surfaces to minimize the local energies may play an important role [16].

A typical example for the island formation is the Stranski-Krastanov (SK) growth mode [11, 17] of Ge on Si(100) substrates. The growth of a strained wetting layer, as thick as 3–4 monolayers, is followed by the formation of three-dimensional islands. Eaglesham and Cerullo [18] have made the surprising discovery that in the initial stages of SK growth, the islands can be coherent, i.e., dislocation-free. Only later, as the islands grow in size, dislocations develop. The coherent islands can be up to ~ 150 nm in size and ~ 50 nm high. Before the appearance of micrometer-sized Ge crystallites, an intermediate phase of metastable clusters has been also observed [19]. Scanning tunneling microscopy (STM) at low Ge coverage has shown that small islands (so-called hut clusters [19] or pyramids [20]) with rectangular or square base are formed by $\{501\}$ facets. Phase transitions take place when larger islands with a higher aspect ratio, so-called domes [21, 22], appear at higher Ge coverages and display a multifaceted surface including $\{311\}$ facets. Typical Ge nanocrystals with both pyramid and dome shapes grown on Si(100) examined by STM are shown in Fig. 1.1 (from Ref. [21]). The situation may be more complicated due to intermixing. Recently, it has been shown [23] that domes contain a

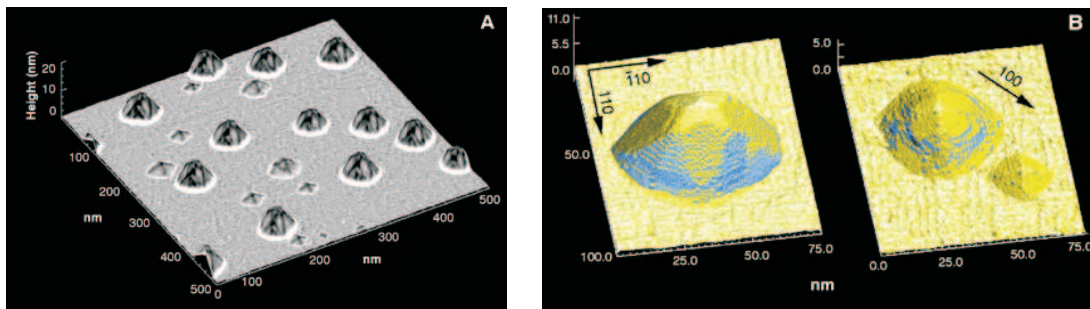


Figure 1.1 STM topograph of Ge nanocrystals on a Si(001) surface showing both pyramids and domes (from Ref. [21]).

Si-rich core covered by a Ge-rich shell. In any case nanocrystals are bounded by facets which correspond to certain surface orientations. Faceted islands have been also grown on Si(111) [24] and SiC(0001) substrates [25], where $\{113\}$ facets are quite pronounced.

The situation is less clear for Si nanocrystals. Micrometer-scale Si droplets have been formed on a Si(111) substrate by photolithography [26]. They have been used to determine the equilibrium shape of a small Si crystal. Well-characterized $\{111\}$ and $\{311\}$ facets exist on the nanocrystal surface. They are separated by rounded regions that display a tangential merging into the facets. Bermond et al. [26] found that the surface energy increases from $\{100\}$ to $\{111\}$ via a $\{311\}$ plane, and has local minima at the surfaces $\{111\}$, $\{311\}$, $\{110\}$, and $\{100\}$. These results are in qualitative agreement with measurements [27] of small voids in a Si crystal which indicate the existence of the same facets. Pyramidal Si nanocrystals can be selectively grown on Si(100) windows in ultrathin SiO₂ films [28–31]. These Si pyramids possess four equivalent facets of the types $\{111\}$, $\{311\}$ or even $\{911\}$ and $\{1\bar{3}11\}$. Using a micro-shadow mask technology or nonplanar prepatterned Si(100) substrates, the self-assembling Molecular Beam Epitaxy (MBE) growth also leads to nanometer-scale features [32]. Depending on the growth parameters, pyramid-like tips or long wedges are formed. The sidewalls are free-standing $\{111\}$ and $\{311\}$ facets.

One more group-IV material, diamond (tetrahedral carbon), possesses extraordinary properties, which suggest a broad range of scientific and technological applications. Diamond is the hardest and stiffest material known, has the highest room temperature (RT) thermal conductivity and one of the lowest thermal expansion coefficients of known materials. It is radiation-hard and chemically inert to most acidic and basic reagents. Diamond has a large band gap, hence electrical devices can work at higher temperatures (HTs) than Si. Unfortunately, due to the high cost and preparation difficulties, the applications of natural and synthetic diamond have been limited in comparison to its great potential [33].

The many ways in which diamonds have been synthesized are clues to the conditions under which diamonds form naturally. Diamond is the stable carbon phase at pressure $p > 5$ GPa. Industrial-scale production of diamond starts from amorphous carbon or graphite at HT (1200–1400 °C) and high pressure (HP) (5 to 7 GPa). Diamond morphologies vary as a function of temperature at constant pressure (for example, 6 GPa): Octahedrons form preferentially at HTs

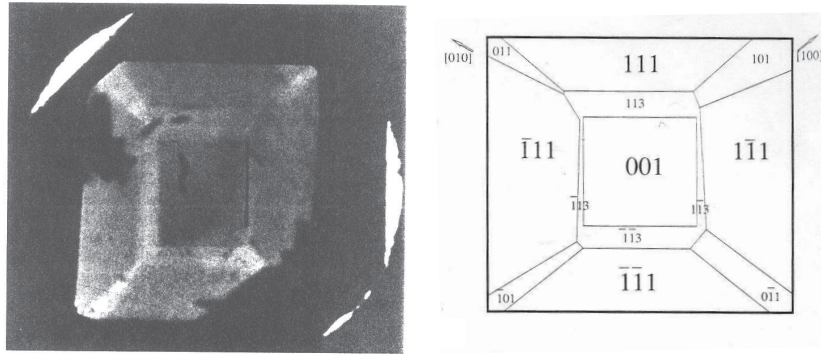


Figure 1.2 Micrograph of HP-HT synthetic diamond (left) and map of growth sectors (right) (from Ref. [34]).

1500 to 1600 °C, cubo-octahedrons at 1350 to 1500 °C, and cubes at <1300 °C. Small synthetic diamonds grown by HT-HP methods have major growth sectors of {100} and {111} type and some minor sectors of {110} and {311} (see Fig. 1.2) [34]. The most recent industrial method is to form diamond through Chemical Vapor Deposition (CVD). In this process, a thin (nanometer to micrometer) metastable diamond film is formed on metal substrates from methane (CH_4) or other hydrocarbons at low pressure (<1 Pa) and at HT (1000 °C), in the presence of excess hydrogen. The morphology of diamond particles grown by HT-CVD is dominated by {100} and {111} facets (see Ref. [35] and references therein). In addition, facets of the types {110} and {311} appear between those with common orientation. However, it is difficult to conclude that {311} facets exist in a steady state. Using CVD also diamond nanocrystallites can be grown partially epitaxially or perfectly heteroepitaxially on stepped Si substrates with [110] orientation [36]. An exact determination of the facet orientations of the crystallites with 2–6 nm size is, however, hardly possible.

The absolute value of the surface free energy of a crystalline solid is one of the most important fundamental quantities which characterizes a large number of basic and applied phenomena. Among them are crystal growth, surface faceting, epitaxy and stability of thin layers, and the shape of small crystallites. In particular the construction of the equilibrium crystal shape (ECS) requires the complete determination of the surface free energy γ as a function of the surface orientation \mathbf{n} . Despite its significance, a complete and well-accepted set of corresponding experimental data of group-IV materials is not available. There are only few experimental data for surface free energies and only for Si [27]. In general, the experimental determination of γ remains a challenge [37]. Theoretical data, in particular derived from highly-precise, parameter-free total-energy calculations, are of great importance. However, calculated absolute surface energies are also rare.

Due to surface formation, bonds are cut, what requires energy. One may expect that the resulting surface energy γ is proportional to the dangling-bond density. However, in order to reduce this energy surface atoms relax which leads to a certain distortion of the ideal bulk-like positions. Such processes take place in particular on metal surfaces. The situation for semiconductors is more complicated due to the tendency of significant surface reconstructions. In

tetrahedrally bonded semiconductors, such as diamond, Si, and Ge strong directional bonds are present what leads to dramatic effects. Nearly all surface orientations of group-IV elements observed experimentally possess reconstructions which give rise to a two-dimensional translational symmetry with unit cells much larger than 1×1 , i.e., that of a surface according to the bulk termination. It is required to understand and determine the precise atomic geometry of a given reconstruction for a certain orientation depending on the material.

Calculations of absolute surface energies are mainly restricted to semi-empirical methods as the tight-binding (TB) approach [38] or the use of classical interaction potentials [39, 40]. In most cases they do not consider surface reconstructions. The fully quantum-mechanical treatment usually gives relative surface energies for different reconstructions but one and the same orientation. Only for low-index diamond surfaces there are comparative studies which give absolute surface energies [41, 42]. Moreover, reconstruction elements which appear on group-IV surfaces are still under debate even considering low-index surfaces. The situation is really complicated for Si and Ge surfaces. The origin and the driving forces of reconstructions are not always understood. For that reason the main part of the present work is devoted to comprehensive studies of diamond, Si and Ge surfaces including low-index (100), (111), (110) and high-index (113) ones. We try to answer the question as to why surfaces of group-IV elements behave differently. There are no comprehensive comparative studies of the materials for different surface orientations considering reconstructions observed experimentally. As a consequence, surface energies have not been determined and the energy dependences of the surface reconstructions and orientations for these important semiconductors have not been derived.

Based on well converged energies of the most-frequently observed (100), (111), (110), and (113) surfaces of group-IV semiconductors one may construct the ECSs using the Wulff construction [43]. However, Wulff constructions using theoretical or reliable experimental data for γ have not been presented so far for diamond, Si, and Ge. Yet important conclusions can be drawn from the equilibrium shapes of the crystals. We attack this problem assuming large facets. Therefore surface reconstructions are important. The stability evaluation of a certain surface orientation gives information about tendencies for faceting etc. For instance, the question has to be answered whether the ECS of diamond exhibits only cleavage orientations corresponding to {111} facets? Another one is if there are tendencies for high-index surfaces to contribute to the ECSs of Si and Ge?

In contrast to free crystallites the actual three-dimensional shape of a nanocrystal grown on a certain substrate depends on many thermodynamic and kinetic aspects or growth conditions including strain, alloying, temperature, number of adsorbate atoms, wetting layer, and interface. For nanocrystallites grown (hetero)epitaxially, strain may play a dominant role for the crystallite shape [9, 44]. Nevertheless, interesting trends can already be derived studying the influence of surface energies. We restrict the discussions of the shapes on the latter. Despite such a simplified picture it could describe the trend for crystallites to be deformed if a certain base orientation and a certain shape are chosen. Pyramid shapes observed during the growth should be considered and compared with ECSs (i.e., shapes of free crystallites).

The most powerful tools to study the energetics and the atomic geometry of solids and their surfaces are *ab-initio* methods, particularly using the Density-Functional Theory (DFT)

for total-energy calculations. Parameter-free quantum-mechanical calculations can give a precise microscopic picture of systems in the ground state. The true bonding behavior allows to determine the electronic structure and consequently to come close to the understanding of the nature of studied surface reconstructions.

It is now generally accepted that the (100) surfaces of diamond, silicon, and germanium show dimer-based reconstructions [45, 46]. Symmetric dimers (SDs) dominate a 2×1 reconstruction of the C(100) surface [47]. At RT, Si and Ge exhibit a 2×1 reconstruction governed by asymmetric dimers (ASDs) [48]. A staggered arrangement of these dimers explains the $c(4 \times 2)$ low-temperature (LT) phase [46]. Recently, however, the atomic configuration of the Si(100) surface at very low temperature became a subject of debate. That concerns on the one hand the question whether the true surface ground state shows symmetric or asymmetric dimers. On the other hand, phase manipulation between $c(4 \times 2)$ and $p(2 \times 2)$ has been performed at 4.2 K using the STM [49]. The dimers were found to prefer the $p(2 \times 2)$ ordered phase when scanned with a negative tip. Applying a voltage pulse or scanning with a positive tip tends to reverse $p(2 \times 2)$ to $c(4 \times 2)$. Similar effects have also been observed on Ge(100) surfaces [50].

The origin and nature of reconstructions at (111) surfaces of elemental semiconductors is one of the most intensively discussed issues in surface physics. The (111) surfaces of diamond, silicon, and germanium show a manifold and puzzling reconstruction behavior in dependence on the surface preparation and the considered semiconductor. Silicon and germanium exhibit a 2×1 reconstruction following cleavage perpendicular to the [111] direction at RT. However, such a 2×1 reconstruction can be also found on the C(111) surface after careful preparation [46]. From many experimental and theoretical studies the (111) 2×1 surfaces are believed to have a π -bonded chain geometry [51]. In the case of Si and Ge the π -bonded chains are tilted [52, 58] whereas, apart from one exception [53], converged total-energy calculations do not indicate neither a chain buckling nor a chain dimerization for diamond(111) [41, 54, 55]. For Si and Ge the π -bonded chain reconstruction has two different isomers with the tilt angle of the uppermost chains in opposite directions [56–58]. The chain-left isomer has been indeed observed for Ge(111) 2×1 by means of scanning tunneling microscopy (STM) [59]. Heat treatment of cleaved Si(111) and Ge(111) surfaces at elevated temperatures cause the 2×1 reconstruction to convert into a 7×7 (Si, [60]) and a $c(2 \times 8)$ (Ge, [61]) structure, respectively. Whereas the Si(111) 7×7 surface is now explained by a dimer-atom-stacking-fault (DAS) model with corner holes [62–65], the Ge(111) $c(2 \times 8)$ surface is represented by a simple adatom model [66, 67]. Recently, it has been shown that a $c(2 \times 8)$ reconstruction can be also observed on the quenched Si(111) surface [68, 69].

There are various *ab-initio* studies of the basic reconstruction models, the π -bonded chain model for 2×1 [41, 53–56, 58], the DAS model for 7×7 [64, 65], and the adatom model for $c(2 \times 8)$ [67, 69]. However, there is no study by one and the same group and one and the same method of all reconstructions for even one semiconductor, not to speak about the three group-IV materials under consideration. Therefore, a comparison of the energetics and the driving forces of the reconstruction is hardly possible. Precise conclusions, why the lowest-energy reconstructions 2×1 , 7×7 , and $c(2 \times 8)$ of diamond, silicon or germanium are different, cannot be drawn. Obviously, despite the same valence-electron structure of the atoms and the same crystal struc-

ture of the corresponding solid, the different atomic sizes and bonding characteristics give rise to a stabilization of different surface reconstructions. An explanation based on first-principles calculations is, however, still missing. There are only model considerations comparing the energetics of 7×7 and $c(2\times 8)$ reconstructions [70].

Among the clean low-index silicon and germanium surfaces, the (110) surfaces are the only ones whose atomic structures are unknown. Only for diamond(110), Low-Energy Electron Diffraction (LEED) found a 1×1 diffraction pattern [71], the atomic structure of which can be characterized by relaxation. At least for silicon, the (110) surface has a free energy only slightly larger than that of the (111) plane [27]. It should therefore be a stable facet on the equilibrium crystal shape [44]. However, the preparation of such surfaces is difficult. Only non-vicinal, clean and well-annealed Si(110) surfaces exhibit a 16×2 reconstruction [72–75]. Contaminations, for example of very small amounts of Ni, destroy the long-range reconstruction and give rise to translational lattices with smaller unit cells, e.g. 5×1 [74, 76, 77]. STM experiments [73–75] suggest that the Si(110) 16×2 reconstruction consists of equally spaced and alternately raised and lowered stripes lying along the $[1\bar{1}2]$ direction. The height of the steps between two stripes is equal to the layer spacing in normal direction. Along the stripes these experiments reveal arrangements of “pairs of pentagons” which are more pronounced in empty-state images [75]. The experimental situation is less clear for the Ge(110) surfaces. In the pioneer’s work Olshanetsky et al. [78] showed that a $c(8\times 10)$ superstructure appears after annealing. Despite the existence of STM images for Ge(110) $c(8\times 10)$ [79], there are indications that the $c(8\times 10)$ structure is transient and unstable and changes into a 16×2 superstructure [80, 81]. However, for both periodicities the STM images show sequences of pentagons similar to the findings for the Si(110) surface.

There are no accepted structural models for the reconstructed Si and Ge(110) surfaces which consistently explain the energetics, the geometry and the electronic structure, in particular the STM images. Usually a certain distribution of adatoms and several top layers involved in the reconstruction are assumed in order to interpret the atomic structures of Si(110) 16×2 [72, 75, 82, 83] and Ge(110) $c(8\times 10)$ [79] or 16×2 [80, 81]. Conglomerates of adatoms which capture interstitial atoms like in the case of Si(113) surfaces [84] have been suggested by An et al. [75] to explain the pentagon pairs observed in high-resolution STM images of the Si(110) 16×2 surface. The origin of the stabilization of Ge(110) surfaces by certain reconstruction elements is also not understood. Recently, Ichikawa [81] explained the STM images observed for the Ge(110) 16×2 surface by pairs of five-membered adclusters. However, such structures are questionable from the energetical point of view.

Apart from one trial [81], theoretical studies have not been performed for the large 16×2 or $c(8\times 10)$ unit cells. Some attempts were devoted to find favorable reconstruction elements and to understand the bonding behavior by studying smaller unit cells [83, 85, 86]. In particular, it has been found that a bond-rotation relaxation mechanism should take place on Si and Ge(110) surfaces [85, 86] where the top-layer atomic chains are buckled like in the case of III-V compounds [44]. Dimerization similar to the (100) case has been proposed based on TB calculations [83]. Possible structures with adatoms have been studied by means of both *ab initio* [86] and TB molecular-dynamics calculations [85]. The suggestion of fully bonded

(i.e., fourfold-coordinated) adatoms which leave no dangling bonds [85, 86] is rather surprising for group-IV semiconductor surfaces and needs additional studies. In order to understand the atomic geometry and the bonding of the Si(110) 16×2 surface, one has to study the energetic preference and the structure of the step configuration observed by STM. Until now there is no idea why steps may occur on a flat, non-vicinal low-index surface, and how they contribute to the stabilization of the 16×2 translational symmetry. First-principles calculations exist only for the Ge(110) 16×2 surface [81]. They suggest a higher surface energy when steps are introduced, in contrast to the experimental observations of images in form of stripes on lower and higher terraces also for germanium [79].

High-index (113) surfaces of group-IV semiconductors are of interest from both the fundamental and applied point of view. In recent years wide flat (113) terraces have been prepared on Si substrates demonstrating that such surfaces are thermally stable against faceting [27]. Their inherent structural anisotropy makes (113) surfaces promising substrates for epitaxial growth of novel optoelectronic devices [87]. Very interesting is the fact that {113} facets have been observed on islands for all group-IV materials.

The actual atomic structure of the (113) surfaces is also strongly changed by the surface reconstruction. For Si and Ge, 3×1 and 3×2 translational symmetries have been reported [84, 88–108]. To our knowledge there is neither a theoretical nor a direct experimental study of clean reconstructed C(113) surfaces. The Si(113) surface exhibits a 3×2 reconstruction at RT, while a transition to the 3×1 phase is observed at elevated temperature [91, 94, 96, 104, 105]. In the Ge case 3×2 and 3×1 periodicities seem to coexist already at RT [95, 99, 108].

The bulk-terminated (113) surfaces of diamond-structure crystals consist of alternating rows of twofold-coordinated (001)-like atoms and threefold-coordinated (111)-like atoms. If one (001)-like atom is removed, the adjacent (111)-like atom looks like an adatom. The additional formation of a tetramer by bonding two (001)-like atoms leads to a 3×1 translational symmetry [88]. Many refinements of such an adatom-dimer (AD) model, including voids, puckering and buckling, and vertical displacement of the dimers, have been discussed to explain the observed 3×2 translational symmetry, particularly for Si [88, 89, 98, 101–104, 106]. One important step towards the understanding of the behavior of group-IV(113) surfaces was the introduction of a novel reconstruction element, a sixfold-coordinated surface self-interstitial similar to the [110]-split interstitial bulk defects, by Dabrowski et al. [84, 92, 107]. Interstitial distribution and migration [95, 107, 108] allow the study of additional surface reconstructions, among them adatom-interstitial (AI) and adatom-dimer-interstitial (ADI) models.

Meanwhile, there are several *ab initio* studies of 3×1 and 3×2 reconstructions of Si and Ge(113) surfaces [84, 106–110]. There are also studies using a semiempirical method [111] or combined methods [106]. However, the energetical ordering of the most important structural models is not well clarified for both Si and Ge [92, 106, 108]. Details of the geometrical reconstructions concerning their asymmetries, e.g. buckling, puckering, vertical displacement of appearing reconstruction elements, tetramers or pentamers, are under discussion. The chemical trends in energies and geometrical parameters are not understood. This holds for the comparison between Si and Ge(113) but, in particular, for C(113); the properties of this surface are unknown.

The driving forces of the various reconstructions have not yet been understood completely. The relationship between energetics, bonding, displacements of atoms, and the electronic structure is not clarified. There are only a few simulated images observable in STM [84, 92, 106, 107]. However, their relation to the surface band structures and surface electronic states is not derived. Calculated band structures are not published, except from those derived within a TB approach [106], the accuracy of which is, however, limited. The experimental bands for Si(113) 3×2 need an interpretation [102]. It has to be discussed why 3×1 reconstructions are seemingly observed in several experiments, despite the violation of the general reconstruction rules [112] and the electron counting rule [113]. Consequently, the metallic or insulating character of a (113) surface has to be explained in dependence on the translational symmetry but also the (local) point-group symmetry.

Then questions are addressed in the thesis at hand in the following way: Descriptions of the theoretical grounds and numerical approaches are given in Chapter 2. The studies of driving forces and the energetics of diamond, Si and Ge surfaces are presented in Chapter 3 for $\langle 100 \rangle$ and $\langle 111 \rangle$ surface orientations. Chapter 4 is devoted to the $\langle 113 \rangle$ surface orientation, whereas Chapter 5 focusses on the $\langle 110 \rangle$ surface orientation. A discussion of shapes of free and constrained crystallites based on the calculated absolute surface energies is given in Chapter 6. Summary and conclusions follow in Chapter 7.

Chapter 2

Theoretical background and numerical approaches

2.1 Many-body problem and steps for the solution

The theory of solids including their surfaces leads to a complicated microscopic description of interacting atoms. Formally the Hamiltonian \hat{H} of any system consists of kinetic and Coulomb interaction energy contributions of all nuclei and electrons involved. The properties of the system can be derived by solving the many-body Schrödinger equation:

$$\hat{H}\Psi = E\Psi, \quad (2.1)$$

where the wave function Ψ depends on the coordinates of electrons \mathbf{r} and nuclei \mathbf{R} . However, the solution of problem (2.1) is almost impossible because of its complexity. One needs to search for (some) approximations. One idea arises from the difference of the involved particles. The motion of nuclei is much slower than that of the electrons. Therefore, movements of the electrons and nuclei can be separated. The motion of the electrons is determined for the ensemble of nuclei at certain fixed positions. The resulting total energy of the electrons together with the ion-ion repulsion gives rise to a potential surface for the motion of the nuclei. Using the Born-Oppenheimer adiabatic approximation, the total wave function can be represented as a product of the ion and electron wave functions [114]. For the ground state of the electronic system one has to solve the Schrödinger equation for the many-electron Hamiltonian

$$\hat{H}_{\text{el}} = - \sum_i \frac{\hbar^2}{2m} \nabla_i^2 - \sum_{l,i} \frac{Z_l e^2}{|\mathbf{r}_i - \mathbf{R}_l|} + \frac{1}{2} \sum_{i \neq j} \frac{e^2}{|\mathbf{r}_i - \mathbf{r}_j|}, \quad (2.2)$$

where the three terms represent the kinetic energy of electrons \hat{T}_{el} , the interaction energy with the external potential \hat{V}_{ext} imposed on the electrons for a given nuclear configuration, and the Coulomb energy of interacting electrons \hat{U}_{ee} , respectively. Spin is not considered. The problem of the Hamiltonian (2.2) is still very difficult to solve. While \hat{T}_{el} and \hat{V}_{ext} depend only on the i -th electron, \hat{U}_{ee} involves pairs of electrons. According to Hartree a simplification can be achieved by writing the many-electron wave function as a product of one-electron wave functions $\psi_i(\mathbf{r}_i)$, $\Psi = \prod_i \psi_i(\mathbf{r}_i)$, which leads to an effective one-electron Schrödinger equation.

Such a simple product ansatz describes non-interacting particles. Since we have interacting particles it is only an approximation, implicitly assuming that adding an interaction to the non-interacting system does not significantly change the wave function. However, this is not the only weakness of this ansatz. The Hartree approximation needs to be improved upon by introducing Pauli's principle using an antisymmetric many-electron wave function in the form of a Slater determinant [115]. This is the idea of the Hartree-Fock (HF) approximation which introduces the spatially nonlocal electron exchange [116, 117]. The HF method requires already heavy numerical treatments, despite the fact that it does not take into account correlation effects. Correlation is, in fact, defined as the missing part of the HF electron-electron interaction compared to the exact solution. The HF method is usually only suitable for systems with not too many electrons. Because of neglecting correlation, it works better for atoms and molecules. In the case of solids such as metals and semiconductors, bonding and electronic properties are not reproduced correctly by the HF method. The inclusion of correlation effects using the so-called configurational interaction (CI) method is restricted to small molecules. Here, a sum of Slater determinants is needed which has to be truncated in practical calculations. Only such sums of Slater determinants allow an exact representation of any arbitrary wave function of a true interacting systems, whereas single Slater determinants are only exact in the case of systems of non-interacting particles.

2.2 Density-functional theory

A theory for the description of a system with many electrons including correlation effects is the Density-Functional Theory (DFT). It is based on the theorem of Hohenberg and Kohn that the ground-state energy is a functional of the electron density only [118]. A practical method for treating inhomogeneous systems of interacting electrons has been proposed by Kohn and Sham [119] and makes the DFT an extremely powerful tool for the determination of properties of matter using a microscopic model according to e.g. Eq. (2.2).

2.2.1 Hohenberg-Kohn theorem

This theorem is usually formulated for an external potential $V_{\text{ext}}(\mathbf{r})$ acting on a system of N electrons, which could be for instance the potential of an electron in the field of all nuclei which therefore depends on the configuration of the nuclei [cf. e.g. Eq. (2.2)]. The electron density $n(\mathbf{r})$ determines the ground state energy $E[n]$ of the system no matter what the external potential is. It has been proven by *reductio ad absurdum* that $V_{\text{ext}}(\mathbf{r})$ is a unique functional of $n(\mathbf{r})$. The knowledge of the total density $n(\mathbf{r})$ is as good as the knowledge of the wave function Ψ describing the ground state of the system. Since for a non-degenerate ground state Ψ is a functional of $n(\mathbf{r})$ [120], so are evidently also the resulting kinetic and interaction energies. For a given potential $V_{\text{ext}}(\mathbf{r})$, the energy functional can be written as

$$E[n] = \int V_{\text{ext}}(\mathbf{r})n(\mathbf{r})d\mathbf{r} + F[n], \quad (2.3)$$

where $F[n]$ is an universal functional which contains the total effect of the electron-electron interaction. For the density $n(\mathbf{r})$ that minimizes the functional (2.3), $E[n]$ equals the ground state energy E_0 . Thereby the admissible densities are restricted by the condition of particle number conservation

$$\int n(\mathbf{r})d\mathbf{r} = N. \quad (2.4)$$

The ground state density can be calculated, in principle exactly, using a variational method involving only the density. To determine $n(\mathbf{r})$ one finds

$$\delta \left\{ E[n] - \mu \left[\int n(\mathbf{r})d\mathbf{r} - N \right] \right\} = 0, \quad (2.5)$$

where μ is a Lagrange multiplier which may be interpreted as the chemical potential of the electrons. From Eq. (2.3) one obtains now

$$\frac{\delta E[n]}{\delta n(\mathbf{r})} = V_{\text{ext}}(\mathbf{r}) + \frac{\delta F[n]}{\delta n(\mathbf{r})}. \quad (2.6)$$

The major part of the complexities of the many-electron problem is now deferred to the determination of the universal functional $F[n]$.

2.2.2 Kohn-Sham method

In analogy to the Hartree or the HF approximation, it was proposed to separate the total energy in the components

$$E[n] = T_s[n] + \int \left[V_{\text{ext}}(\mathbf{r}) + \frac{1}{2} V_{\text{H}}(\mathbf{r}) \right] n(\mathbf{r})d\mathbf{r} + E_{\text{xc}}[n], \quad (2.7)$$

where $T_s[n]$ is the kinetic energy of a non-interacting electron system which has the same density $n(\mathbf{r})$ as the real interacting system. The classical Coulomb interaction between the electrons is described by the Hartree potential

$$V_{\text{H}}(\mathbf{r}) = e^2 \int \frac{n(\mathbf{r}')}{|\mathbf{r}' - \mathbf{r}|} d\mathbf{r}' \quad (2.8)$$

which includes self-interactions. The factor 1/2 avoids that pair interactions are counted twice. The external potential V_{ext} in Eq. (2.7) is due to the nuclei, and E_{xc} is the exchange-correlation energy. The last term includes all the interaction contributions missing in the previous terms, i.e., electron exchange and electron correlation, a portion of the kinetic energy which is needed to correct $T_s[n]$ to obtain the true kinetic energy of the real interacting system, and corrections to compensate the self-interactions introduced by the classical Hartree interaction. According to Eq. (2.6) one has

$$\frac{\delta E[n]}{\delta n(\mathbf{r})} = \frac{\delta T_s[n]}{\delta n(\mathbf{r})} + V_{\text{ext}}(\mathbf{r}) + V_{\text{H}}(\mathbf{r}) + \frac{\delta E_{\text{xc}}[n]}{\delta n(\mathbf{r})}. \quad (2.9)$$

The last three terms can be expressed by an effective potential V_{eff} , and a Schrödinger-like equation of noninteracting particles has to be solved. The so-called Kohn-Sham (KS) equation is

$$\left[-\frac{\hbar^2}{2m} \nabla_i^2 + V_{\text{eff}}(\mathbf{r}) \right] \psi_i(\mathbf{r}) = \epsilon_i \psi_i(\mathbf{r}). \quad (2.10)$$

It describes an auxiliary system of non-interacting particles, the density of which is equal to the density of the real interacting system. The ground-state density $n(\mathbf{r})$ is derived from the wave functions,

$$n(\mathbf{r}) = \sum_i^{\text{occ.}} |\psi_i(\mathbf{r})|^2. \quad (2.11)$$

The KS Eq. (2.10) has to be solved self-consistently. After subtraction of doubly counted terms the total ground-state energy can be expressed as

$$E[n] = \sum_i^{\text{occ.}} \epsilon_i - \frac{1}{2} \int \int \frac{n(\mathbf{r})n(\mathbf{r}')}{|\mathbf{r} - \mathbf{r}'|} d\mathbf{r}d\mathbf{r}' - \int V_{\text{xc}}(\mathbf{r})n(\mathbf{r})d\mathbf{r} + E_{\text{xc}}[n] \quad (2.12)$$

where $V_{\text{xc}}(\mathbf{r}) = \frac{\delta E_{\text{xc}}[n]}{\delta n(\mathbf{r})}$ is the exchange-correlation potential. Wave functions and densities depend parametrically on the atomic coordinates.

2.2.3 Local density approximation and limitations

The exchange-correlation energy $E_{\text{xc}}[n]$ in the KS equation (2.10) can be written in the form

$$E_{\text{xc}}[n] = \int e_{\text{xc}}[n, \mathbf{r}]n(\mathbf{r})d\mathbf{r} \quad (2.13)$$

where $e_{\text{xc}}[n, \mathbf{r}]$ is an exchange-correlation energy density per particle. In the local density approximation (LDA) $e_{\text{xc}}[n, \mathbf{r}]$ is replaced by the exchange-correlation energy of the homogeneous electron gas, $e_{\text{xc}}^{\text{hom}}(n)$, where the constant density is replaced by the local density of the studied inhomogeneous electron gas. It results in

$$E_{\text{xc}}[n] \simeq \int e_{\text{xc}}^{\text{hom}}(n) \Big|_{n=n(\mathbf{r})} n(\mathbf{r})d\mathbf{r}. \quad (2.14)$$

For $e_{\text{xc}}^{\text{hom}}$ there are several prescriptions available in the literature. The exchange part can be calculated analytically. For the correlation part, values have to be taken from numerical calculations. In the present work the Ceperly-Alder results [121] based on Monte-Carlo calculations and parameterized by Perdew and Zunger [122] are used.

Despite the fact that the LDA is a crude approximation for a strongly inhomogeneous gas, it is even able to predict bonding properties of solids with covalent bonds. There are quantitative errors in the evaluation of bond lengths, elastic constants, and cohesive energies which are in

principle known, and often the situation can be improved by using the generalized gradient approximation (GGA) [123]. Within the LDA one finds an overbinding tendency: The calculated cohesive energies come out larger compared to experiment, while lattice constants and bond lengths are smaller. In the case of Si, the lattice constant is 5.398 Å within LDA or 5.464 Å within GGA, while measurements give the value 5.431 Å [124]. It is also expected that absolute surface energies within GGA are somewhat lower than those calculated within LDA because of the larger cohesive energies obtained for the latter case.

Measurements such as photoelectron or inverse photoelectron spectroscopies are frequently directed to the determination of the electronic bands in a crystalline solid. Comparing with the KS eigenvalues in (2.10) in particular, the band dispersion is reasonably described. There is no clear justification for interpreting the one-particle eigenvalues in DFT as the band structure. This is because the KS energies are eigenvalues of the auxiliary system of non-interacting particles which have a physical meaning only for its density and functionals of the density, like the total energy. Only the highest occupied level has a real physical meaning and is identical with the first ionization energy of an N-electron system. However, despite its lack of formal justification as a description of band energies the KS scheme bears at least some merit for the description of excitations [125]. DFT transition energies between occupied and empty states, including the fundamental gap, are clearly underestimated. The underestimation of the fundamental band gap is a serious problem independent of the LDA or GGA treatment of the exchange-correlation energy [126]. Within the DFT-LDA (GGA) one obtains about one half of the experimental band gap for Si and C, and practically a zero gap in the case of Ge.

In order to obtain correctly the quantity corresponding to the experimental band gap one may calculate quasiparticle energies by using the many-body perturbation theory and determining the poles of the one-particle Green's function G . One way to proceed is Hedin's GW approximation [127, 128]. It accounts for the response of the electronic system to an electron or hole by screening. This leads to the occurrence of the screened Coulomb potential W . Usually, it is sufficient to calculate only the discrepancy between the exchange-correlation self-energy $\Sigma_{xc} = GW$ in this approximation with respect to the XC potential $V_{xc}(\mathbf{r}) = e_{xc}^{\text{hom}}(n) + n \frac{d}{dn} e_{xc}^{\text{hom}}(n) \Big|_{n=n(\mathbf{r})}$ already included in the KS Eq. (2.10). Within the first-order perturbation theory it results in quasiparticle shifts of all KS eigenvalues which open the gaps and increase transition energies between valence and conduction bands.

However, in general the DFT-LDA method is sufficient for the major purposes of this dissertation, in particular for studies of atomic structures of diamond, silicon and germanium surfaces in the ground state, and the second step, the evaluation of absolute surface energies since we focus on comparative studies. The KS eigenvalues are only used to discuss qualitatively the electronic structure of a surface,¹ in particular their metallic or insulating character and the appearance of bound surface states in the fundamental gap. Certain remarks will be given in the text where surface electronic structures of Ge surfaces are discussed.

¹The eigenvalues of the KS equation (2.10) are also used to simulate the STM images within the Tersoff-Hamann approach [129]. A constant-height mode is assumed for the simulation. Smearing-out procedures to account for the non-ideality of the tip are not used.

2.3 Total energy and forces

The KS approach allows the determination of the electronic ground-state energy of the system for a given nuclear configuration. The total energy of the system contains the electronic energy (2.7) and the energy of interacting ions:

$$E_{\text{tot}} = \frac{1}{2} \sum_{I,J} e^2 \frac{Z_I Z_J}{|\mathbf{R}_I - \mathbf{R}_J|} + E[n], \quad (2.15)$$

where the first term is the Coulomb repulsion energy of the nuclei. The force \mathbf{F}_I acting on the atom at the position \mathbf{R}_I can be obtained by the gradient

$$\mathbf{F}_I = -\nabla_{\mathbf{R}_I} E_{\text{tot}}. \quad (2.16)$$

E_{tot} depends explicitly on the coordinates of the nuclei. In addition, E_{tot} also depends implicitly on these coordinates via the charge density $n(\mathbf{r})$. Consequently two different contributions to the forces are obtained:

$$\mathbf{F}_I = -\frac{dE_{\text{tot}}}{d\mathbf{R}_I} - \int_{\Omega} \frac{\delta E_{\text{tot}}}{\delta n(\mathbf{r})} \frac{dn(\mathbf{r})}{d\mathbf{R}_I} d\mathbf{r}. \quad (2.17)$$

The force contribution due to the explicit dependence on the energy on the atomic position is called the Hellmann-Feynman force [130, 131]. It is of physical origin, in contrast to the second part in Eq. (2.17). This part is called variational force [132] and vanishes in the ground state for a given configuration $\{\mathbf{R}_I\}$. We optimize structures until forces are smaller than 10 meV/Å.

2.4 Plane-wave expansion

For the numerical treatment, it is advantageous to expand the KS eigenfunctions of Eq. (2.10) in certain orthonormalized and more or less complete basis sets. Since we apply the repeated-slab method [44] to model the surfaces, one has to handle an artificial system with huge unit cells. Because of a translational symmetry a system is expressed by the a Bravais lattice with lattice points $\{\mathbf{R}\}$. Consequently it can be expanded in terms of plane waves (PWs)

$$\frac{1}{\sqrt{\Omega}} \exp[i(\mathbf{k} + \mathbf{G})\mathbf{r}], \quad (2.18)$$

where \mathbf{G} is a reciprocal lattice vector with $\mathbf{G} \cdot \mathbf{R} = 2\pi$ times an integer number, and \mathbf{k} is a vector within the first Brillouin zone (BZ). The functions (2.18) form an orthonormal and complete set of wave functions. Performing calculations on periodic systems the KS orbitals in (2.10) with quantum numbers $i = j\mathbf{k}$ can be written as a sum of plane waves

$$\psi_{j\mathbf{k}}(\mathbf{r}) = \frac{1}{\sqrt{\Omega}} \sum_{\mathbf{G}} c_{j,\mathbf{k}+\mathbf{G}} \exp[i(\mathbf{k} + \mathbf{G})\mathbf{r}]. \quad (2.19)$$

The functions (2.19) fulfill the Bloch theorem. For numerical calculations, only a finite number of \mathbf{k} can be taken into account. Therefore, usually a set of so-called special \mathbf{k} points that are

adapted to the crystal symmetry is used [133–135]. An integral over \mathbf{k} points is approximated by a weighted sum:

$$\frac{(2\pi)^3}{\Omega_0} \int_{\text{BZ}} f(\mathbf{k}) d\mathbf{k} = \sum_{\text{sp}} w_{\text{sp}} f(\mathbf{k}_{\text{sp}}) \quad (2.20)$$

with Ω_0 as volume of a unit cell and the normalization $\sum_{\text{sp}} w_{\text{sp}} = 1$ for the weights. In the case of more than one \mathbf{k} point, a rather simple but flexible method has been suggested by Monkhorst and Pack (MP) [134] where the set of \mathbf{k} points is generated by division of the lattice vectors of the reciprocal lattice into P_i equal pieces. Every mesh point represents a \mathbf{k} point of the MP set. The points lying within the irreducible part of the BZ (IBZ) are finally used to calculate quantities such as the electron density or the total energy with weights according to their symmetry degeneracy. Hence, the number of \mathbf{k} points depends on the size of the IBZ and, therefore, on the symmetry (see also Sect. 2.9).

The expansion of the electronic wave functions would in principle require an infinite plane-wave basis set. However, the coefficients $c_{i,\mathbf{k}+\mathbf{G}}$ for the plane waves with small kinetic energy $\hbar/2m|\mathbf{k} + \mathbf{G}|^2$ are typically more important than for those with large kinetic energy. Thus the PW basis set can be truncated to include only plane waves that have kinetic energies less than some particular cutoff energy,

$$\frac{\hbar}{2m}|\mathbf{k} + \mathbf{G}|^2 \leq E_{\text{cut}}. \quad (2.21)$$

The energy E_{cut} has to be chosen in a way that, on the one hand, the wave functions may be reasonably represented and, on the other hand, the numerical effort is not too large. The convergence has to be carefully tested.

With a plane-wave basis, the KS equation gives the secular equation:

$$\sum_{\mathbf{G}'} \left[\frac{\hbar}{2m}|\mathbf{k} + \mathbf{G}|^2 \delta_{\mathbf{G},\mathbf{G}'} + V_{\text{eff}}(\mathbf{k} + \mathbf{G}, \mathbf{k} + \mathbf{G}') \right] c_{i,\mathbf{k}+\mathbf{G}'} = \epsilon_i c_{i,\mathbf{k}+\mathbf{G}}, \quad (2.22)$$

with the Fourier components $V_{\text{eff}}(\mathbf{k} + \mathbf{G}, \mathbf{k} + \mathbf{G}')$ of the KS potential. The latter potential is nonlocal due to the use of nonlocal pseudopotentials. In the local case the Fourier components only depend on differences of reciprocal lattice vectors, $V_{\text{eff}}(\mathbf{G} - \mathbf{G}') = V_{\text{ext}}(\mathbf{G} - \mathbf{G}') + V_{\text{H}}(\mathbf{G} - \mathbf{G}') + V_{\text{xc}}(\mathbf{G} - \mathbf{G}')$. In Eq. (2.22) the kinetic energy is diagonal, and the various potentials are described in terms of their Fourier transformations. The system (2.22) of algebraic equations has to be solved. The size of the Hamilton matrix which has to be diagonalized is determined by the choice of E_{cut} . It will lead to rather heavy calculations if the studied system contains both valence and core electrons. This problem can be overcome by the use of the pseudopotential approximation.

2.5 Pseudopotentials

The concept of pseudopotentials supplies smooth wave functions, which can be easily expanded in PWs. The core electrons do not contribute appreciably to the properties of interest and can

be “frozen” in their free-atom configuration, while the bonding is dominated by the behavior of the valence electrons. In particular, the Si atom consists of a nucleus ($14+$), core electrons [$1s^2 2s^2 2p^6$] and valence electrons [$3s^2 3p^2$]. The idea is to map the all-electron problem onto an equivalent problem involving valence electrons only. The consequences are (i) a frozen core with the nucleus and the core electrons and (ii) smooth orbitals for the valence electrons [136]. The formal transformation of the Hamiltonian is an orthogonalization to core states, giving pseudowavefunctions and pseudopotentials. It turns out that the orthogonalization “cancels” to a large extent the ionic attraction in the core region [137]. The pseudowavefunction of the lowest valence state is nodeless, and all the others are smooth as well. The ionic pseudopotential consists of a Coulomb attractive term, whose charge is the valence one, plus a short-range part, mostly due to non-classical orthogonalization repulsion, but which also has contributions from the true interactions with core electrons. In order to use the pseudopotential approach one has to ensure that the core overlap between neighboring ions is negligible.

A step forward to modern pseudopotentials has been done by the introduction of the norm-conservation requirement, in particular for applications in solid-state physics [138]. In this approach, pseudowavefunctions are constructed. The potentials are then found by inverting the atomic Schrödinger equation. Together with the matching conditions at R_{cut} the concept of norm-conservation guarantees that the pseudocharge distribution exactly reproduces the full valence charge beyond the core radius. Such pseudopotentials are nonlocal, because the radial ionic pseudopotential depends explicitly on the angular momentum. One more difficult problem has to be solved for Ge which has an extended core, $1s^2 2s^2 2p^6 3s^2 3p^6 3d^{10}$. In particular the $3d$ -core shell is extended, partial overlap with valence electrons is possible. To include this effect partially one has to use the so-called nonlinear core corrections which correct errors due to the linearization of the exchange-correlation energy in the valence and core electron densities [139, 140]. Si and Ge are best described using norm-conserving pseudopotentials.

There is still a problem for C atoms where the core only consists of the $1s$ electron shell. For materials with such a small core a good transferability can only be achieved by pseudopotentials which are very “hard” and consequently need a PW expansion restricted by a large cutoff in order to achieve convergence in a given calculation. E_{cut} is required to be of about 700 eV if norm-conserving pseudopotentials are used [141]. Atoms such as carbon can be better mastered within the ultrasoft pseudopotential scheme proposed by Vanderbilt [142], tailored to generate pseudowavefunctions which are smooth, although the condition of norm-conservation is not used. The missing charge is accurately accounted for by an augmentation procedure in the self-consistent scheme. As a result, the ultrasoft pseudopotentials achieve both high transferability (adequate description of the scattering properties of the ion in diverse chemical environments) and fast PW convergence. We apply the ultrasoft pseudopotentials not only for carbon but also for silicon and germanium. The details of the pseudopotentials used in this work are given in Table 2.1. A more detailed description of the construction of the pseudopotentials used can be found in Refs. [142–144] and the references cited therein. As a consequence of the optimization of the pseudopotentials the PW expansion of the single-particle eigenfunctions can be restricted by an E_{cut} of only 270 (C), 130 (Si), and 120 eV (Ge). In Fig. 2.1 a series of test calculations is shown for the total energy E_{tot} , lattice constant a_0 , and isothermal bulk modulus B_0 versus E_{cut} .

Table 2.1 Cutoff radii R_{cut} and types of pseudopotentials [ultrasoft (US), norm-conserving (NC), all electron (AE)] for corresponding angular momentum (AM) for C, Si, Ge and H used in the calculations. For hydrogen two types of pseudopotentials are used, H_{soft} for Si-H and Ge-H bonds and H_{hard} for C-H bonds. In the US case values in parentheses denote cutoff radii of the augmentation charges.

Element	AM	R_{cut}	Potential	Element	AM	R_{cut}	Potential
C	s	1.90(1.40)	US	Si	s	2.35(2.00)	US
	p	1.90(1.40)	US		p	2.80(2.20)	US
	d	1.90	NC		d	2.80(2.30)	US
	local	d_{pot}			local	1.60	cut AE
H_{soft}	s	2.00(1.50)	US	Ge	s	2.45(2.10)	US
	p	2.20(1.50)	US		p	2.90(2.30)	US
	local	1.0	cut AE		d	2.80(2.30)	US
H_{hard}	s	1.25(0.80)	US	local	1.60	cut AE	
	p	1.25(0.80)	US				
	local	0.65	cut AE				

The figure indicates convergence of the ground-state properties for the chosen energy cutoffs. The resulting lattice constants a_0 , chemical potentials μ , and fundamental energy gaps E_g (the latter ones are determined from bulk band structure calculations) are $a_0 = 3.531, 5.398,$ and 5.627 \AA , $\mu = -5.195, -5.957,$ and -10.147 eV , and $E_g = 4.15, 0.46,$ and 0.00 eV for C, Si and Ge in DFT-LDA.

2.6 Implementation and minimization algorithms

The investigation of the microscopic properties in the framework of DFT-LDA has been done with the VASP (Vienna *ab-initio* Simulation Package) code (see Refs. [145, 146]). This complex package allows the minimization of the total energy with respect to both electronic and ionic degrees of freedom. It also provides tools for generating and testing pseudopotentials if necessary. Most of the algorithms implemented in VASP use an iterative matrix-diagonalization scheme: the employed algorithms are based on the conjugate gradient scheme [147, 148], block Davidson scheme [149, 150], or a residual minimization scheme – direct inversion in the iterative subspace (RMM-DIIS) [151, 152]. For the mixing of the charge density an efficient Broyden/Pulay mixing scheme [152–154] is used. The package VASP is available as a fully parallel code. Together with the use of ultrasoft pseudopotentials and the effective minimization-schemes [145] it allows us to treat large systems, here artificial crystals with diamond, Si, and Ge surfaces, with up to several hundred atoms in a unit cell.

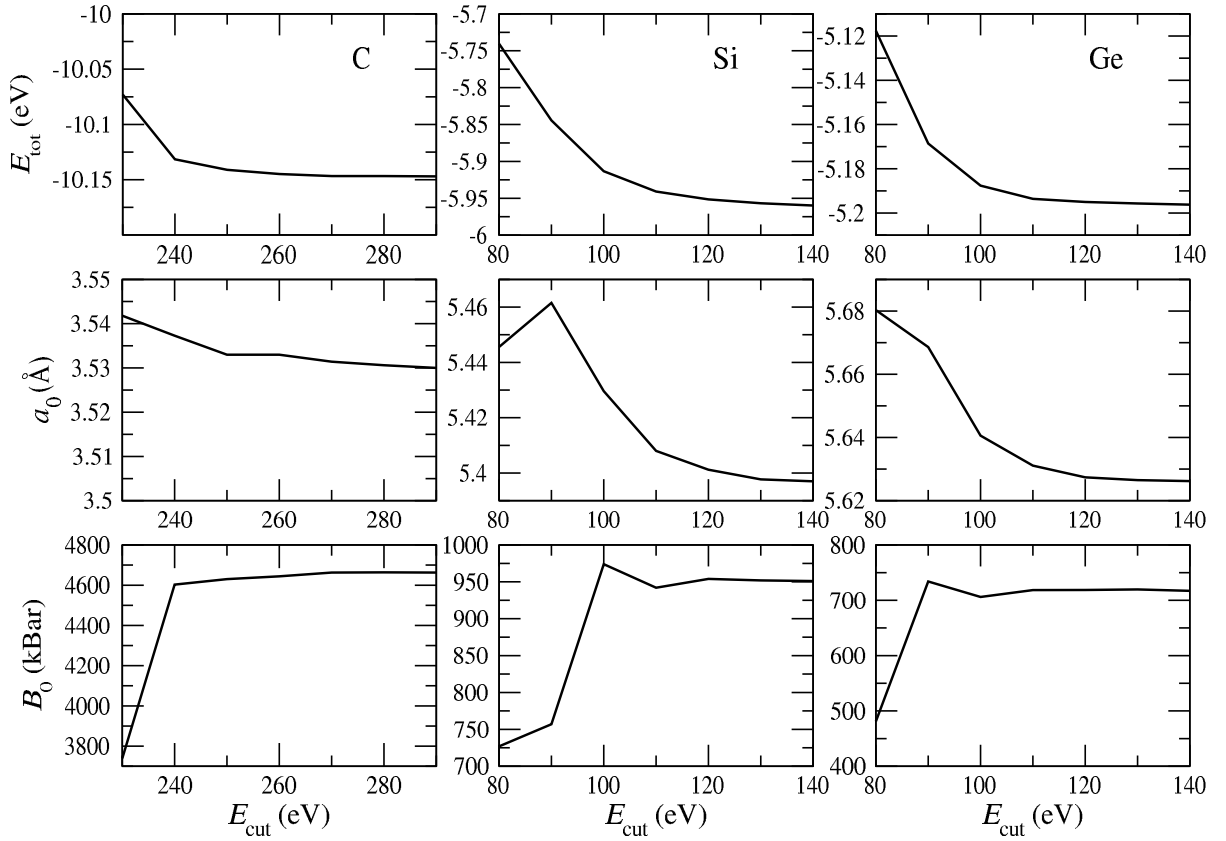


Figure 2.1 Convergence with respect to E_{cut} for bulk properties of C, Si, and Ge.

2.7 Thermodynamical relations for surfaces

2.7.1 Thermodynamical potentials and modification for surfaces

The equilibrium state of a one-component system consisting of N particles at a fixed temperature T and pressure p is the one with the minimum Gibbs free enthalpy $G(T, p, N)$ [155],

$$G = F + pV, \quad (2.23)$$

where $F(T, V, N)$,

$$F = U - ST, \quad (2.24)$$

is the Helmholtz free energy. It is related to the internal energy $U = U(S, V, N)$ and the entropy S by a Legendre transformation. The energy conservation law and the relationship between heat and work can be written in the form

$$dU = TdS - p dV + \mu dN \quad (2.25)$$

for an infinitesimal change of the internal energy. A variation of the number of particles N is allowed due to particle exchange with a reservoir characterized by the chemical potential μ

of the particle. For an isolated system with no heat exchange ($dS = 0$) and particle exchange ($dN = 0$) the internal energy is a constant at constant volume ($dV = 0$).

The thermodynamical potential G (or F) can be used to derive the thermodynamical quantities of the considered system at constant temperature T , particle number N and pressure p (or volume V). Infinitesimal changes of the three variables give rise to infinitesimal changes of the potential, so that

$$dG = -SdT + Vdp + \mu dN \quad (2.26)$$

or

$$dF = -SdT - p dV + \mu dN. \quad (2.27)$$

In equilibrium, F is a minimum with respect to the inner variables at constant T , V , and N , whereas G is a minimum at constant T , p , and N . The chemical potential μ in Eqs. (2.25), (2.26), or (2.27) is given by

$$\mu = \left(\frac{\partial U}{\partial N} \right)_{S,V} = \left(\frac{\partial F}{\partial N} \right)_{T,V} = \left(\frac{\partial G}{\partial N} \right)_{T,p}. \quad (2.28)$$

Under normal pressure of about 1 atmosphere, the difference between the Helmholtz free energy F and the Gibbs free energy G ,

$$\Omega = F - G = -pV, \quad (2.29)$$

is insignificant for a bulk solid or liquid. This holds in particular for volume-induced changes $-p dV$. Thus, it is sufficient to use F for the most cases interesting in solid state physics. The difference (2.7) is Kramer's grand potential $\Omega = \Omega(T, V, \mu)$ [156]. Despite its smallness, more precisely its vanishing influence on changes in the bulk systems including phase transitions, the potential is convenient to use for system transformations that occur at a constant temperature T , volume V , and chemical potential μ . This may be of particular interest for the surface region of the systems under consideration. Together with the Gibbs–Duhem equation, $SdT - Vdp + Nd\mu = 0$, infinitesimal changes of the variables result in

$$d\Omega = -SdT - p dV - Nd\mu. \quad (2.30)$$

The comparison of Eqs. (2.27) and (2.30) indicates a transformation law

$$\Omega = F - \mu N. \quad (2.31)$$

This is a consequence of the fact that the Gibbs free enthalpy varies linearly with the number of particles (cf. 2.29 and 2.31),

$$G = \mu N \quad (2.32)$$

with the proportionality factor $\mu = \mu(T, p)$ for each homogeneous phase [155].

In order to discuss the influence of a free surface of a halfspace, we follow Gibbs' idea of the "(equimolar) dividing surface" [156, 157]. It can be presented in terms of the particle density $n = N/V$ as a function of the distance normal to the surface. Values of n change gradually from its solid to its vapor value. The total space is divided into a bulk solid volume V_1 , a bulk vapor volume V_2 , and a volume V_s of the transition region, the surface. The corresponding densities n_1 and n_2 characterize the uniform bulk phases, the (semi-infinite) solid and its vapor with which the solid coexists and which occupies the other halfspace. The surface region, whose spatial extent is of atomistic dimensions (about 10 or less atomic layers), is thus a strongly inhomogeneous region surrounded by two homogeneous phases, the solid and the vapor. The number of particles in each phase 1 or 2 depends on the number of particles N_s in the surface transition region. The same holds for the volumes. This uncertainty is of the same order of magnitude as the surface effect itself. However, in the framework of a macroscopic theory, here the thermodynamics, the partition is made unique by applying the natural conditions [155]

$$\begin{aligned} V &= V_1 + V_2, \\ N &= n_1 V_1 + n_2 V_2. \end{aligned} \quad (2.33)$$

In comparison to the total number of particles the number of particles N_s in the surface region is assumed to be negligible. In the macroscopic limit it holds that $N_s = 0$.

The extensive thermodynamical potentials under consideration, the free energy F and the free enthalpy G , can be written as contributions from phases 1, 2 plus a surface term. We follow the derivation of Landau and Lifshitz [155] as well as of Desjonquères and Spanjaard [156] and consider Kramer's grand potential. Since in the thermodynamical equilibrium the pressure p is the same in the two homogeneous bulk phases, at least for a plane surface [155], equation (2.29) can be written in the form

$$\Omega = -p(V_1 + V_2) + \Omega_s. \quad (2.34)$$

The surface contribution Ω_s to the grand potential should be proportional to the surface area A ,

$$\Omega_s = \gamma A \quad (2.35)$$

with γ as the surface excess density of Ω .

2.7.2 Surface energy

The proportionality factor γ in Eq. (2.35) can be identified as the surface excess free energy per unit area or surface free energy for short (but imprecisely). For a one-component system the chemical potential μ is equal in both phases in the thermodynamical equilibrium. With the total number of particles according to Eq. (2.33), $G = \mu N$ Eq. (2.26) is still fulfilled. From the approximate description of the "dividing surface" with $N_s = 0$, one readily obtains $G_s = 0$ for the surface contribution. Thus, with Eq. (2.35)

$$F_s = \Omega_s = \gamma A \quad (2.36)$$

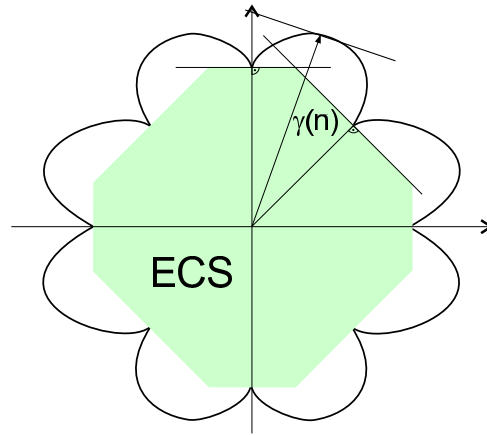


Figure 2.2 Example for the determination of the ECS from the Wulff construction.

holds. The surface excess free energy γ is sometimes called surface tension, although this term is somewhat confusing despite the corresponding common unit of measurement.

The calculation of the surface free energy for a given surface orientation $[hkl]$ and surface reconstruction is described in detail in Sect. 2.8. Here we assume zero temperature (or at least a thermal energy small compared to the energy barrier between two reconstructions) and that the crystal is unstrained. The calculations are restricted to the electronic configuration. The contribution of the zero-point displacements of the lattice is neglected. Only the core-core repulsion is taken into account and the system energies are calculated using expression (2.15).

2.7.3 Wulff construction

The anisotropy of the surface free energy per unit area, $\gamma(hkl)$, with the orientation of a certain surface $\{hkl\}$ determines the equilibrium shape of small free crystals at a particular temperature T (here: T small compared to the melting temperature). Wulff and later Herring [43, 158, 159] have derived a thermodynamic theory for the equilibrium shape of small crystals in the case that the energies $\gamma(hkl)$ for all facets, i.e. the relevant surface orientations $\langle hkl \rangle$, are known. It is based on the relation (2.36) for unstretched surfaces. The crystallite is assumed to be of at least mesoscopic or nanometer size so that edge and apex effects (more precisely, the corresponding energy terms) can be neglected (compared to the surface energy terms). Then, the equilibrium crystal shape (ECS) at constant (here: low) temperature T with fixed crystal(like) volume V and chemical potential μ of the group-IV material is determined by the minimum surface excess free energy F_s with respect to the total surface area $A = A(V)$ of the crystal,

$$F_s = \oint_{A(V)} \gamma(hkl) dA, \quad (2.37)$$

subject to the constraint of fixed volume V ,

$$V = \iiint_{V(A)} dV. \quad (2.38)$$

The direction \mathbf{n} of the area element dA is parallel to the facet normal $\langle hkl \rangle$. In the case of pure energetical studies of nanocrystals with pyramidal shape one has to take into account additional constraints such as the orientation and the shape of the basal plane of the pyramid. Formula (2.37) represents a bridge between microscopic and macroscopic approaches to the properties of matter. The surface free energies $\gamma(hkl)$ based on a full quantum-mechanical treatment of the motion of electrons (as discussed below) are combined to calculate a thermodynamic potential which is minimized with respect to the shape of a crystallite.

The Wulff theorem based on the minimum surface excess free energy (2.37) and the constraint (2.38) [43, 158, 159] states that the ECS is not necessarily that of the minimum surface area of the free crystallite. It may be a complex polyhedron with the lowest total surface energy for a given volume. A minimal surface area occurs only for perfectly isotropic (i.e., constant) values of $\gamma(hkl)$. The corresponding ECS is a sphere. The variation of γ with the normal $\mathbf{n} \parallel \langle hkl \rangle$ produces, on each surface element dA , a force proportional to $\partial\gamma/\partial\mathbf{n}$ which tends to alter the direction at the same time as γ tends to shrink the area. Consequently, in general the ECS cannot be a sphere. Determination of the ECS from the Wulff construction is equivalent to solving $r(\mathbf{h}) = \min_{\mathbf{n}}(\gamma(\mathbf{n})/\mathbf{n} \cdot \mathbf{h})$, where $r(\mathbf{h})$ is the radius of the crystal shape in the direction \mathbf{h} . A two-dimensional example of the Wulff construction is presented in Fig. 2.2. In a polar (spherical for 3D case) coordinate system, draw a vector parallel to the normal of the surface and with length proportional to the energy of the surface $\gamma(\mathbf{n})$. For each of the vectors draw the perpendicular line. The ECS is described by the interior envelope of these perpendicular lines (planes).²

2.8 Modeling of surfaces

In order to model the various surfaces we consider periodic arrangements of slabs along the surface normal. Each slab consists of a certain number of atomic layers and a vacuum region. Within one supercell the number of atoms in one layer is restricted to the surface unit cell. There are two types of possible slabs, centrosymmetric and asymmetric ones. In the first case two identical surfaces are involved as can be shown by applying a space-group transformation. In the second case one side of the material slab in the unit cell is saturated by hydrogen atoms as shown in Fig. 2.3. In our studies we use both types. While centrosymmetric slabs are used in order to obtain accurate absolute surface energies, the ones passivated by H and with substantially reduced number of layers are used to study surface reconstructions and accompanying band structures. Relative surface energies are also obtained by using asymmetric H-covered slabs as described below. They allow the calculations of relative surface energies for reconstructed surfaces with respect to a surface with a bulk orientation. The combination of such values with absolute surface energies of unreconstructed surfaces gives the absolute surface energy of a reconstructed surface.

²In the present work the program Wulffman for interactively examining the Wulff shapes of crystals is used [160].

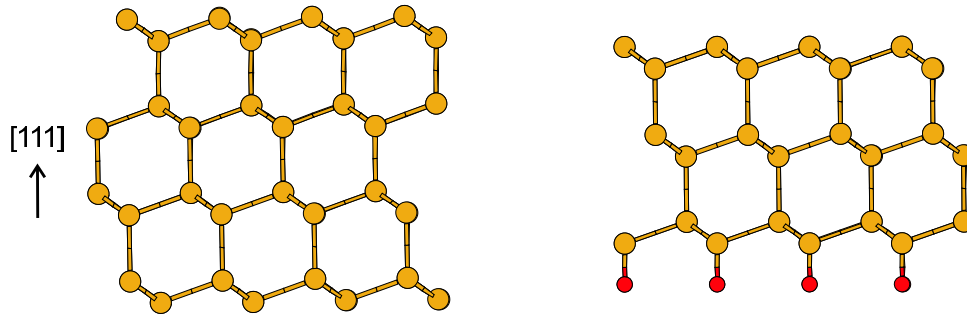


Figure 2.3 Examples for models of centrosymmetric (left) and asymmetric (right) slabs of (111) surfaces. Together with the vacuum region along the [111] direction the material slabs are repeated according to the translational symmetry. Two surfaces, an upper one and a lower one, occur for each system.

The two surfaces of a centrosymmetric slab are physically equivalent and, hence, allow the direct calculation of absolute (free) surface energies. As an advantage, in the centrosymmetric case the same surface and, hence, the same surface reconstruction $n \times m$ occurs on both sides of a material slab. For a given atomic configuration $\{\mathbf{R}_i\}$ in such a slab the surface energy (per 1×1 surface cell) can directly be inferred from the total energy of the slab $E_{\text{tot}}(N, \{\mathbf{R}_i\})$ with N atoms by subtracting N times the bulk energy μ per atom,

$$E_{\text{surf}}^{n \times m} = \frac{1}{2nm} \{E_{\text{tot}}(N, \{\mathbf{R}_i\}) - \mu N\}. \quad (2.39)$$

The introduction of the chemical potential μ of the constituents allows us to compare surfaces with different numbers of atoms in the two-dimensional surface unit cell. The values of μ are determined as a bulk energy per atom for a given slab when the vacuum region is filled. So the same numerical approaches are used to calculate slab and bulk energies. We obtain μ values which are identical with those mentioned in Sect. 2.5. In the case of the primitive $n \times m$ reconstructions $n \cdot m$ gives the number of 1×1 unit cells. In the case of a centered structure $c(n \times m)$ this number has to be divided by a factor 2. The prefactor $1/2$ in expression (2.39) indicates that for centrosymmetric slabs two equivalent surfaces are involved in the calculations. The surface energy per unit area

$$\gamma^{n \times m} = E_{\text{surf}}^{n \times m} / A \quad (2.40)$$

immediately follows dividing expression (2.39) by the area A of an 1×1 cell for a given surface orientation \mathbf{n} .

The quality of the surface calculations depends on the number of atomic layers and vacuum layers used in a supercell of the repeated-slab approximation. In order to obtain a fully relaxed geometry of a surface the relaxation of several top layers of the material slab is required. If the last condition is satisfied the number of additional layers will not really influence the final geometry. However, the absolute surface energies have to be completely converged. In Table 2.2 we list results of test calculations for a varying number of atomic layers in the material slab and

Table 2.2 Convergence of the surface energy γ (in J/m^2) with respect to the number of material layers and vacuum layers for $(111)1 \times 1$ centrosymmetric slabs with a total number of 18, 24, or 48 layers in the supercell.

Number of material layers	Diamond			Silicon			Germanium		
	18	24	48	18	24	48	18	24	48
6	7.406	7.406	7.406	1.697	1.697	1.698	1.228	1.225	1.221
8	7.866	7.866	7.866	1.798	1.798	1.798	1.312	1.308	1.303
10	8.059	8.059	8.059	1.835	1.834	1.833	1.348	1.342	1.336
12	8.101	8.100	8.100	1.830	1.828	1.826	1.349	1.343	1.335
14		8.115	8.115	1.828	1.827	1.824	1.352	1.344	1.333
16		8.120	8.120		1.827	1.824		1.344	1.330
18		8.120	8.120		1.827	1.823		1.402	1.328
24						1.822			1.328
32			8.120			1.822			1.331
36						1.823			1.334
40			8.120			1.825			1.339
44						1.826			1.345

the “total number of layers” including the vacuum region by atomic layers not occupied with atoms. The tests have been performed in order to obtain γ for ideal $(111)1 \times 1$ centrosymmetric slabs for diamond, Si, and Ge. Three different supercells with a total number of 18, 24, or 48 layers are studied. The convergence depends on the element. In the diamond case one needs at least 16 layers of material and a vacuum region corresponding to 6 layers in order to achieve convergence. Although the energies change when going from six layers to higher numbers within one slab, those for the same thickness do not correlate for the different supercells. In the case of the largest slab with 48 layers the value for γ does not change the surface energy with rising number of material layers with respect to the case with 16 layers. So, the absolute surface energy in the case of diamond is achieved. For Si small deviations of values at the third digit are observed. Because of the equal energies for 8 layers of Si for all the supercells, we conclude that a vacuum region corresponding to 10 layers is sufficient. After 14 layers γ shows only a small variation, which is practically negligible. The most critical case is Ge where, in contrast to diamond and silicon, a much larger number of atomic and vacuum layers has to be used. In particular for 14 layers of Ge within the three supercells under consideration, the variation is found to be 0.02 J/m^2 (cf. Table 2.2). Moreover, Ge seems not to show a performance like diamond or even Si with respect to the absolute surface energies. The situation is similar for other surface orientations. The reason for the required larger supercells is not only related to the weaker localization of the valence electron states in Ge. The much smaller ionization energies compared to C and Si and, therefore, the smaller surface barriers make interactions through the

vacuum more likely. Perhaps, the vanishing gap of Ge in DFT-LDA requires a refined \mathbf{k} -point sampling for the band structure energy.

For Ge we have taken into account 18, 15, 24, or 42 atomic layers and 30, 27, 36, 46 vacuum layers for the $\langle 111 \rangle$, $\langle 110 \rangle$, $\langle 100 \rangle$ or $\langle 113 \rangle$ surface orientation. For diamond and Si the number of vacuum layers can be remarkably reduced without changing the values of γ . Anyway, to represent absolute surface energies we allow for an inaccuracy less than 0.01 J/m^2 ($\approx 0.6 \text{ meV/\AA}$) for diamond and Si, while for the more complicated case of Ge the inaccuracy of the absolute surface energies may be increased to values of $0.01\text{--}0.02 \text{ J/m}^2$, in particular for a comparison of different surface orientations. This larger inaccuracy for Ge may be also influenced by the numerical inputs, the use of various unit cells, \mathbf{k} -sampling, and even FFT-meshes, for different orientations and reconstructions.

Equations (2.39) and (2.40) give the precise expressions for surface energies applicable to arbitrary surface translational symmetries and reconstruction models. However, despite the consideration of nonpolar group-IV semiconductors, the numerical effort due to the use of centrosymmetric slabs becomes too expensive for surface reconstructions yielding large unit cells. Too many atoms have to be taken into account for a converged calculation. This holds in particular for the long-range reconstructions such as Si(111) 7×7 or Si(110) 16×2 . For that reason, we only use the centrosymmetric slabs to obtain absolute surface energies for the unrelaxed surfaces with a 1×1 translational symmetry.

In order to reduce the computational efforts for the reconstructed surfaces, we focus the attention to reconstruction-induced energy changes. Therefore, we use asymmetric slabs with a reduced number of layers saturated by hydrogen atoms (Fig. 2.3). The H atoms are situated in directions of the one [(111), (110), (113)] or two [(100), (113)]³ bulk bonds cut forming a surface. For each surface orientation $\langle 110 \rangle$, $\langle 100 \rangle$ or $\langle 113 \rangle$ the group-IV-H bond length d_{IV-H} is optimized to find a minimum of the total energy. We obtain $d_{IV-H} = 1.11, 1.48, 1.52 \text{ \AA}$ for (111), $d_{IV-H} = 1.10, 1.49, 1.57 \text{ \AA}$ for (110), and $d_{IV-H} = 1.05, 1.44, 1.51 \text{ \AA}$ for (100) surfaces considering the three materials diamond, silicon, and germanium. Then, studying the reconstruction of the clean surface, the bottom layers of the hydrogen-covered slab sides are kept frozen during the surface optimizations. They simulate the bulk regions of the semiconductors under consideration. The numbers of the atomic layers (vacuum layers) are reduced to 8 (10), 15 (9), 8 (8), and 22 (22) for the reconstructions of the (111), (110), (100), and (113) surfaces for all materials considered. The uppermost five atomic layers are allowed to relax. For (113) surfaces this value increased to 6 double layers. To reduce the computational efforts and make the computations tractable, the number of atomic layers has been reduced to 7 for 3×2 , 6×2 and 16×2 reconstructions on Si and Ge(110) surface. Also in the case of the (111) 7×7 surfaces, determining the atomic geometries, we restrict ourselves to six atomic layers covered by an incomplete layer of adatoms on the upper slab side and a hydrogen layer on the bottom side.⁴

³In the case of (113) surfaces two kinds atoms, i.e. (111)-like and (100)-like atoms, appear after the bulk termination.

⁴Since the Si(111) 7×7 reconstruction is very well established, with the resulting atomic coordinates the total-energy calculations have been repeated using eight atomic layers to find converged surface energies.

According to the idea of expression (2.39), for asymmetric slabs with a given surface orientation one obtains the sum of two absolute surface energies

$$E_{\text{surf}}^{n \times m} + E_{\text{surf}}^{\text{H}} = \frac{1}{n \cdot m} \{E_{\text{tot}}(N, N_{\text{H}}, \{\mathbf{R}_i\}) - \mu N - \mu_{\text{H}} N_{\text{H}}\}, \quad (2.41)$$

one for the clean surface, $E_{\text{surf}}^{n \times m}$, and one for the hydrogen-covered surface, $E_{\text{surf}}^{\text{H}}$. Thereby, N_{H} denotes the number of hydrogen atoms, i.e., $N_{\text{H}} = n \cdot m$ in the case of the $\langle 111 \rangle$ orientation, $N_{\text{H}} = 2n \cdot m$ for (110) and (100), and $N_{\text{H}} = 3n \cdot m$ for non-centered (113) surface reconstructions. The chemical potential μ_{H} of the hydrogen atoms varies in dependence of the reservoir. Here, we assume that the reservoir is given by free hydrogen atoms, the total energy of which is taken from a calculation including spin polarization. The spin polarization lowers the total energy by 0.897 eV. As a consequence of the chosen H chemical potential the energy values of the hydrogen-covered surfaces, $E_{\text{surf}}^{\text{H}}$, will be negative. The assumption seems to be reasonable considering the hydrogen adsorption energy, $E_{\text{ads}}^{\text{H}} = E_{\text{surf}}^{n \times m} - E_{\text{surf}}^{\text{H}}$. It measures the energy gain due to the adsorption of free H atoms on the most stable, reconstructed group-IV surface. If $E_{\text{ads}}^{\text{H}}$ is larger than the molecular binding energy per atom of the H_2 molecule, 2.45 eV/atom, a dissociative adsorption of H_2 on the surface should be possible, unless there is a large energy barrier for the dissociation (Fig. 2.3 right). In this thesis we will however not discuss the hydrogen-covered surfaces.

Explicitly we do not use Eq. (2.41). It requires an extra calculation to find $E_{\text{surf}}^{\text{H}}$ using a centrosymmetric slab. Moreover, we avoid an additional inaccuracy due to the computation of μ_{H} for certain preparation conditions. The calculations of the absolute surface energies for relaxed and reconstructed surfaces does however not really need $E_{\text{surf}}^{\text{H}}$. Using expression (2.41) and computations for asymmetric slabs with the same H-covered slab sides, we only calculate the energy gain due to an $n \times m$ reconstruction by

$$\Delta E^{n \times m} = \frac{1}{n \cdot m} [E_{\text{tot}}(N_{\text{ideal}}, N_{\text{H}}, \{\mathbf{R}_i\}) - E_{\text{tot}}(N_{n \times m}, N_{\text{H}}, \{\mathbf{R}_i\}) - \mu \Delta N] \quad (2.42)$$

per 1×1 cell of a relaxed or reconstructed surface with respect to the corresponding unrelaxed surface. The number $\Delta N = N_{\text{ideal}} - N_{n \times m}$ indicates the variation of the number of group-IV atoms in the slab in dependence on the surface reconstruction. The non-centrosymmetric slabs with 8 or 15 atomic layers are sufficient to calculate the energy gain $\Delta E^{n \times m}$ with a high accuracy of about 1 meV, whereas the absolute surface energies using such slab thicknesses in the symmetric case possess an inaccuracy of about 20-30 meV. The absolute surface energies, which are given in the following, are combined by the accurately calculated absolute surface energies of unreconstructed surfaces and energy gains due to reconstruction. They follow from the relation

$$E_{\text{surf}}^{n \times m} = E_{\text{surf}}^{1 \times 1}(\text{unrelaxed}) - \Delta E^{n \times m}. \quad (2.43)$$

2.9 Two-dimensional Brillouin zones

The \mathbf{k} -point sampling in the irreducible part of the BZ varies with orientation and reconstruction of the surface. In the present studies all five two-dimensional Bravais lattices occur. For that

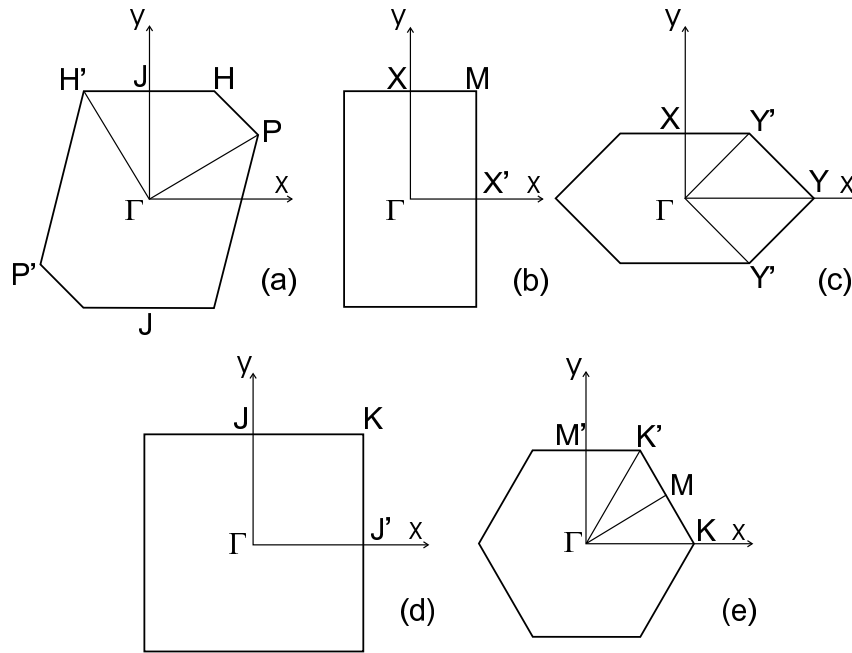


Figure 2.4 Brillouin zones of the five two-dimensional Bravais lattices: (a) oblique, e.g. $(113)2 \times 1$ and $(110)16 \times 2$, (b) rectangular, e.g. $(111)2 \times 1$, $(110)1 \times 1$, $(100)2 \times 1/4 \times 2$, $(110)2 \times 2/3 \times 2/6 \times 2$, and $(113)3 \times 2$ (c) c -rectangular, e.g. $(111)c(2 \times 8)$, (d) square, e.g. $(100)1 \times 1$, and (e) hexagonal, e.g. $(111)1 \times 1/7 \times 7$. High symmetry points and a 2D Cartesian coordinate system are indicated.

reason, also all BZs of these lattices have to be considered performing the \mathbf{k} -point integrations or summations in (2.20). They are shown in Fig. 2.4 indicating also certain high symmetry points.⁵ Several aspects have to be mentioned. Convergence to a certain accuracy, e.g. for the total energy of the slab system, requires a high density and a somewhat symmetry-adapted distribution of the \mathbf{k} -points. This becomes very important to compare absolute surface energies for different surface orientations and especially important to compare different reconstructions and, therefore, different translational symmetries. They give rise to different local minima on the total-energy surface. To find out the global one a high precision is required. We reach this by replacing the final energy minimization by a procedure using a common (in general non-primitive and, hence, larger) unit cell and therefore a smaller BZ. In the cases of $(110)2 \times 1$, 1×2 , and $c(2 \times 2)$ reconstructions 2×2 unit cells are used to minimize the total energy. On (110) and (113) surfaces for the variety of 3×1 and 3×2 reconstructions [in the case of (113) surfaces also for the 1×1 one], 3×2 unit cells are studied. A 4×2 cell is used for the treatment of $p(2 \times 2)$ or $c(4 \times 2)$ reconstructions on (100) surfaces.

⁵Unfortunately, the notation in the literature is not consistent. In the original papers several modifications are used. Which of the different points should be indicated by prime or not, is not exactly fixed. In the case of the rectangular BZ instead of X or M , the notations J and K are also possible.

Table 2.3 Number of \mathbf{k} points in the entire BZ and corresponding grids of Monkhorst-Pack points being used for different orientations and reconstructions.

Reconstruction	MP grid	\mathbf{k} points	Reconstruction	MP grid	\mathbf{k} points
(111)1×1	8×8×1	60	(110)1×1	12×8×1	96
(111)2×1	4×8×1	32	(110)2×2	6×4×1	24
(111) <i>c</i> (2×8)	4×4×1	12	(110)3×2	4×4×1	16
(111)7×7	2×2×1	2	(110)6×2	2×4×1	8
(100)1×1	8×8×1	64	(110)16×2	1×4×1	4
(100)2×1	4×8×1	32	(113)2×1	8×6×1	48
(100)4×2	2×4×1	8	(113)3×2	4×4×1	16

We need also \mathbf{k} -point sets to represent the surface band structures. Therefore, we repeat band calculations versus high-symmetry lines in the BZ. Here, the density of \mathbf{k} -points is chosen to reproduce the curvature of the bands correctly.

The number of \mathbf{k} -points used in the BZ is extremely important for converged results for slab energies. The grids of MP points and corresponding \mathbf{k} points for different surface reconstructions are presented in Table 2.3. Our tests (which have been partially presented in this chapter) showed that the used \mathbf{k} -point meshes and slab thicknesses give rise to quite accurate results. Useful test quantities are also the chemical potentials of the bulk materials resulting within a slab approximation. After filling the vacuum regions by atoms in bulk positions we calculate chemical potentials μ which only vary by maximum deviations from the "bulk" values calculated using the three-dimensional BZ of fcc lattice with an extremely high density of \mathbf{k} -points of 2.2, 0.7 or 0.2 meV for Ge, Si, and C with the slab orientation and the size of the two-dimensional unit cell. Moreover, the different \mathbf{k} -point sets are only used to calculate the reconstruction-induced energy gains $\Delta E^{n \times m}$. This also supports to reach the accuracy requirements discussed above.

Chapter 3

Low-index surfaces I – (100) and (111)

3.1 (100) surface orientation

The ideal, bulk-terminated {100} surfaces of diamond-structure crystals have a square unit cell, with one surface atom. The surface atoms possess two dangling sp^3 hybrids. However, such an ideal structure has not been observed experimentally. On a (100) surface a dehybridization takes place yielding a bridging $p_{y,z}$ orbital and a dangling sp_x orbital. The number of dangling bonds can be minimized by a pairing mechanism, more strictly by the formation of dimers representing a classical picture of reconstruction-induced surfaces. A variety of possible dimer-based reconstructions observed on (100) surfaces of group-IV semiconductor is shown in Fig. 3.1. Models represent symmetric and asymmetric dimers within 2×1 reconstruction and asymmetric dimers with different left/right-tilting arrangements within $p(2 \times 2)$ and $c(4 \times 2)$ reconstructions.

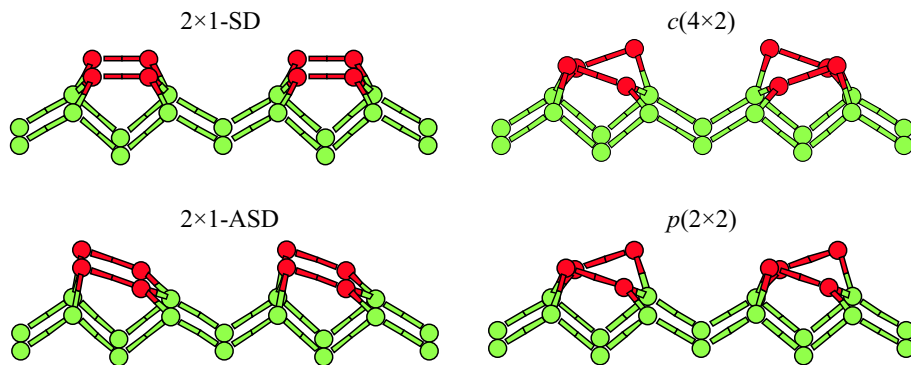


Figure 3.1 Perspective view of diamond(100) 2×1 -SD reconstruction and 2×1 -ASD, $c(4 \times 2)$, and $p(2 \times 2)$ reconstructions on Si or Ge(100) surfaces.

All above mentioned surface geometries are included in the present study. The results for the surface energies are listed in Table 3.1. We also list values for unreconstructed (i.e. bulk-terminated and relaxed) surfaces. One notices that relaxation of bulk-terminated (100) surfaces gives an energy gain of 0.3 eV per 1×1 unit cell for diamond but practically zero for Si and Ge. The surface energies are substantially lowered allowing a dimerization of two surface atoms

accompanied by a 2×1 reconstruction. We calculate large reconstruction energies of about 1.6, 0.9, and 0.6 eV for C, Si, or Ge due to the formation of dimers.

Table 3.1 Absolute surface energies $E_{\text{surf}}^{n \times m}$ and $\gamma^{n \times m}$ for various (100) surface reconstructions.

Reconstruction	E_{surf} (eV/ 1×1 cell)			γ (J/m ²)		
	C	Si	Ge	C	Si	Ge
bulk-terminated	3.78	2.17	1.69	9.72	2.39	1.71
relaxed	3.65	2.17	1.69	9.40	2.39	1.71
2×1	2.22	1.32	1.03	5.71	1.45	1.05
$p(2 \times 2)$		1.286	0.993		1.41	1.00
$c(4 \times 2)$		1.285	0.985		1.41	1.00

In Table 3.2 values of the characteristic geometry parameters (see also Fig. 3.2) for different dimer-based reconstructions are listed. In general, the basic 2×1 reconstruction of the (100) surfaces indicates an opposite behavior of silicon and germanium on the one side and diamond on the other side. Dimers with strong bonds are formed. Their bond lengths d_{dim} are close to the bulk ones for Si and Ge (cf. Table 3.2) but d_{dim} approaches the value of a double bond $>C=C<$ in the case of diamond. In the C(100) 2×1 reconstruction dimers are symmetric. Si and Ge(2×1) show asymmetric behavior. This asymmetry is well characterized by the different lengths d_{back} and d'_{back} of the backbonds of the two dimer atoms. The tilt angles φ of the Si and Ge dimers with about 18 and 19° are in agreement with values of other *ab initio* calculations [48].

Table 3.2 Geometry parameters of dimer-based reconstruction on (100) surfaces. Lengths are given in units of the bulk bond length. The dimer buckling is characterized by the angle φ (in degrees).

Geometry parameter	2×1			$p(2 \times 2)$		$c(4 \times 2)$	
	C	Si	Ge	Si	Ge	Si	Ge
d_{dim}	0.90	0.98	1.00	1.00	1.03	1.00	1.03
d_{back}	0.98	1.02	1.03	1.01	1.03	1.01	1.03
d'_{back}	0.98	0.99	1.00	0.99	1.00	0.99	1.00
φ	0	18.4	19.2	19.2	19.7	19.2	19.8

The origin of the different reconstruction behavior of diamond as opposed to Si and Ge is related to the different strengths in σ - and π -bonding between the orbitals at the atoms of the symmetric dimers and the lack of p states in the diamond core. For C $2p$ orbitals are more localized than $2s$ orbitals, while in the case of Si and Ge $3p$ orbitals are more extended than $3s$ ones. For the bonded surface atoms the σ and σ^* bonding and antibonding states cannot modify

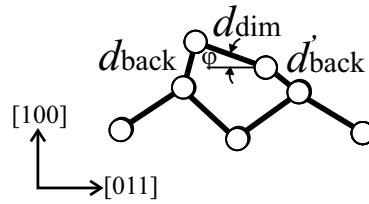


Figure 3.2 Side view of asymmetric 2×1 model with notations of characteristic geometry parameters. The corresponding values are given in Table 3.2.

the electronic structure around the projected fundamental gap. Only surface bands belonging to the π - and π^* -like bonding/antibonding states may occur in the fundamental gap.

The surface electronic structures resulting within the SD or ASD model of the $(100)2 \times 1$ surfaces are plotted in Fig. 3.3. Each structure shows the projected bulk bands as shaded region in the surroundings of the fundamental gap. Solid lines represent the surface bands. The valence-band maximum (VBM) of the bulk band structure is taken as energy zero. As a consequence of the short dimer bond, the π -interaction between the dangling bonds at the C $(100)2 \times 1$ surface is strong enough to clearly separate the bonding π -band and an antibonding π^* -band energetically appearing in the fundamental gap.¹

The situation is different for Si and Ge $(100)2 \times 1$ reconstructions, where the π -interaction are not strong enough to open up a surface gap (see e.g. [48]). A Jahn-Teller-like distortion is expected to open a surface gap between the π and π^* bands. For Si and Ge an insulating surface only occurs after dimer buckling. The corresponding energy gain via the band structure energy explains why the symmetry-breaking tilting of the dimers is energetically favorable. Buckled dimers consist of two atoms, an sp^2 -like bonded lower atom with a p_z -like dangling bond and upper one with an s -like dangling bond. The charge transfer occurs from the lower atom to the upper one which becomes fully occupied. Consequently a surface band gap is opened.

Arrangements of the buckled dimers in $c(4 \times 2)$ and $p(2 \times 2)$ reconstructions lower the Si and Ge surface energies further (cf. Table 3.1). Corresponding values of the bond lengths and angles of the buckling are practically equal between $c(4 \times 2)$ and $p(2 \times 2)$ phases for each material independently of left/right-tilting of the dimer. Only the characteristic angle is little bit larger than the one for the 2×1 ASD reconstruction (cf. Table 3.2). Indeed, $c(4 \times 2)$ gives the most stable ground state phase for Si and Ge (100) surfaces. However, there is only a tiny energy difference between these two reconstructions (i.e. one or eight meV per 1×1 cell for Si and Ge, respectively). This is in agreement with previous first-principles calculations [161–163]. Taking into account effects of STM tip such a small preference of the $c(4 \times 2)$ reconstruction makes quite plausible the observation of the $p(2 \times 2)$ translational symmetry, in particular on Si (100)

¹It has to be mentioned that the band structure of C $(100)2 \times 1$ in Fig. 3.3 has been calculated using symmetric slabs. The idea of saturation of the dangling bonds at one slab side by hydrogen atoms cannot be used to obtain a reliable band structure for C $(100)2 \times 1$. In the case with two dangling bonds per surface atom the interaction of neighboring C-H antibonds is so strong that the upper part of fundamental gap is filled with hydrogen-related surface states. On the other hand, the idea that the group-IV-hydrogen bonding and antibonding orbital combinations give rise to energies far away from the fundamental band gap is still valid for silicon and germanium.

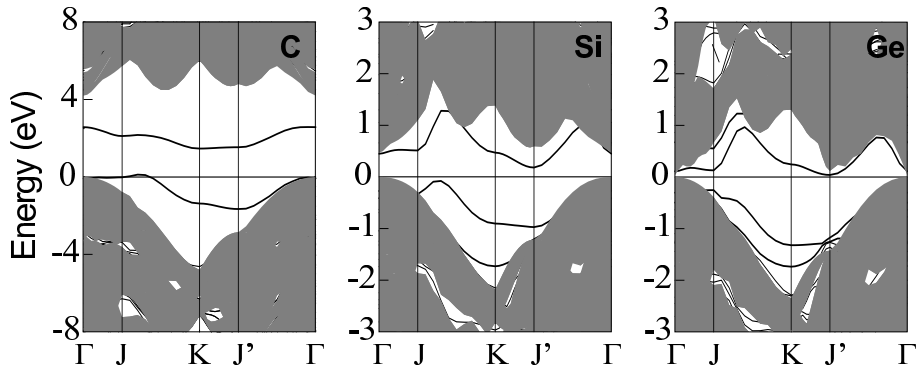


Figure 3.3 Band structures of (100) 2×1 surfaces with symmetric dimer (diamond) and asymmetric dimer (Si and Ge).

surfaces. Recent *ab-initio* calculation showed a possible mechanism which shifts the energy balance when external electric fields point along the surface normal and electrons are inserted into surface states [164].

The absolute surface energies are very interesting. They show a clear chemical trend along the row C, Si, and Ge, similar to the bulk cohesive energies. In general, the largest surface energies appear for the diamond surface whereas the smallest ones are calculated for germanium. Comparing the energies with other findings one gets for Si surfaces with unspecified or 2×1 reconstruction the values $\gamma = 1.36$ [27], 1.34 [38], 1.49 [39], and 1.16 J/m² [165]. Other calculations [40] give $\gamma = 2.32$ and 1.21 J/m² for the unrelaxed or relaxed surface. Large values are reported for diamond(100). Classical potentials give the values $\gamma = 9.21$ and 3.34 J/m for the unrelaxed or relaxed surface [40]. The huge reduction of the surface energy per unit area due to surface relaxation agrees with the *ab initio* findings listed in Table 3.1.

3.2 (111) surface orientation

3.2.1 Energetics

In Figure 3.4 we present (111) surface reconstructions of group-IV elements for different models. The results for the absolute surface energies for (111) surface reconstructions are listed in Table 3.3. All considered rearrangements of surface atoms – the relaxed 1×1 surface [46], the π -bonded chain model of the 2×1 surface with the two isomers [56, 58], the $c(2\times 8)$ adatom reconstruction [66, 67], and the 7×7 DAS model [62–65] – give rise to local minima on the total-energy surface. The (111) surface gains energy during relaxation or reconstruction. The gain values obtained from other *ab initio* calculations [41, 54, 55, 58, 166, 167] for the relaxed 1×1 and the π -bonded chain 2×1 surfaces are rather similar. This holds for example for the remarkable large energy gain due to relaxation of the C(111) surface, which has been traced back to a tendency for the formation of a graphite overlayer [55]. There is also agreement concerning the preference of the chain-left isomer for Ge [57, 58]. The situation is less clear in the

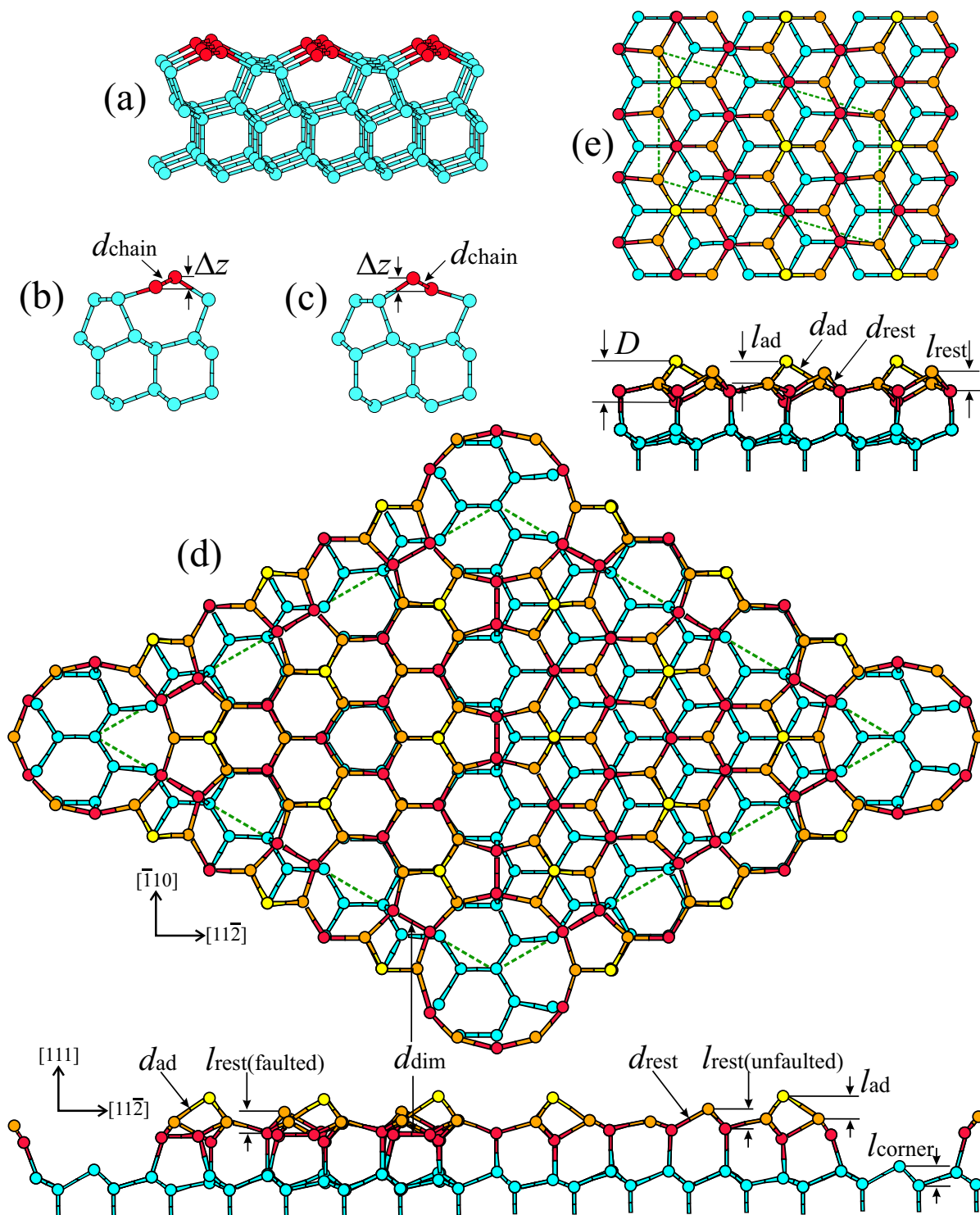


Figure 3.4 Various (111) surface reconstructions. (a) Perspective view of π -bonded chain model of $(111)2 \times 1$; (b) side view of π -bonded chain model of $(111)2 \times 1$, chain-right isomer; (c) side view of π -bonded chain model of $(111)2 \times 1$, chain-left isomer; (d) $(111)7 \times 7$, DAS model (top and side views); (e) $(111)c(2 \times 8)$, adatom model (top and side views).

Si case, since the energy differences between chain-right and chain-left isomers are smaller in agreement with Refs. [56, 57].

Table 3.3 Absolute surface energies $E_{\text{surf}}^{n \times m}$ and $\gamma^{n \times m}$ for various (111) surface reconstructions.

Reconstruction	E_{surf} (eV/1×1 cell)			γ (J/m ²)		
	C	Si	Ge	C	Si	Ge
bulk-terminated	2.73	1.43	1.13	8.12	1.82	1.32
relaxed	2.16	1.37	1.12	6.43	1.74	1.30
2×1(right)	1.37	1.14	0.90	4.06	1.45	1.05
2×1(left)	1.37	1.13	0.89	4.06	1.44	1.04
c(2×8)	2.35	1.11	0.86	6.96	1.41	1.01
7×7	2.39	1.07	0.87	7.11	1.36	1.02

Table 3.3 clearly indicates the different reconstruction behavior of the three group-IV semiconductors under consideration. According to our calculations we find a further lowering of the absolute surface energy going from the 2×1 reconstruction (π -bonded chain model) to the c(2×8) reconstruction (adatom model) and 7×7 (DAS model) in the case of both Ge and Si. In the case of diamond the large reconstructions are completely unfavorable. This is in agreement with studies [168] which found that adatoms and vacancies on the diamond(111) surface are energetically less favorable than the relaxed surface in contrast to the case of Si and Ge. For instance, the truncated diamond crystal gains more energy by the relaxation in the first atomic layers than by the addition of adatoms leading to a c(2×8) translational symmetry. The increase of the energy gain in the Ge(111)c(2×8) and Si(111)7×7 cases with respect to the 2×1 surface is in agreement with previous calculations [58, 67]. Here, we also clearly show that in the Si case the 7×7 reconstruction (DAS model) gives the most favorable reconstruction. In the Ge case, we observe more or less the same energy for c(2×8) and 7×7. This may be a consequence of numerical inaccuracies, in particular related to the small number of atomic layers used in the calculations. However, the values in Table 3.3 really calculated with 8 atomic layers and 16 vacuum layers in the supercell give rise to the preference of c(2×8) versus 7×7 in the Ge case. On the other hand the 7×7 surface can be also prepared for germanium in the presence of biaxial strain [169]. Interestingly, there is the preference of c(2×8) against 2×1 in the Si case. Indeed, a c(2×8) ordering is observed on the quenched Si(111) surface [68]. We mention that the energy gain of 0.26 eV due to the adatom adsorption between c(2×8) and 1×1 (relaxed) is close to the adatom binding energy measured by means of STM on Ge(111) [170].

The absolute surface energies E_{surf} for the 1×1 and 2×1-reconstructed diamond surfaces in Table 3.3 are in complete agreement with results of previous first-principles calculations [41, 42, 171]. On the other hand, computations using classical interaction potentials underestimate the surface energies with $\gamma = 3.39$ (unrelaxed) and 0.83 (relaxed) J/m² [40] in the case of diamond with strong bonds. In the Si case this underestimation is less drastical. The method using interaction potentials [40] gives 1.15 and 1.02 J/m². A molecular dynamics simulation

Table 3.4 Characteristic geometry parameters of relaxed and reconstructed (111) surfaces. All lengths are indicated in Fig. 3.4 given in units of the bulk bond length.

Reconstruction	Geometry parameter	Diamond	Silicon	Germanium
(111)1×1 (relaxed)	$3l$	0.50	0.79	0.90
(111)2×1 (right)	Δz	0.00	0.23	0.33
	d_{chain}	0.93	0.97	0.99
(111)2×1 (left)	Δz	0.00	0.27	0.34
	d_{chain}	0.93	0.97	0.99
(111)c(2×8) (adatom)	$3l_{\text{ad}}$	0.58	0.55	0.58
	d_{ad}	0.88	0.86	0.88
	D	1.04	1.03	1.07
	$3l_{\text{rest}}$	0.75	1.41	1.51
	d_{rest}	0.72	0.81	0.83
(111)7×7 (DAS)	$3l_{\text{ad}}$	1.75	1.67	1.75
	d_{ad}	1.06	1.05	1.07
	$3l_{\text{rest}}$ (faulted)	0.72	1.41	1.50
	$3l_{\text{rest}}$ (unfaul.)	0.72	1.35	1.50
	d_{rest}	0.98	1.02	1.03
	$3l_{\text{corner}}$	0.88	1.44	1.56
	d_{dim}	1.08	1.04	1.04

with empirical potentials [39] ends with a value $\gamma = 1.41 \text{ J/m}^2$ for the relaxed Si(111)1×1 surface, whereas tight-binding calculations [38] lead also to $\gamma = 1.41 \text{ J/m}^2$ but for the 2×1 reconstructed surface. Experimentally surface energies for Si(111) have been extracted from the equilibrium shape of voids as $\gamma = 1.23 \text{ J/m}^2$ [27]. Using a cleavage technique Gilman [172] measured a surface energy of Si(111) as 1.24 J/m^2 at a low temperature of -196°C . These experimental values are close to the theoretical ones calculated for reconstructed surfaces. We have to mention that with 1.51 and 1.18 eV Stich et al. [65] and Brommer et al. [64] calculated values for E_{surf} which envelope the surface energy of Si(111)7×7 given in Table 3.3. However, the energy lowering 0.06 eV of Stich et al. [65] for 7×7 with respect to 2×1 exactly approaches the value obtained here. To our knowledge neither experimental nor theoretical values have been published in the case of germanium.

3.2.2 Geometry

In Table 3.4 the values of characteristic geometry parameters for the various reconstructions of the (111) faces are listed. The geometry parameters are introduced in Fig. 3.4. The parameter l characterizes the distance between the nominal first- and second-atomic layers on the relaxed (111) surface. In the case of the $c(2 \times 8)$ adatom reconstruction and the 7×7 DAS model l gives

the vertical distances between rest atoms (l_{rest}), adatoms (l_{ad}), center-corner-hole atoms (l_{corner}) and the atoms in the layer below. For the rest atoms and the adatoms we list an average value in Table 3.4 independent of the atomic position and the faulted or unfaulted area in the 7×7 cell. We only distinguish between the rest atoms on the faulted and the unfaulted regions. In Table 3.4 we list the triple values of l etc., since on the ideal surfaces with atoms in bulk-like positions and bulk bond lengths these vertical distances are given by $d_{\text{bulk}}/3$. With exception of l_{ad} for $c(2 \times 8)$ the values of the vertical distances on the (111) surfaces indicate a completely different behavior of diamond on the one hand and silicon or germanium on the other hand. For diamond these distances are usually smaller than $d_{\text{bulk}}/3$ indicating a strong tendency for graphitization in the first atomic layers. This vertical approach of the atoms in neighboring atomic layers is in particular well pronounced for the relaxed surface. In this case also Si and Ge(111) 1×1 surfaces exhibit a small approach of first- and second atomic layers. However, for the $c(2 \times 8)$ and 7×7 reconstructions the adatoms, rest atoms and corner-hole Si or Ge atoms show the opposite effect. For Si and Ge(111) $c(2 \times 8)$ one observes an increase of l_{rest} with respect to the ideal value, whereas the adatoms are displaced towards the bulk. This geometry is accompanied by a rehybridization of the rest atoms resulting in s -like dangling bonds. Consequently, the adatoms should donate their electrons to the s -like dangling bonds of the rest atoms resulting in an energy gain. The adatoms on the $c(2 \times 8)$ surface and 7×7 surface in T_4 position are characterized by a bond length d_{ad} to the atoms in the nominal first-atomic layer. Interestingly, this parameter does practically not vary with the group-IV semiconductor, neither in the $c(2 \times 8)$ case nor in the 7×7 case. The adatom heights l_{ad} above the first-atomic layer depend on the area in the 7×7 case. We confirm the experimental and theoretical result for Si [173–176] that l_{ad} is larger for the faulted region than for the unfaulted region. However, this effect (not shown in Table II) is more pronounced for Ge than for Si. The opposite behavior happens for the rest atoms. In the 7×7 DAS case, in addition we consider the dimer bond length d_{dim} , which, however, also does not vary with the element. Another interesting parameter is the vertical distance D of the adatoms to the second atomic layer. It almost approaches the value of the bulk bond length indicating the basic idea of the T_4 adatoms that the wave functions of adatom and second-layer atom overlap.

The chain-right and chain-left isomers of the 2×1 π -bonded chain reconstruction are characterized by a bond length d_{chain} and the buckling Δz of the chains. A possible dimerization of the chains on (111) is not indicated. The bonds along the π -bonded chains are slightly contracted with respect to the ideal bulk bond length as found by many authors. There is a clear chemical trend. The contraction is the largest one for diamond. We confirm the remarkable buckling of the chains on the Si and Ge(111) 2×1 surfaces [56–58] and its vanishing value for C(111) 2×1 [41, 55, 166]. Bond contraction and buckling are rather independent of the chain-right or chain-left isomer. Only the buckling increases from the chain-right to the chain-left isomer of Si(111) 2×1 .

There is a clear difference between Si, Ge, and diamond. Again as for the dimer-based reconstructions on (100) surfaces diamond shows no asymmetry within the (111) 2×1 π -bonded chain model what is due to the strong C-C bonding and, hence, the lack of p electrons in the core. It is also responsible for the absence of long-range adatom-induced reconstructions on

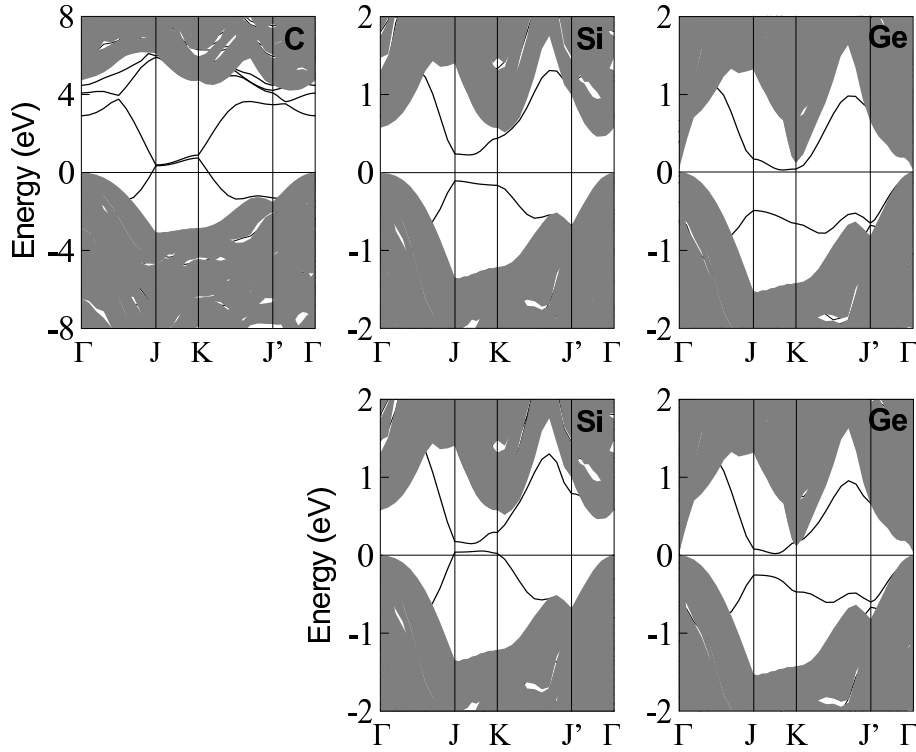


Figure 3.5 Band structures of the (111) 2×1 surfaces described within the π -bonded chain model. The upper panels show the bands of the chain-right isomers whereas the lower panels give the results for the chain-left isomers.

diamond(111). The bigger Si valence electron shell is much more softer and, consequently, a certain buckling of the chains for (111) 2×1 is more likely. Values of the tilting angles increase for Ge as the softest material. The behavior of Ge surfaces is also attributed to the presence of d electrons in the core. Subsurface stresses must be smaller for Si and Ge than for diamond when adatoms are present on the surfaces what allows long-range reconstructions (e.g. $c(2\times 8)$) with an energy gain due to the electron transfer between adatoms and the rest atoms. In the intermediate case of silicon, additional reconstruction elements occur to balance the different tendencies observed for diamond and germanium.

3.2.3 Band structures

The different geometries influence the band structures. Their occupied parts may however already give an explanation of the energetics discussed above via the band structure energies. This is demonstrated for the 2×1 , $c(2\times 8)$, and 7×7 reconstructions. The band structures of the π -bonded chain reconstructions in Fig. 3.5 along the $\Gamma J - JK - KJ' - J'\Gamma$ directions are characterized by an upper π^* -like and a lower π -like band in the fundamental bulk energy gap. In the diamond case the surface is metallic within the used DFT-LDA. The two bands are degenerate at J in the surface BZ. Moreover, both bands widely overlap in energy along the JK direction. The chain buckling in the case of the Si and Ge atoms with larger cores lifts the

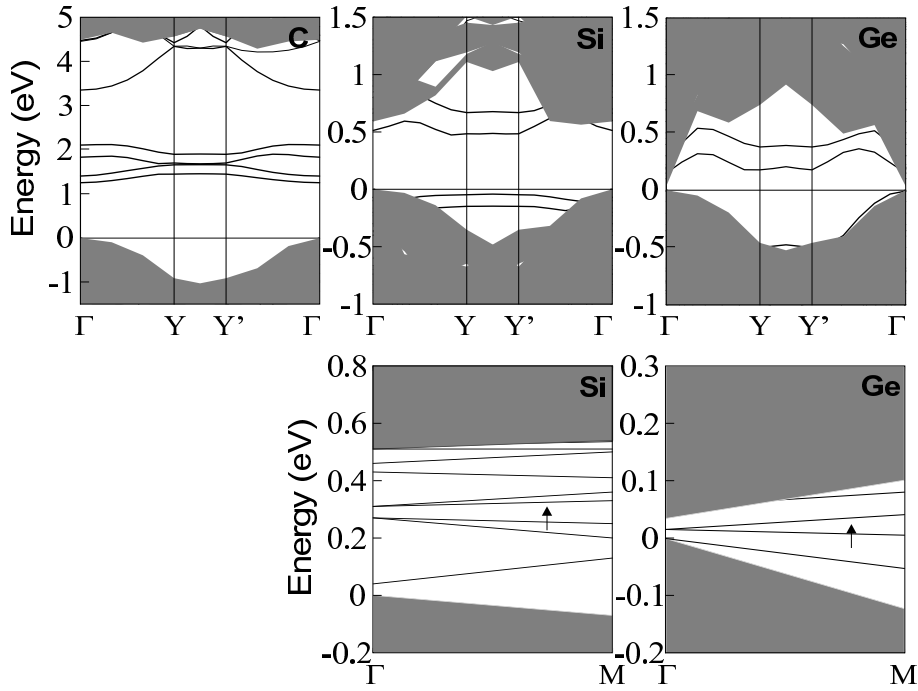


Figure 3.6 Band structures of (111) $c(2\times 8)$ (top panel) and (111) 7×7 (bottom panel) surface reconstructions.

band degeneracy. Along a row $C \rightarrow \text{Si} \rightarrow \text{Ge}$ the gap is opened as a consequence of the chain buckling. The corresponding surfaces for Si and Ge become insulating. The occupied π bands are shifted below the VBM indicating an energy gain due to the band structure contribution. A small indirect energy gap appears along the JK line which is smaller for the chain-left isomers. This fact is accompanied by a slightly higher energy position of the occupied π -band in the chain-left case. This does not allow to explain the energetic preference of the chain-left structure, in particular in the case of germanium, simply by an energy gain due to the band structure energy. Perhaps the changed topology of the five- and seven-fold rings in the layers beneath plays a role. On the other hand, the alignment of the projected bulk band structure and the slab band structure may be accompanied by an inaccuracy of the surface band positions by about 0.1 eV.

The band structures of the (111) $c(2\times 8)$ surfaces are plotted in Fig. 3.6 (top panel) along the high-symmetry directions $\Gamma Y - YY' - Y'\Gamma$ in the BZ of the twodimensional c -rectangular Bravais lattice (see Sec. 2.9). Essentially the dangling bonds belonging to the two adatoms and the two rest atoms appear in the fundamental gap region of the projected bulk band structure. The wave functions of two of these bands are represented in Fig. 3.7. The four bands are clearly observable for diamond because of the weak interaction of the dangling bonds and the similarities of the adatom and rest atom bonding to the underlying atomic layer (cf. Table 3.4). There is only a vanishing surface-state gap. In the silicon case the adatom dangling bonds become more p_z -like whereas the rest atom dangling bonds increase the s -character. This rearrangement is accompanied by an electron transfer from the adatoms to the rest atoms forming a lone

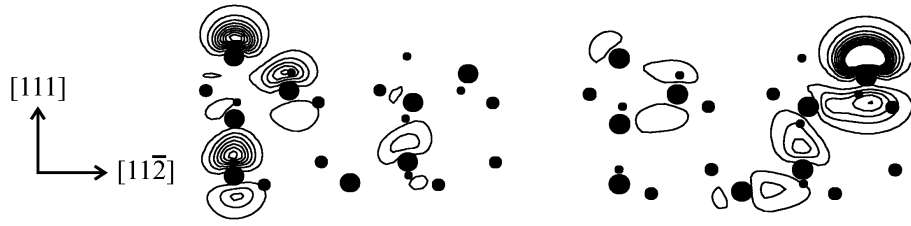


Figure 3.7 Contour plots of surface states of the Ge(111) $c(2 \times 8)$ surface. The wave function squares are represented in a $(1\bar{1}0)$ plane. State of the lowest empty surface band at a wave vector on the ΓY line (cf. Fig. 3.6) mainly localized at a T_4 adatom (left panel). State of the highest occupied surface band close to the VBM at a wave vector at the $\Gamma Y'$ line (cf. Fig. 3.6) mainly localized at a rest atom (right panel). The distance of the Ge atoms to the plane of adatom and rest atom is indicated by varying size of the dots.

pair in the dangling-bond orbital of the rest atom. As a consequence, the surface bands belonging to the rest atoms are close to the VBM of the bulk band structure and, hence, completely filled with electrons. A remarkable gap occurs between the empty and filled dangling-bond states localized at adatoms or rest atoms. In the Ge case, the occupied rest atom bands are further shifted into the projected bulk valence bands. The accompanying energy gain via the band structure energy explains why the $c(2 \times 8)$ reconstruction is more energetically favorable than the π -bonded chain 2×1 reconstruction as well as why this happens in particular for germanium. The adatom-induced elastic energy is obviously overcompensated more strongly by lowering the band-structure energy due to the reduction of the density of dangling bonds in the Ge case. The surface bands are clearly related to the geometry discussed above. Whereas the adatom structure is similar for C, Si, and Ge, there is an increase of the vertical distance of the rest atoms to the atomic layer beneath, (see Table 3.4). It is accompanied by a dehybridization from four sp^3 - to p_x -, p_y -, p_z -, and s -orbitals and, hence, a downshift of the surface bands related to the occupied rest atom dangling bonds.

Figure 3.6 (bottom panel) represents the band structures of the $(111)7 \times 7$ surfaces along a high-symmetry direction in the twodimensional hexagonal BZ (see Sec. 2.9). Explicitly, only the bands at the center point Γ and the point M at the BZ boundary have been calculated. Here we mainly discuss the electronic structure for silicon. We observe several occupied, half occupied and empty surface bands within the fundamental gap of the projected bulk band structure. They belong to the dangling bonds situated at the adatoms, rest atoms and corner-hole atoms [177]. Corresponding selected states are represented in Fig. 3.8. Within the DFT-LDA band structure of Si the surface Fermi level is located at about 0.3 eV above the VBM. The half-filled band that pins the Fermi level shows strong contributions from dangling bonds of adatoms. Dangling bonds localized at rest atoms and corner-hole atoms contribute to the occupied bands just below the Fermi level. The tendency that the occupied dangling bonds of the rest atoms dominate this region of surface states has been also found by other authors [177]. The contribution of dangling bonds situated at adatoms near the corner holes or in the center of the unit mesh are much smaller. The empty surface bands mainly arise from the dangling bonds

of adatoms. The interpretation of the states at the Ge(111) 7×7 surface is more complicated, since the fundamental gap in the projected bulk band structure is so small in DFT-LDA. Only a few surface bands really represent bound states. In the diamond case (not shown in Fig. 3.6) one observes a dense bunch of dangling-bond-derived bands in a mid-gap position. As a consequence of the weak geometrical changes practically all types of dangling bonds contribute to the bunch of surface bands around the Fermi level in the center of the fundamental gap.

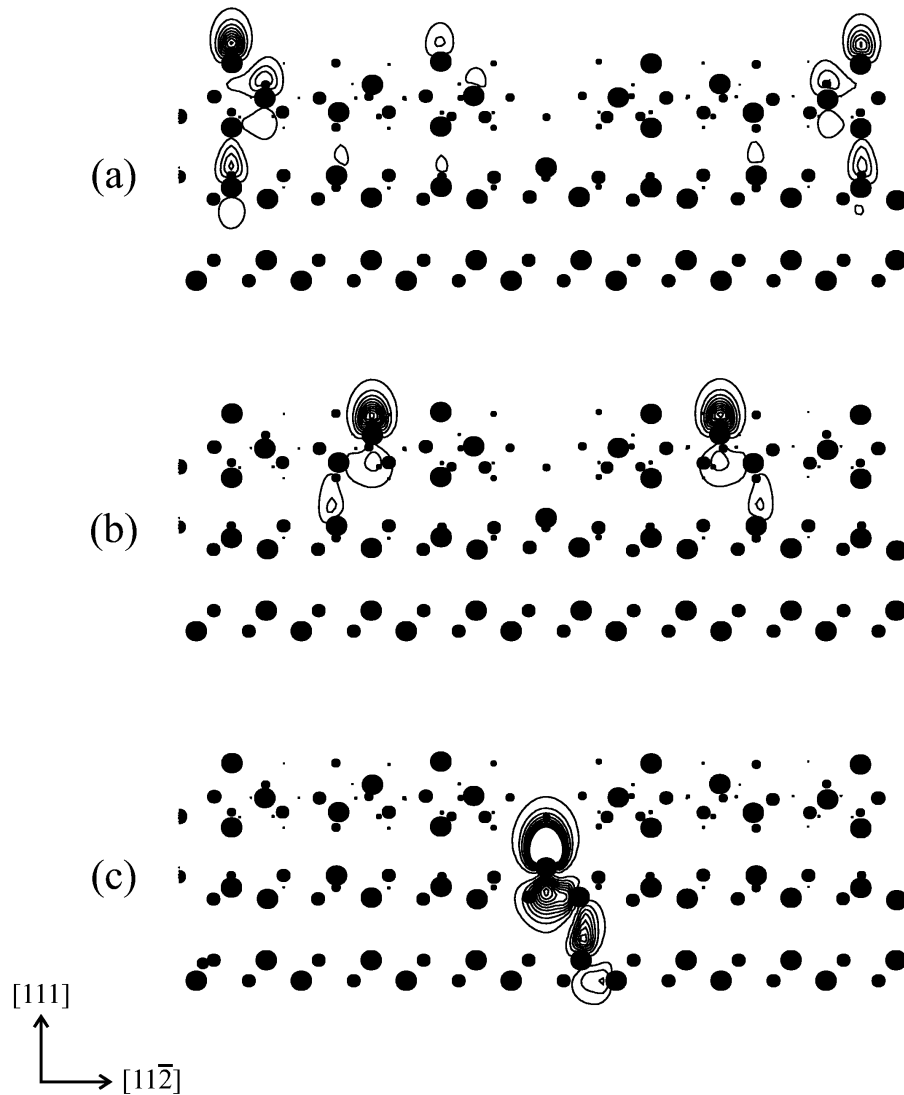


Figure 3.8 Contour plots of surface states of the Si(111) 7×7 surface. The wave function squares are represented in a ($1\bar{1}0$) plane for surface bands plotted in Fig. 3.6. (a) Partially filled surface band in the gap. (b) Occupied slab band just below VBM (not shown in Fig. 3.6). (c) Occupied surface band above VBM.

Chapter 4

High-index surfaces – (113)

4.1 Reconstruction models and structural parameters

A (113) surface of a truncated bulk Ge, Si or diamond crystal consists of alternating (001)- and (111)-like atomic rows in the uppermost double layer [Fig. 4.1(a)]. A 1×1 unit cell contains two atoms. The (001)-like atoms in the upper part of this bilayer are twofold-coordinated and, hence, possess two dangling bonds. The (111)-like atoms in the slightly lower part of the topmost bilayer are threefold-coordinated and, therefore, only have one DB. The DBs are half-filled. According to the general rules [112] such a surface should reconstruct to minimize the DB density and the surface energy.

The two twofold-coordinated atoms may form a dimer along $[1\bar{1}0]$ direction with a characteristic bond length d_{dim} and a possible dimer tilting Δz_{dim} . The dimerization of neighbored (001)-like atoms leads to a 2×1 translational symmetry [Fig. 4.1(b)]. Together with the two adjacent non-rebonded edge atoms they form a trapezoidal tetramer. A possible asymmetry may be characterized by the difference Δz_{edge} of the vertical positions of the two edge atoms. The removal of every third (001)-like atom in $[1\bar{1}0]$ direction gives a 3×1 translational symmetry. The adjacent (111)-like atom rebonds and forms an adatom-like reconstruction element. The adatom is characterized by the displacements Δz_{ad} and Δy_{ad} parallel to the $[113]$ or $[33\bar{2}]$ direction from the bulk-like position. It results an adatom-dimer reconstruction model keeping the 3×1 translational symmetry [Fig. 4.1(c)] [88].

Refinements of the 3×1 AD model such as tetramer tilting or puckering (indicated by Δz_{dim} and $\Delta z_{\text{edge}} \neq 0$) may lower the total energy, but still the electron counting rule [112, 113] cannot be fulfilled. Three partially filled DBs remain. However, if the tetramers [as in the case of Ge and Si(001) $c(4 \times 2)$ or $p(2 \times 2)$ surfaces (cf. Sect. 3.1)] of adjacent horizontal rows are tilted/puckered in opposite direction [88, 106], it results a 3×2 periodicity that allows for pairing of all electrons and, hence, an insulating (semiconducting) surface. [106] The generalized oppositely puckered 3×2 AD(op) structure is shown in Fig. 4.1(c).

The 3×1 AD surface can transform into another 3×1 structure by capturing a self-interstitial atom in the center of the tetramer. It results in a 3×1 AI reconstruction [Fig. 4.1(d)] [84]. The interstitial atom is sixfold-coordinated. Together with the (subsurface) common neighbor (called subatom) of the two edge atoms, the original tetramer forms a nearly flat pentamer around the

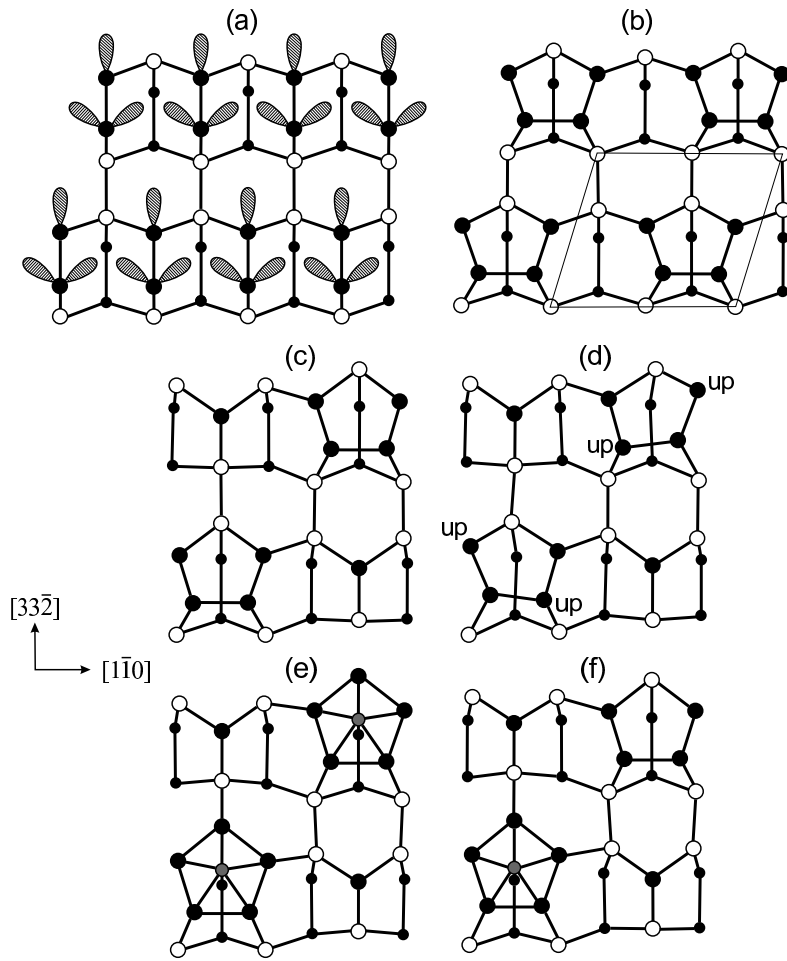


Figure 4.1 Top view of various reconstructions of (113) surfaces. (a) Bulk-truncated surface with indicated dangling bonds, (b) 2×1 model with symmetric tetramers as reconstruction elements, (c) 3×2 AD model, (d) 3×2 AD (oppositely puckered) structure, (e) 3×1 or 3×2 AI reconstruction, and (f) 3×2 ADI model. Filled (open) circles indicate atoms in the top (second) bilayer. Dots represent atoms in the third bilayer. The interstitial atoms are indicated by shaded circles. In (b) a 2×1 unit cell is indicated by thin lines. In (c), (d), (e), and (f) the area of a 3×2 unit cell is shown.

interstitial. The subatom is characterized by the vertical distance to the average position of the edge atoms Δz_{sub} . The interstitial may be characterized by the vertical distance Δz_{in} of this atom to the average position of the atoms in the surrounding pentamer. A possible displacement along the $[1\bar{1}0]$ is represented by Δx_{in} . However, there is also a substantial interaction with the atom beneath in the third bilayer, completing the sixfold coordination. The number of DBs is not reduced with respect to the 3×1 AD surface. Complete electron pairing or completely empty orbitals may occur by allowing an asymmetry associated e.g. with the opposite tilting of neighboring pentamers, or with different vertical positions of atoms in adjacent pentamers. The resulting 3×2 AI reconstruction [also Fig. 4.1(e)] should be insulating. For that reason, we study possible asymmetric 3×2 AI reconstructions. The AD and AI models differ by the weakly

Table 4.1 Absolute surface energies $E_{\text{surf}}^{n \times m}$ and $\gamma^{n \times m}$ for various (113) surface reconstructions.

Reconstruction	E_{surf} (eV/ 3×2 cell)			γ (J/m ²)		
	C	Si	Ge	C	Si	Ge
bulk-terminated	32.28	20.00	15.83	8.34	2.21	1.61
relaxed	26.44	16.71	12.70	6.83	1.85	1.29
2×1 symmetric	19.77	14.46	12.66	5.11	1.60	1.28
2×1 asymmetric		13.23	10.11		1.46	1.03
3×1 AD	21.29	13.49	10.58	5.50	1.49	1.08
3×1 AD(p)		13.37	10.44		1.48	1.06
3×2 AD(op)		13.35	10.42		1.48	1.06
3×1 AI		13.16	9.77		1.45	0.99
3×2 AI		13.11	9.72		1.45	0.99
3×2 ADI		12.69	9.77		1.40	0.99

bonded interstitial atoms. The migration of such atoms is likely, resulting in a certain surface disorder. A stable intermediate structure may only contain one interstitial per 3×2 cell. It results the mixed 3×2 ADI reconstruction shown in Fig. 4.1(e) [84]. Since there is an even number of half-filled DBs, also this combined reconstruction model may describe a non-metallic surface.

4.2 Energetics and geometries

The calculated surface energies are summarized in Table 4.1. Important geometry parameters are listed in Table 4.2. In addition to the most stable reconstruction models with 2×1 , 3×1 and 3×2 translational symmetries with different symmetric and asymmetric variations, we have also studied the bulk-terminated and relaxed (113) surfaces. Relaxation of bulk-terminated surfaces already gives rise for the reduction of the surface energies. Dimerization of two twofold-coordinated atoms leads to further stabilization of the surface structure. The resulting 2×1 reconstruction gains 4.17 (C), 2.26 (Si), and 1.91 (Ge) eV/ 2×1 cell with respect to unrelaxed surfaces. As for the (111) and (100) group-IV semiconductor surfaces asymmetries play an important role also in the case of the (113) surfaces. For C(113) 2×1 a symmetric tetramer is the most favorable reconstruction element. The comparison of the energy for 2×1 with energies obtained for 3×1 reconstruction shows clearly that the 2×1 reconstruction gives the most stable structure of the C(113) surface. With respect to the 3×1 AD structure, there is an additional decrease of the surface energy by about 0.4 J/m². The formation of a symmetric tetramer per three 2×1 cells instead of two adatoms in the case of two 3×1 cells lowers the energy of the diamond surface by 0.51 eV per 2×1 unit cell. This is expected for diamond since adatoms also do not lead to a stable reconstruction of the C(111) surface (cf. Sect. 3.2).

The situation is different for the Si and Ge(113) surfaces. In these cases the low-energy structures with 2×1 translational symmetry are given by puckered tetramers. The tetramer

Table 4.2 Important geometry parameters of 2×1 , 3×1 and 3×2 reconstructions of (113) surfaces of C, Si and Ge (in units of the bulk bond length). In the case of 2×1 translational symmetry values are given for symmetric tetramers for diamond or for asymmetric ones for Si(Ge). Due to the asymmetry in the case of 3×2 AI and ADI two values are given for the left (right) part of the reconstructed unit cell [Fig. 4.1(e) and 4.1(f)]. For 3×2 AD(op) only one value of each tilting parameter Δz_{dim} and Δz_{edge} is given, since the buckling in the opposite tetramer only gives a changed sign.

Reconstruction	Element	Dimer atoms		Edge at.	Subat.	Adatom		Interstitial	
		d_{dim}	Δz_{dim}	Δz_{edge}	Δz_{sub}	Δz_{ad}	Δy_{ad}	Δz_{in}	Δx_{in}
2×1	C	0.99	0	0	-0.22				
	Si	1.01	0.26	0.33	-0.21				
	Ge	0.99	0.27	0.35	-0.22				
3×1 AD	C	0.96	0	0	-0.22	-0.19	-0.29		
	Si	1.00	0	0	-0.21	-0.19	-0.36		
	Ge	1.06	0	0	-0.22	-0.01	-0.34		
3×2 AD(op)	Si	0.99	0.23	0.26	-0.34	-0.19	-0.37		
	Ge	1.01	0.29	0.27	-0.34	0.00	-0.37		
3×1 AI	Si	0.98	0	0	0.00	0.00	-0.28	0.62	0
	Ge	1.00	0	0	0.09	0.04	-0.28	0.63	0
3×2 AI	Si	0.99	0.02	0.06	0.03	0.00	-0.27	0.61	-0.03
		(0.99)	(0.05)	(0.21)	(0.00)	(-0.01)	(-0.25)	(0.60)	(0.10)
	Ge	1.00	0.0	0.01	0.09	0.02	-0.26	0.61	-0.01
		(1.02)	(0.09)	(0.26)	(0.01)	(0.04)	(0.27)	(0.63)	(0.12)
3×2 ADI	Si	1.01	0	0	0.03	-0.01	-0.28	0.62	0
		(0.98)			(-0.19)	(-0.02)	(-0.34)		
	Ge	1.00	0	0	0.08	0.04	-0.29	0.64	0
		(1.06)			(-0.21)	(0.01)	(-0.33)		

atoms belonging to a diagonal pair go up or down with respect to the substrate. The occurrence of asymmetric reconstructions is similar to the observations for the dimer reconstruction of the (001) surfaces and the π -bonded chain reconstruction in the case of the (111) surfaces (cf. Sects. 3.1 and 3.2). Interestingly, the asymmetric tetramers also stabilize the Si and Ge(113) surfaces more than the variety of originally suggested AD models with 3×1 or 3×2 translational symmetries (see Table 3.5). As for the 2×1 reconstruction in the puckered 3×1 AD structure diagonal atoms in the tetramer are buckled towards the same direction. In the oppositely puckered 3×2 AD geometry upper and lower atoms of two tetramers belong to different diagonals. Apart signs, the geometry parameters (cf. Table 4.2) are almost the same for 3×1 AD(p) and 3×2 AD(op) models. Only in the Ge case one parameter is somewhat different for 3×1 and 3×2 unit cells, the buckling Δz_{edge} between the edge atoms (instead of 0.27 it is 0.17 d_{bulk}). The buckling Δz_{edge} is also different (larger) for both Si and Ge in comparison to the 2×1 reconstruction.

Indeed, puckering reduces the surface energy, but only within AD models. For silicon we calculate an energy gain of 0.12 eV per 3×2 unit cell for the 3×1 AD(p) reconstruction. The puckered structure with 3×1 translational symmetry is only slightly higher in energy by 0.02 eV compared with the 3×2 AD(op) reconstruction. Similar energy gains are obtained for germanium (cf. Table 4.1). The 3×1 puckered model lowers the surface energy by 0.14 eV for Ge. The opposite puckering further lowers the surface energy by 0.02 eV, a value of the order of the thermal energy at room temperature. Consequently, a flipping of the tetramers should be already possible at room temperature. A phase transition between 3×1 and 3×2 structures may be easily imaginable in the framework of the AD model as suggested in the literature for Si [101, 106]. The small energy differences also suggest the local coexistence of phases with different translational symmetries as observed in the Ge case [95, 99, 108].

The introduction of self-interstitials on Si and Ge(113) surfaces reduces the energy further in agreement with previous calculations [84, 108]. However, there is a sensitive balance of different energy contributions. For Si(113), the 3×2 ADI reconstruction [Fig. 4.1(f)] with only one interstitial atom per 3×2 unit cell gives the lowest-energy structure. The 3×1 and 3×2 AI structures with more interstitials per unit area are less stable. With respect to the optimized 3×2 AD(op) structure (Table 4.2), the adsorption of an interstitial atom gains energy of about 0.7 eV within the 3×2 ADI model. Due to the repulsive interaction of the interstitials on the short distances this value is reduced to 0.2 eV per interstitial for AI geometries. For Ge the energies of the 3×1 AI and 3×1 ADI models are equal. The novel asymmetric 3×2 AI model gives rise to the lowest energy structure. There is an energetical ordering 3×1 AI/ 3×2 ADI and 3×2 AI, which is different from that observed for Si(113). The repulsive interaction of the interstitials is much weaker in the germanium case. The energy gain of 0.6 eV by adding an Ge interstitial in a 3×2 ADI structure is reduced to 0.3 eV per interstitial in the AI cases.

Within the interstitial models pronounced asymmetries are found only for the 3×2 AI reconstruction (cf. Table 4.1). There is a general tendency to break the symmetry between the two pentamers. Such asymmetries have been observed in STM images for the seemingly 3×1 reconstruction [108]. The unit cell of the 3×2 AI reconstruction is doubled by opposite buckling of the two pentamers, where the interstitial atoms can also change their central positions. Such a staggered arrangement of buckled pentamers lowers the total energy by about 50 meV for Si and Ge and results in the 3×2 AI model. Here we present the most favorable asymmetries which have been found. Other asymmetries, e.g. an average relative vertical displacement of the two pentamers within the 3×2 AI model, also lower the total energy. One observes different local minima on the total-energy surface with practically the same surface energies. The band structures of the two geometries are nearly identical. Particularly for Si the asymmetry opens a gap. The removal of one interstitial, i.e., the transition to the 3×2 ADI structure, further lowers the energy in the Si case but not for Ge(113). For the 3×2 ADI reconstruction an additional asymmetry is not favorable for both materials.

The small energetical differences between ADI and AI models may explain the observed temperature-induced order-disorder phase transitions [91, 94–96, 99, 104, 105, 108]. The low temperature of about 120 K for Ge and the high temperature of about 800 K for Si seem to be correlated with the differences in the corresponding surface energies between AI and ADI

structures. According to the small binding energy of the second interstitial, surface diffusion must play an important role, in particular the migration of the interstitial atoms [108]. Such a migration at a certain temperature may be accompanied by a certain amount of surface disorder and, hence, explains the coexistence of 3×1 and 3×2 reconstructed domains on a given (113) surface [94, 97, 99, 101, 108]. In the Si(113) case the observation of 3×1 instead of 3×2 seems to be also dependent on the density of the surface defects and the bulk doping [89, 93].

The energetical ordering of the reconstruction models in Table 4.1 is the same as in other *ab initio* calculations [84, 92, 106, 108], apart that the 2×1 and asymmetric 3×2 AI structures have not been studied. In particular, interstitial models give the lowest-energy structures. We agree that 3×2 ADI is the lowest-energy structure for Si(113) and with nearly the same energies for all interstitial reconstructions of Ge(113). However, the calculated absolute surface energies per unit area, γ , in Table 4.1 are slightly smaller than those computed by other authors [84, 92, 108]. This holds for both Si and Ge(113).

4.3 Band structures and electronic states

In order to understand the driving forces of the reconstructions and the electronic structures of the (113) surfaces for diamond, Si and Ge, band structures for all important models have been calculated. The corresponding resulting band structures of (113) 2×1 surfaces are plotted in Fig. 4.2 versus the variation of the \mathbf{k} points between high-symmetry points in the surface BZ of the oblique lattice (see Sect. 2.9). The C(113) 2×1 surface with tetramers shows a significant insulating behavior. Two neighbored empty surface bands in the upper part of the projected fundamental gap are well separated from the two completely filled surface bands somewhat below the VBM of the bulk band structure. The indirect energy gap is related to a transition from the ΓP line to the J point and amounts to 2.1 eV within the DFT-LDA, i.e., half the value of the bulk gap. Surprisingly, already the symmetric tetramers give rise to the opening of a surface gap for Si(113) 2×1 , though the gap is small with 0.4 eV. This is not the case for the symmetric-dimer reconstruction of the Si(001) 2×1 surface (cf. Sect. 3.1) for reasons which will be seen discussing the nature of the electronic states below. A gap opening does not occur for symmetric tetramers on Ge(113) 2×1 . However, the prediction of the surface band structure is difficult due to the remarkable band-gap underestimate within the DFT-LDA already for bulk Ge. In any case, for Si and Ge there is a tendency to open the surface gap by puckering of the tetramers. The occupied bands, in particular for Ge, are shifted into the projected valence bands and only an empty surface state band remains in the projected fundamental gap. However, due to its strong dispersion the Ge(113) 2×1 surface with asymmetric tetramers remains metallic. The low position and the strong dispersion of the lower surface band for Ge(113) 2×1 is a consequence of the bulk electronic structure. The bulk conduction-band states arising not far from the L point in the fcc BZ repel the surface band at J (which is in contrast empty for C and Si) towards lower energies even below the VBM. The general tendency of shifting the surface bands and opening gaps between surface states with the asymmetry of the tetramers is

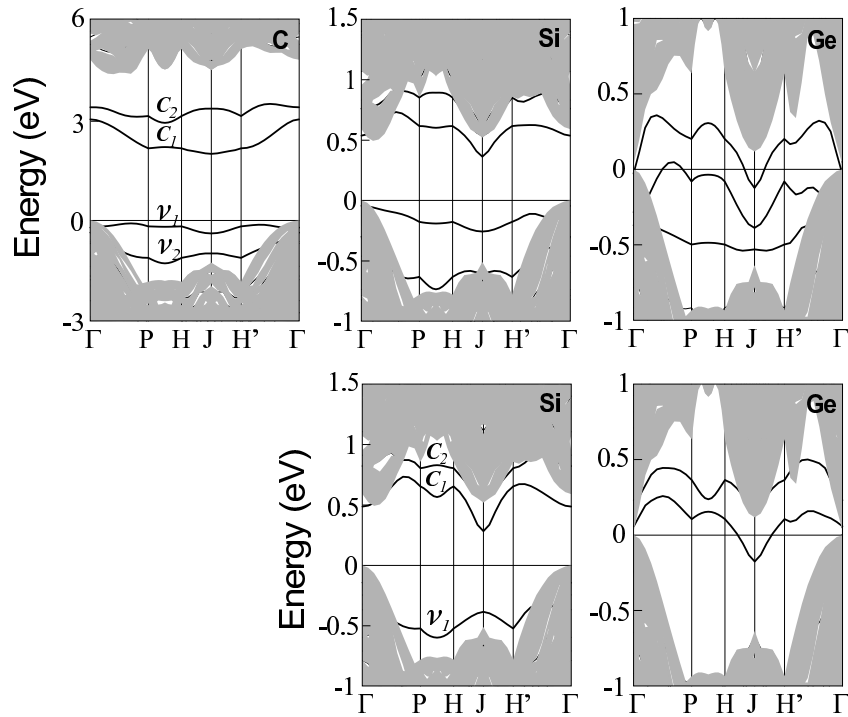


Figure 4.2 Electronic band structures of C, Si and Ge(113) 2×1 surfaces. The band structures in the upper panels are calculated for symmetric tetramers, while the lower ones represent asymmetric tetramers.

in agreement with similar findings for the (111) and (001) low-index surfaces of Si and Ge (cf. Sects. 3.1 and 3.2).

The physical/chemical origin of the surface bands is indicated in Figs. 4.3 and 4.4. The squares of the wave functions are plotted for the two lowest empty surface bands and the two highest occupied surface bands for symmetric tetramers [C(113) 2×1 , Fig. 4.3] and asymmetric tetramers [Si(113) 2×1 , Fig. 4.4]. The character of the four surface bands within the fundamental gap is dominated by the six dangling-bond orbitals situated at the four tetramer atoms (one on each (111)-like atom (or edge atom) and two on each (001)-like atom (or dimer atom) of the tetramer) as indicated in Fig. 4.1(a) for the surface atoms in bulk positions. Their linear combinations form the surface-state wave functions. Even for the symmetric case of diamond, the two sp^3 orbitals of each (001)-like atom cannot be dehybridized in such a way forming σ and π orbitals with respect to the directions $[113]$ and $[1\bar{1}0]$ as in the classical dimer picture of (001) surfaces [48]. In contrast to (111) and (001) surfaces with exact π and σ orbitals, six sp^3 -like dangling bonds have to be discussed to explain the electronic structure of the tetramer.

As a consequence, for diamond only one bond along the $[1\bar{1}0]$ direction is nearly formed by two sp^3 -like orbitals located at (001)-like atoms. The remaining dangling bonds strongly interact with the dangling bonds of the neighbored (111)-like edge atoms of the tetramer. In the case of C(113) 2×1 the distance of the two (001)-like atoms in the tetramer amounts 99% (Table 4.1) of a bulk bond length d_{bulk} . This is in contrast to a dimer bond length $0.90 d_{\text{bulk}}$

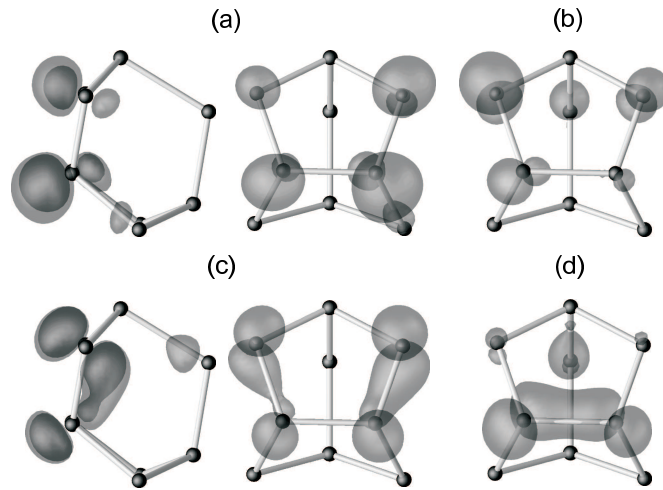


Figure 4.3 Wave-function squares of the lowest unoccupied c_2 (a), c_1 (b) and highest occupied v_1 (c), v_2 (d) surface bands at P for the C(113) 2×1 reconstruction. In (a) and (c) cases side views are additionally plotted in the left panels in order to show the contributions below the tetramer plane.

calculated for C(001) 2×1 (Table 3.2). Interestingly the two bond lengths between edge and dimer atoms in the tetramer are reduced to $0.89 d_{\text{bulk}}$. The reason is a true dimer-like behavior of two such atoms. Already in the bulk case a σ bond exists. An additional bond is formed by the two dangling hybrids of the edge and dimer atoms. No asymmetry occurs in the tetramer because of the strong bonding between the carbon atoms which takes place due to the lack of p and d electrons in the atomic core. The tetramers nearly show a mirror symmetry along $[3\bar{3}\bar{2}]$. They are almost planar. Only a small difference of 0.22 \AA remains between dimer and edge atoms along the z direction as an artifact of the atomic positions in the bulk-terminated surface. As a consequence of the weak bonding of the so-called dimer atoms, the occupied tetramer states in Fig. 4.3(c) and Fig. 4.3(d) are governed by antibonding (bonding) combinations of dangling orbitals at dimer atoms and bonding (antibonding) combinations of dangling orbitals located at edge and dimer atoms. However, there are also contributions from the orbitals around the central atom below the tetramer. The unoccupied states are dominated by antibonding linear combinations of dangling bonds located at the dimer and edge atoms.

Because of the most favorable asymmetric (puckered) tetramer structures the surface states are completely changed for the Si and Ge(113) 2×1 surfaces. A tetramer does not anymore form a planar structure. Starting from the left edge atom, approaching the two so-called dimer atoms, and going around to the second edge atom one finds the following variations Δz in the vertical positions, 0, 0.91, 0.29, and 0.77 \AA (0, 0.98, 0.33, and 0.86 \AA) for Si (Ge). The dimer bond length between two (001)-like atoms amounts to 1.01 (0.99) d_{bulk} , whereas the lengths between (111) and (001) atoms are 0.97 (0.95) d_{bulk} for Si(113) [Ge(113)]. For Si(113) 2×1 the wave-function squares of the surface states are shown in Fig. 4.4. Because of their similarity those for Ge are not plotted. The consequence of the asymmetry of the tetramers is obvious.

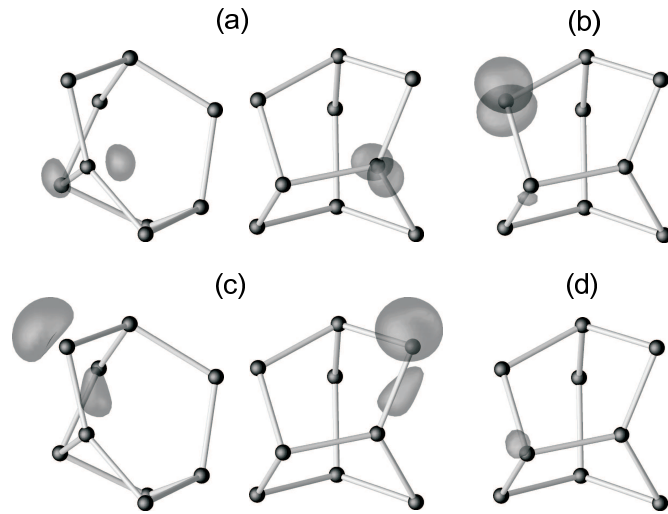


Figure 4.4 Wave-function squares of the lowest unoccupied c_2 (a), c_1 (c) and highest occupied v_1 (c), v_2 (d) surface bands at P for the asymmetric tetramer reconstruction of the Si(113) surface. The band v_2 (d) occurs in the projected band structure of the valence bands and, hence, is not indicated in Fig. 4.2. In (a) and (c) side views are also plotted in the left panels.

The different surface states at the P point in the BZ are mainly due to orbitals located at one tetramer atom. The two lowest unoccupied states are localized at the two down atoms forming a diagonal of the tetramer. The two considered occupied states are mainly localized at the two upper atoms. Energetically the lowest one lies already in the projected bulk band structure (cf. Fig. 4.2). The situation shows similarities to the asymmetric-dimer reconstruction of the Si(001) 2×1 surface. The outgoing atoms become a more s -like dangling orbital, whereas the atoms displaced towards the substrate show a more p_z -like character of the dangling orbital. Electron transfer from the more p_z -like orbitals into the more s -like orbitals is expected to lower the total energy of the system.

Electronic band structures of different 3×1 and 3×2 surface reconstructions for Si and Ge(113) surfaces are plotted in Fig. 4.5. In principle, a similar behavior is observed for Si and Ge. Similar to the 2×1 case, modifications are related to differences in the bulk band structures. For Ge a small direct gap at Γ and a conduction-band minimum (CBM) at L instead of at $0.85 \Gamma X$ are found. The minima at L points are responsible for the deep projected conduction bands at the K point of the surface BZ. Moreover, the weaker bonding in Ge plays a role. The 3×1 AD model [Fig. 4.5(a)] clearly gives a metallic behavior of the (113) surfaces in agreement with the three half-filled (without buckling) DBs. DB-related bands overlap partially with bulk states near the VBM. The Fermi level at an energy near the VBM crosses these bands. A similar behavior is observed for the lowest-energy AD structure of the C(113) 3×1 surface. The metallic character remains true for the puckered AD, but surprisingly also for the oppositely puckered 3×2 AD structures [Fig. 4.5(b)]. The DBs at the adatoms still weakly interact and the splitting of the two bands due to asymmetric displacements and DB interaction is too small. This is in contrast to the band structure obtained within a TB approximation by Wang

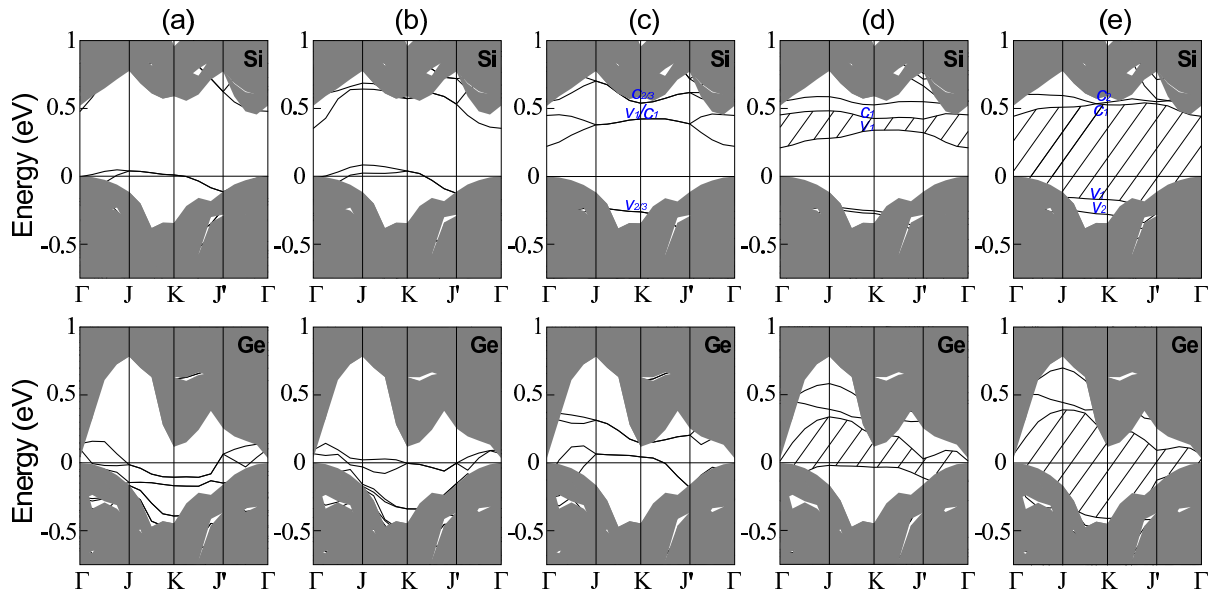


Figure 4.5 Band structures of Si and Ge(113) surfaces. The shaded regions indicate the projected bulk band structures. Surface bound-state bands are shown as solid lines. Fundamental gaps between such states are represented as hatched regions. (a) 3×1 AD, (b) 3×2 AD(op), (c) 3×1 AI, (d) 3×2 AI, and (e) 3×2 ADI. In all cases the BZ of the 3×2 reconstruction is used for the presentation. For Si(113) in (c), (d), (e) surface bands are denoted by v_i and c_i .

et al. [106]. A surface-state gap of about 1 eV [106] would require remarkable differences in the s - and p -character of the two DBs at the adatoms. Still partially-occupied states belong to adatoms, and there is not a significant tendency to transfer electrons from tetramers to the adatoms.

Adding a surface self-interstitial but keeping the 3×1 translational symmetry in the 3×1 AI structure, no change in the metallicity occurs. In the upper part of the fundamental gap in the projected bulk band structure, it appears a half-filled band pair that is degenerate along the BZ boundaries and pins the Fermi level [Fig. 4.5(c)]. However, giving the system more degrees of freedom in a 3×2 AI structure and allowing an asymmetric behavior of the two pentamers in the 3×2 unit cell (relative vertical displacement and/or opposite buckling) the degeneracy is lifted and a surface-state gap appears [Fig. 4.5(d)]. The fully occupied band moves down in energy. Therefore, the stabilization of the 3×2 translation symmetry with respect to the 3×1 one, in Table 4.1, can be explained by an accompanying gain of band-structure energy. The removal of one interstitial atom within the 3×2 ADI reconstruction model increases the asymmetries in the 3×2 unit cells. The insulating or semiconducting character of the surface is increased by further opening of the surface-state gap for both Si and Ge(113) [Fig. 4.5(e)]. The highest occupied surface-state band completely moves below the VBM. There is only a measurable total-energy gain for Si (Table 4.1), which is related to the lowering of the band-structure energy. Whereas for the 3×2 AI model the highest occupied surface-state bands appear in a midgap position, this band occurs below the VBM in the 3×2 ADI case.

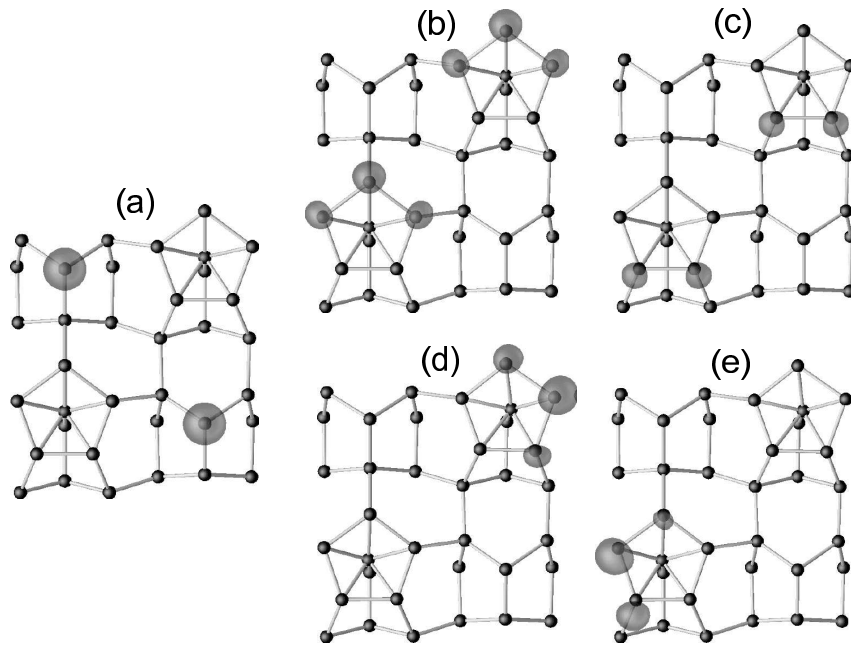


Figure 4.6 Wave-function squares of the highest occupied and lowest unoccupied surface bands at K for the Si(113) surface within the 3×1 and 3×2 AI reconstructions. (a) two fully occupied states $v_{2/3}$, (b) half-occupied v_1/c_1 and (c) lowest conduction states $c_{2/3}$ of 3×1 AI model. (d) and (e) highest occupied (v_1) and lowest unoccupied (c_1) bands of 3×2 AI surface reconstruction. Corresponding electronic structures with band indication are shown in Figs. 4.5(c) and 4.5(d).

The findings of a semiconducting behavior of Si(113) 3×2 surfaces are in agreement with Photoemission Spectroscopy (PES), Angle-Resolved Photoelectron Spectroscopy (ARPES), and STM studies. PES of Ranke and Xing [178] gave the Fermi level in a midgap position of about 0.5 eV above the VBM. This energy region was shown to be free of occupied surface states as demonstrated in Fig. 4.5(e) for the 3×2 ADI structure. At normal emission and at higher emission angles ARPES [102] found two surface bands separated by 0.4 eV below the VBM in a \mathbf{k} -vector direction parallel to $[1\bar{1}0]$. Along JK but also along $J'\Gamma$ (but within the bulk states), we also observe such a pair of surface states in Fig. 4.5(e). Their splitting is smaller than the measured value. One reason may be the neglect of the quasiparticle corrections. Differential tunneling conductance spectra taken at various sites in the 3×2 unit cell on topographic images for both positive and negative voltages also indicate the existence of surface states for Si(113) 3×2 [89]. A broad occupied surface-state feature is observed 0.8 eV below the Fermi level in agreement with PES [179] or 1 eV in Ref. [105]. The gap of about 1.2 eV is almost free of surface states in agreement with the calculations for 3×2 ADI.

As in the case of 2×1 reconstructions the interpretation and identification of the surface bands is more complicated for the Ge(113) surface. However, away from the Γ point the situation becomes clear. The slab band structures show a small gap for both the 3×2 AI and the 3×2 ADI models [Figs. 4.5(d) and 4.5(e)]. The resulting semiconducting behavior is also confirmed

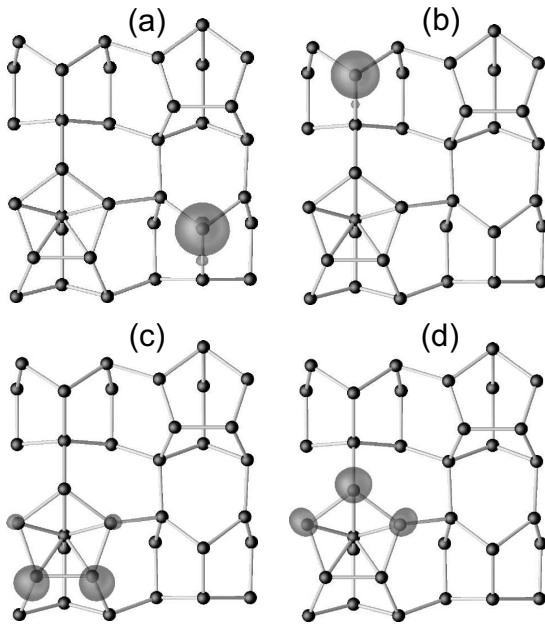


Figure 4.7 Wave-function squares of the highest occupied (v_2, v_1) [(a) and (b)] and lowest unoccupied (c_1, c_2) [(c) and (d)] surface bands at K for the Si(113) surface within the 3×2 ADI reconstruction [see Fig. 4.5(e)].

by PES measurements which found the VBM to be 0.22 eV below the Fermi level and this energy region free of surface states [180].

In order to figure out the true nature of the surface-state bands in the fundamental gap of the projected bulk band structure, the wave functions of the highest occupied (v_1, v_2, v_3) and lowest unoccupied (c_3, c_2, c_1) surface bands are plotted in Figs. 4.6 and 4.7. 3×1 and 3×2 interstitial reconstructions of the Si(113) surface are studied at the K point in the BZ of the 3×2 lattice. At least for Si(113) the states at K are well separated from the bulk states and, hence, show a remarkable localization. In the Ge case there is an energetical overlap of the empty surface bands with the bulk conduction bands at K . Figure 4.6(a) shows for the 3×1 AI model that the two degenerate surface bands $v_{2/3}$ below the VBM are localized at the adatoms and that each DB of an adatom is completely filled. This filling indicates the main effect of the presence of the interstitials. The DBs at the adatoms are filled and, consequently, adatoms move up (see Table 4.2). The wave functions of the half-filled bands v_1/c_1 in the upper part of the fundamental gap [Fig. 4.5(c)] are localized at edge atoms and the subatoms which are originally situated in the third atomic layer. Originally the edge atoms possess half-filled dangling bonds. However, the occurrence of a probability to find electrons at the third-layer atom is somewhat unexpected. That means, this atom is not anymore completely fourfold-coordinated. Rather, because of the presence of the interstitial one bond is weakened, allowing the atom in the fourth atomic layer to form a bond with the interstitial atom. Higher states which appear in the gap ($c_{1/2}$) are localized on the dimer atoms [Fig. 4.6(c)].

The asymmetry in the two pentamers of the 3×2 AI reconstruction governs the gap opening [Fig. 4.5(d)]. The atoms of the pentamer which is closer to the substrate tend to have more p -like DB states. An electron transfer happens from the electronic states localized at this pentamer into the more s -like states at the pentamer that is somewhat displaced away from the bulk. The difference of buckling in the pentamers also plays a role (cf. Table 4.2). Nevertheless, the

atoms with higher positions are more filled and contribute to the v_1 [Fig. 4.6(d)]. The lowest conduction-band states c_1 are localized at the second pentamer [Fig. 4.6(e)]. The higher states should be observable at the lower parts of the pentamers (not shown).

For the 3×2 ADI model the filled and empty surface states v_1, v_2 and c_1, c_2 are shown in Fig. 4.7. The occupied states in Fig. 4.7(a) and 4.7(b) are again localized at adatoms. The empty states belong to the pentamer [Fig. 4.7(c) and 4.7(d)]. Surprisingly, the wave functions around the subsurface interstitial do not contribute to the surface-state bands in the gap. For that reason, they are not visible in STM measurements for not too large voltages [84, 92].

4.4 STM images

The different contributions of the empty and filled electronic states localized at the pentamers, tetramers and the two rebonded adatoms in a certain 3×2 interstitial surface reconstruction will also dominate the STM images. This is demonstrated in Fig. 4.8 for voltages corresponding to energy intervals of 2 eV below or above the theoretical Fermi level within the fundamental gap in DFT-LDA quality. Results are for Si(113), the 3×2 AI structure in Fig. 4.8(a) and the 3×2 ADI reconstruction in Fig. 4.8(b). Those for Ge(113) are very similar. The main differences are due to the strength of the buckling within the 3×2 AI reconstruction.

The resulting STM images are in accordance with the discussion of the orbital character of the gap states in Fig. 4.6 and 4.7. Figure 4.8(a) for the 3×2 AI model clearly shows that the filled-state images are dominated by the wave functions localized at the adatoms. The two pentamers are less visible. However, the right part of the upper pentamer shows brighter spots. They are related to the pronounced asymmetry of the two pentamers. The empty-state images show an opposite behavior. The pentamers are clearly visible whereas only weak contributions are associated with the adatoms. The asymmetry in the upper pentamer is indicated by somewhat smeared-out spots. The interstitial atoms are not visible. In principle such nonsymmetric pentamers are observed experimentally for seemingly 3×1 areas of the Ge(113) surface [108]. Although the asymmetry can be seen there, it is difficult to distinguish whether the 3×1 or 3×2 AI reconstruction appears on the surface, at least in empty-state images. Consequently it is also difficult to distinguish between 3×1 or 3×2 translational symmetries using a local method such as STM.

The observation of pentamer-like structures in empty-state images [89, 93, 107] should be taken as an indication for an interstitial. This is clearly shown in Fig. 4.8(b) for the 3×2 ADI model by the differences between spot arrangements related to pentamers or tetramers. The dimer atoms in the upper-right feature appear in both empty-state and filled-state images, whereas the pentamer is more (empty-state) or less (filled-state) visible. More in detail, the filled-state image is dominated by electronic states localized at the adatoms, as in the case with two interstitials, i.e., the 3×2 AI (or 3×1 AI) reconstruction. For Si(113) 3×2 [93], as well as Ge(113) 3×2 [108], such filled-state images have indeed been observed. The adatoms get electrons from the pentamers to fill their partially occupied states. In the empty-state image [Fig. 4.8(b), right] the adatoms are not seen. The pentamer can be well identified, while the

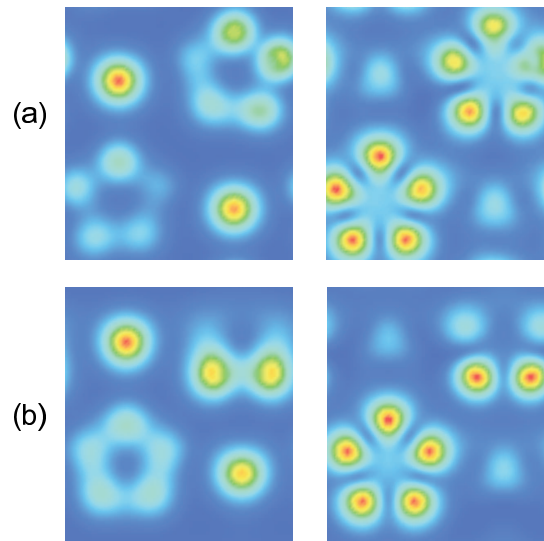


Figure 4.8 STM images of filled (left panel), and empty (right panel) states simulated for the 3×2 AI model (a) and 3×2 ADI model (b) of Si(113) surface for voltages corresponding to -2 and 2 eV with respect to the theoretical Fermi level.

tetramer is only partially visible due to empty π^* dimer states. Images of this type have been observed for Si(113) 3×2 surfaces and voltages of 3 V [93] (see Fig. 4.9). The observation of the dimer in the tetramer in both images is related to the bonding and antibonding π states of these atoms discussed above. This is not surprising since the corresponding bands do not appear in the fundamental gap and are resonant with the projected bulk band structure. Therefore, for smaller voltages the dimers (and the entire tetramers) should be less visible in both filled-state and empty-state images. One also has to mention that the images have been calculated assuming the constant-height mode and not a constant-current mode, and that the energy interval of 2 eV used in the calculations of the images means a larger value for the experimental voltage, since the quasiparticle gap opening is not taken into account.

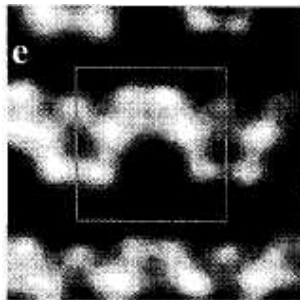


Figure 4.9 Topographic STM image of Si(113) surface corresponding to 3 V of sample bias voltage and 4 nA of the tunneling current (from Ref. [93]).

Chapter 5

Low-index surfaces II – (110)

5.1 Translational symmetry of (110)16×2 surfaces

Clean Si(110) [at certain conditions [80, 81] also Ge(110)] surfaces exhibit 16×2 reconstructions. It was found by using High-Energy Electron Diffraction (RHEED) or LEED in the corresponding patterns, superstructure spots divide the two fundamental spots into 16. Using the basis vectors $\mathbf{a} = (-1, 1, 0)a_0/2$ and $\mathbf{b} = (0, 0, 1)a_0$ (a_0 - bulk lattice constant) of the two-dimensional rectangular Bravais lattice with 1×1 unit cells (see Fig. 5.1), the 16×2 structure has to be described as $\sqrt{171}\times\sqrt{6} - R(32.73^\circ, 35.26^\circ)$ surface within the Wood notation or as

$$\begin{pmatrix} 11 & -5 \\ 2 & 2 \end{pmatrix}$$

within matrix notation [44]. The unit cell of the resulting oblique lattice with the primitive basis vectors $\tilde{\mathbf{a}} = (-11, 11, -10)a_0/2$ and $\tilde{\mathbf{b}} = (-1, 1, 2)a_0$ is also shown in Fig. 5.1. There is a deviation of 2.5° of the first vector $\tilde{\mathbf{a}}$ from the vector $(-1, 1, -1)16a_0/3$ giving rise to a rectangular unit cell. Nevertheless, we still use the denotation “16×2 reconstruction”, since the unit cell area actually amounts to 32 unit cell areas of the 1×1 surface.

5.2 Bond-rotation/bond-contraction relaxation mechanism

A 1×1 unit cell of (110) surfaces consists of two atoms with one dangling bond at each atom connected by two in-plane bonds, introducing in this way a zigzag chain (cf. Fig. 5.2). In the case of zinc-blende crystals where (110) is the cleavage face this bulk-terminated (1×1) translational symmetry is preserved. After the relaxation surface atoms possess asymmetric positions, one atom goes up while the other one moves down, thereby introducing a buckled chain. The relaxation is characterized by a so-called bond-rotation or bond-contraction model in dependence on strength and ionicity of the bonds [181]. These chains are characterized by a bond length d_{chain} and a buckling Δz of the two atoms in a 1×1 unit cell. Basically the same type of relaxation may occur in the case of the group-IV elements. Table 5.1 shows that in the diamond-structure case the Si and Ge(110)1×1 surfaces are clearly described by the bond-rotation mechanism. The bulk bond lengths are conserved but substantial chain bucklings are

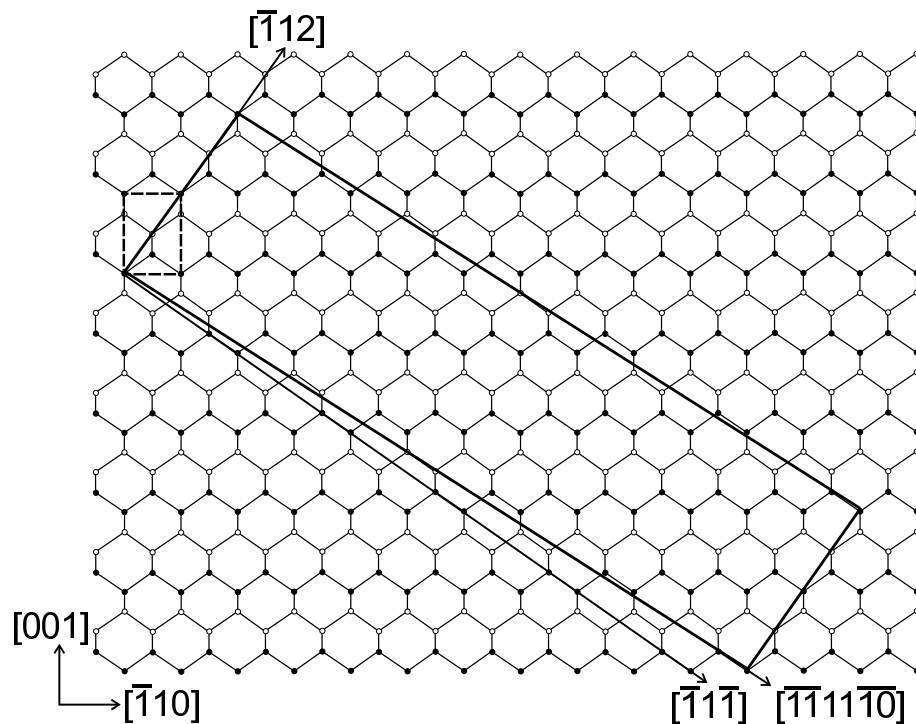


Figure 5.1 Top view of a bulk-terminated (110) surface with 1×1 (dotted line) and possible 16×2 (solid line) unit cells. Dots (circles) represent first(second)-layer atoms. The directions of the primitive basis vectors of the 1×1 and 16×2 lattices are indicated. The deviation from the rectangular lattice is demonstrated by the small difference in the directions $[\bar{1}111\bar{1}0]$ and $[\bar{1}1\bar{1}]$.

predicted. Diamond(110) 1×1 exhibits the opposite behavior, i.e., it is characterized by a bond-contraction relaxation mechanism. There is no buckling but a remarkable shortening of the chain bonds. In any case relaxation gives rise to an energy gain (cf. Table 5.2)

Figure 5.3 presents the bands of the clean relaxed (110) 1×1 surfaces together with the projected bulk band structures. The two dangling bonds per surface unit cell lead to two bands, which are situated within the projected bulk fundamental gap. In the diamond case the two dangling bonds remain equivalent. Consequently the two bands degenerate along the MX line, i.e., perpendicular to the surface chain orientation. The bands split along the other BZ boundary MX' . Along the ΓX and $\Gamma X'$ directions the surface bands exhibit a remarkable dispersion.

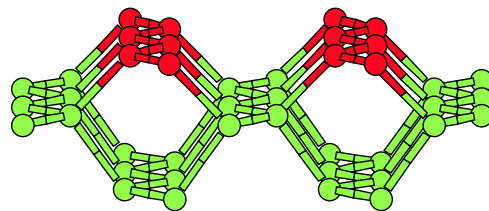


Figure 5.2 Perspective view of zigzag chain on the (110) surfaces.

Table 5.1 Geometry parameters of (110)1×1 reconstruction. Lengths are given in units of the bulk bond length. The chain buckling (rotation) is also characterized by the tilt angle ω (in degrees).

Geometry parameter	Diamond	Silicon	Germanium
ω	0.0	19.6	19.8
Δz	0.00	0.33	0.34
d_{chain}	0.93	0.99	1.00

Table 5.2 Absolute surface energies $E_{\text{surf}}^{n \times m}$ and $\gamma^{n \times m}$ for various (110) surface reconstructions.

Reconstruction	E_{surf} (eV/1×1 cell)			γ (J/m ²)		
	C	Si	Ge	C	Si	Ge
bulk-terminated	4.12	2.63	2.13	7.48	2.04	1.52
1×1-relaxed	3.26	2.19	1.66	5.93	1.70	1.19
1×2-chain		2.18	1.64		1.69	1.17
16×2-chain		2.19			1.70	
16×2-chains on terraces		2.17			1.69	
2×1-adatom		2.14	1.59		1.66	1.14
c(2×2)-adatom		2.26	1.84		1.76	1.32
3×1-adatom		2.09	1.72		1.63	1.23
3×2-adatom		2.23	1.81		1.72	1.29
16×2-adatom-1		2.24			1.74	
16×2-adatom-2		2.16			1.68	
6×2-adclusters		–	–		–	–
16×2-hexagon		2.45			1.90	
3×2 ATI		2.09	1.61		1.63	1.15
16×2 TI		2.24			1.74	
16×2 ATI		2.14			1.66	

Consequently the C(110)1×1 surface is metallic. Along the row C→Si→Ge the chemical trend is similar to that in the (111)2×1 case (cf. Sect. 3.2). The chain buckling (cf. Table 5.1) lifts the degeneracy of the two bands along MX . However, in the Si case the effect is not strong enough. The Si(110)2×1 surface becomes semimetallic. For Ge(110)2×1 a true surface-state gap is opened along the MX line. On the other hand, the bands are shifted towards the occupied bulk bands and the uppermost band exhibits a strong dispersion as a consequence of the interchain interaction. It also results a semimetallic surface electronic structure.

For Si and Ge(110) surfaces a bond-rotation or bond-contraction relaxation mechanism is not the most favorable one assuming not too differing translational symmetries. A more stable

reconstruction with parallel chains buckled in opposite directions is presented in Fig. 5.4(a). This 1×2 reconstruction is energetically more favorable than the relaxed 1×1 one for both materials. The energy gains due to the various buckling contributions of the chains are only of the order of 10 meV for Si and slightly larger for Ge (about 20 meV) (see Table 5.2). The surface stabilization in a 1×2 reconstruction by chains in anti-phase agrees with previous theoretical findings [85, 86]. The values of the buckling amplitudes are 0.75 and 0.80 Å for Si and Ge, respectively. The preference of the 1×2 reconstruction can be related to a gain of band-structure energy. The corresponding electronic band structures are plotted in Fig. 5.5(a). In contrast to the findings for the relaxed 1×1 surface (cf. Fig. 5.3), the alternate buckling of parallel chains in the 1×2 reconstruction opens a fundamental band gap between surface bands. For Si a small gap is observed along the $J'K$ direction. The interchain interaction is effectively reduced. The band folding together with the repulsion of bands decrease the band dispersion in chain direction. For Ge the band structure in Fig. 5.3(a) still indicates a metallic behavior. However, the interpretation of the Ge electronic states is more difficult because of the underestimation of the band gaps within the DFT-LDA already for bulk, as discussed above. The dispersion of the surface bands in Fig. 5.3 is not too large, and the bands mostly overlap near the Γ point. There may be a chance to open a gap using the quasiparticle approach. This also holds for other Ge surface reconstructions discussed below. In contrast to the Ge case the Si(110) 1×2 surface with oppositely buckled parallel chains is semiconducting. The dispersion of the surface bands near Γ is much weaker. For Si(110) 1×2 the squares of the wave-functions at K are shown for the highest occupied and lowest unoccupied states in Fig. 5.6. The principal behavior is similar to the case of equally buckled chains in 1×1 cells. The states localized on upper atoms are fully occupied and behave as s -like orbitals, while those on lower atoms are empty and have p_z -like character. The surface states are similar for Ge (not shown).

Another 1×2 reconstruction may be related to a phase-shifted arrangement of π -bonded dimers [83], due to the rebonding of dangling bonds of neighboring first-layer atoms belonging to the same chain along the $[1\bar{1}0]$ direction (not shown). The total-energy optimization showed that such dimer arrangements are not stable. During the atomic relaxation the starting dimer configuration is transformed back into a chain structure. The reason is that it is not favorable

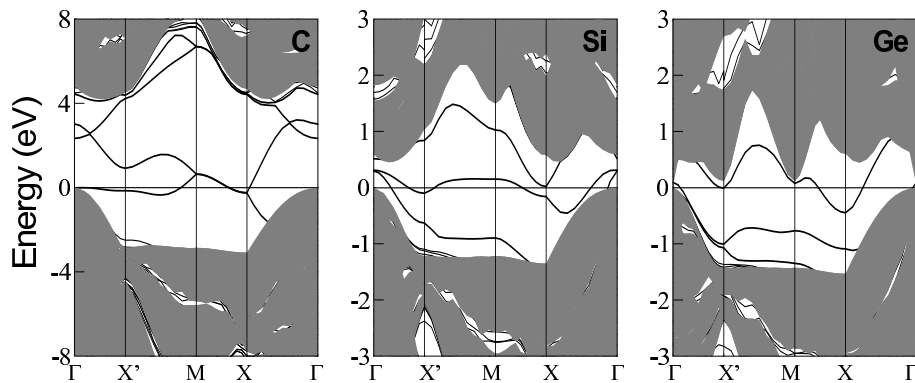


Figure 5.3 Band structure of relaxed (110) 1×1 surfaces.

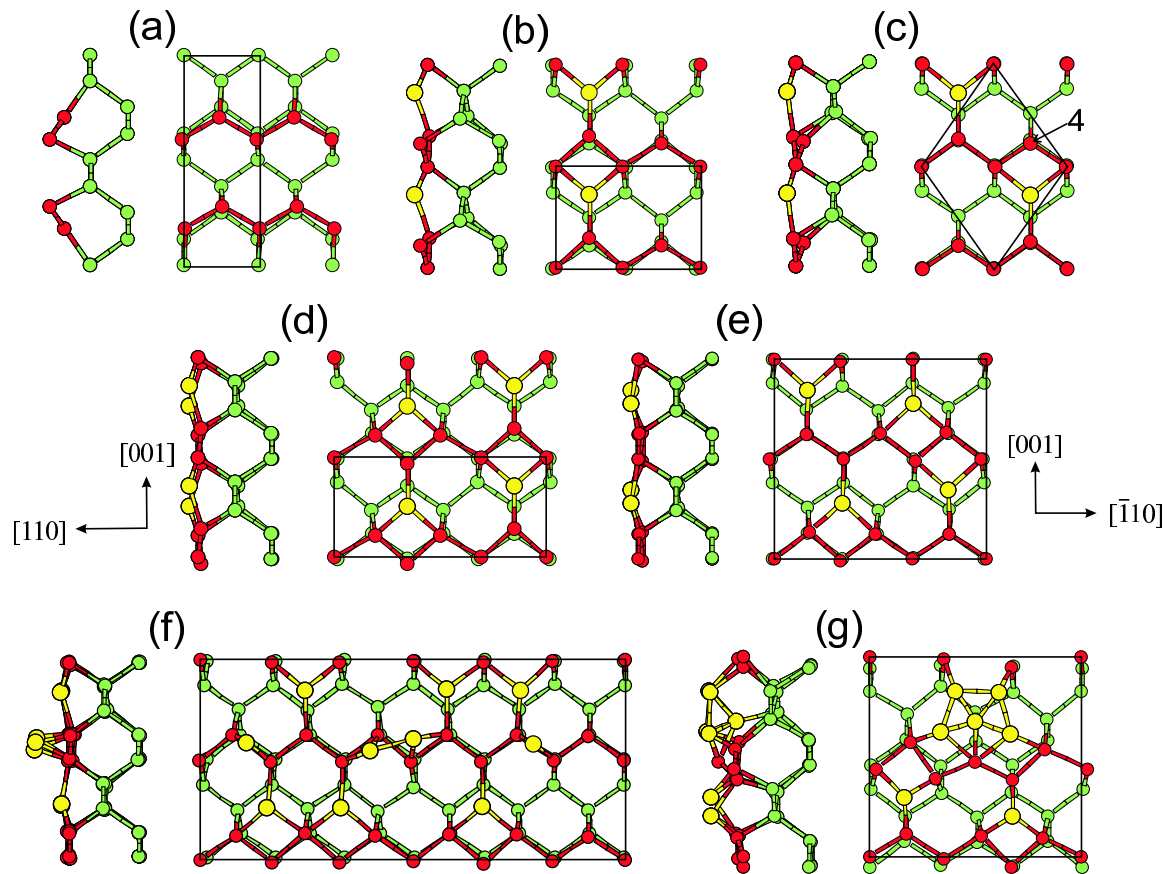


Figure 5.4 Side and top views of relaxed atomic positions of Si(110) surfaces (those for Ge are similar): (a) 1×2 chain buckled model, (b) 2×1 adatom model, (c) $c(2 \times 2)$ adatom model, (d) 3×1 adatom model, (e) 3×2 adatom model, (f) 6×2 five-membered adatom model, and (g) 3×2 adatom-tetramer-interstitial model. Lateral unit cells are indicated by thin solid lines in the top views.

to break a σ bond which already exists and to create a dimer with a π bond which is weaker. Consequently, it is not possible to cover Si and Ge(110) surfaces by neighboring dimers.

The next important point in the understanding of (110) surfaces, in particular of Si(110) 16×2 , is related to study of the step configuration observed by STM. First we have studied a Si(110) 16×2 reconstruction using the bond-rotation relaxation model where chains are buckled in one direction like in nominal 1×1 cell. It gives an idea about the convergence of the total-energy and force calculations using the 16×2 oblique Bravais lattice with primitive vectors $\tilde{\mathbf{a}}$ and $\tilde{\mathbf{b}}$ indicated in Fig. 5.1. The energy gain of 0.44 eV per 1×1 unit cell (cf. Table 5.2) is the same value as computed using the 1×1 rectangular Bravais lattice with primitive vectors \mathbf{a} and \mathbf{b} .

A structure with two terraces and two steps in a 16×2 unit cell can be prepared by removing one half of the first-layer atoms along the $[\bar{1}12]$ direction. However, a simple relaxation of the atoms on both terraces as in the 1×1 case yields an energy gain smaller than the value 0.44 eV/ 1×1 cell due to the presence of the steps. A more intelligent adaption of steps parallel to $[\bar{1}12]$ and chains parallel to $[\bar{1}10]$ is needed. One idea is presented in Fig. 5.7(a). It is based

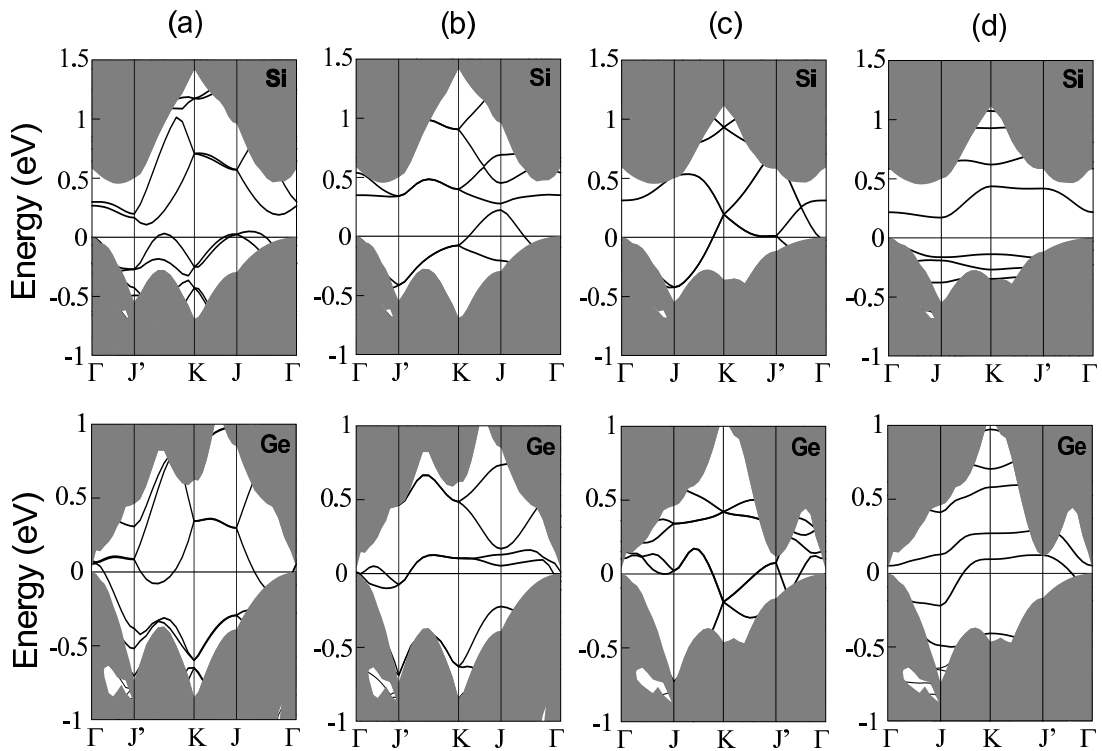


Figure 5.5 Band structures of Si and Ge(110) surfaces. (a) 1×2 with oppositely buckled chains, (b) 2×1 adatom model, (c) 3×1 adatom model, and (d) 3×2 adatom-tetramer-interstitial model. The Brillouin zone of the 2×2 (3×2) structure is used to present the bands obtained for 1×2 , 2×1 (3×1 , 3×2) translational symmetry. The high-symmetry lines are scaled in such a way that the ordinate axis has the same extension, independent of the considered translational symmetry.

on the preference of the 1×2 chain reconstruction. As a result of the chain buckling in opposite directions different distances of the chains parallel to $[001]$ occur on both terraces. These distances "up" and "down" between chains with raised and lowered atoms are indicated in Fig. 5.7(a). There are also lateral displacements of the chain atoms which nearly conserve the bond lengths (cf. Table 5.1). Buckled atoms allow two basically different bonding configurations between chain atoms of the upper and lower terraces across a step. After the formation of the trench each edge atom on the uppermost terrace possesses two dangling bonds. One of these DBs may be rebonded with a DB of an atom from the lower terrace if their distance is not too large. According to Fig. 5.7(a) the lowered atom of a chain of the upper terrace is more preferred to continue a chain on the lower terrace. By means of the total-energy minimization we found that within such a step configuration indeed rebonding of each edge atom on the upper and lower terraces takes place. One has to mention that a similar step structure has been proposed to explain the stripes by pairs of pentagons [182]. In this model the rest atoms at the chains are also correspondingly buckled [75].

The described step structure is energetically favorable. The surface energy of the system with oppositely buckled chains on the terraces and rebonded step atoms is lower in energy by 20 meV/ 1×1 unit cell (cf. Table 5.2) compared with the surface without steps. This corresponds to

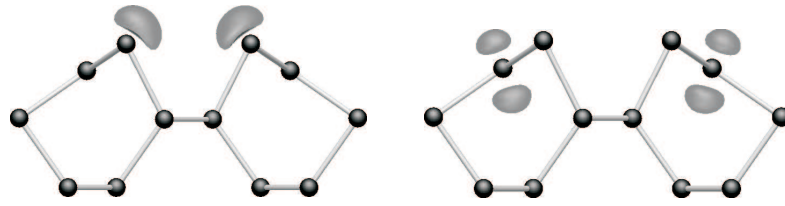


Figure 5.6 Wave-function squares at K for the chain model of the Si(110) 1×2 surface. Left panel: highest occupied state, right panel: lowest unoccupied state.

an effective energy gain of 0.16 eV due to one bond across the step. This fact indicates why steps with an appropriate bonding configuration and the accompanying trenches are favorable for the 16×2 reconstruction of the Si(110) surface. The formation of steps without rebonding slightly increases the surface energy. This loss is overcompensated by the rebonding. The formation of a trench is accompanied by four additional DBs on the upper terraces in a 16×2 unit cell. However, their rebonding with DBs of the lower terrace reduces the total number of dangling bonds by four with respect to the situation of the flat Si(110) surface with 64 DBs. One therefore expects to reduce the absolute surface energy 2.18 eV/ 1×1 cell of the 1×2 reconstructed surface by 6.25%, i.e., by about 0.14 eV/ 1×1 cell. The calculated effective reduction is however much smaller due to the creation of the steps themselves.

5.3 Adatoms

In order to explain the fine structure observed in the STM images of the Si and Ge(110) 16×2 surfaces one has to deal with larger reconstruction elements or building blocks consisting of several atoms. The restriction to chains with only up and down atoms is insufficient. Important parts of such reconstruction elements or building blocks could be adatoms which reduce widely the number of dangling bonds. To understand the basic mechanisms of the stabilization by adatoms we have again considered small unit cells. A variety of reconstruction (Table 5.2) models have been studied. The most favorable (for Ge) and energetically second (for Si) pure adatom reconstruction leads to the 2×1 surface shown in Fig. 5.4(b). One adatom on a 2×1 cell saturates three DBs of first-layer atoms. The remaining DB belongs to a rest atom. One expects an energy gain due to an adatom-rest atom mechanism, such as occurs on a Ge(111)c(2×8) surface (cf. Sect. 3.2). Indeed, the 2×1 adatom model in Fig. 5.4(b) further lowers the surface energy (see Table 5.1) for both Si and Ge(110) surfaces. However, the energy gain is much smaller than that computed by Takeuchi [86]. The adatom-rest atom mechanism determines the surface electronic structure. This is clearly indicated in Fig. 5.5(b). The calculated band structures exhibit the opening of a band gap, at least in the case of Si. A nearly direct band gap occurs at the J point. In the Ge case surface bands overlap with bulk states near Γ . The squares of the surface wave functions at K are presented in Fig. 5.8 for Si. The localization of the wave functions and the state occupation confirm the classical picture of an adatom-rest atom charge transfer. The occupied states with s -like character are observed at the rest atoms which

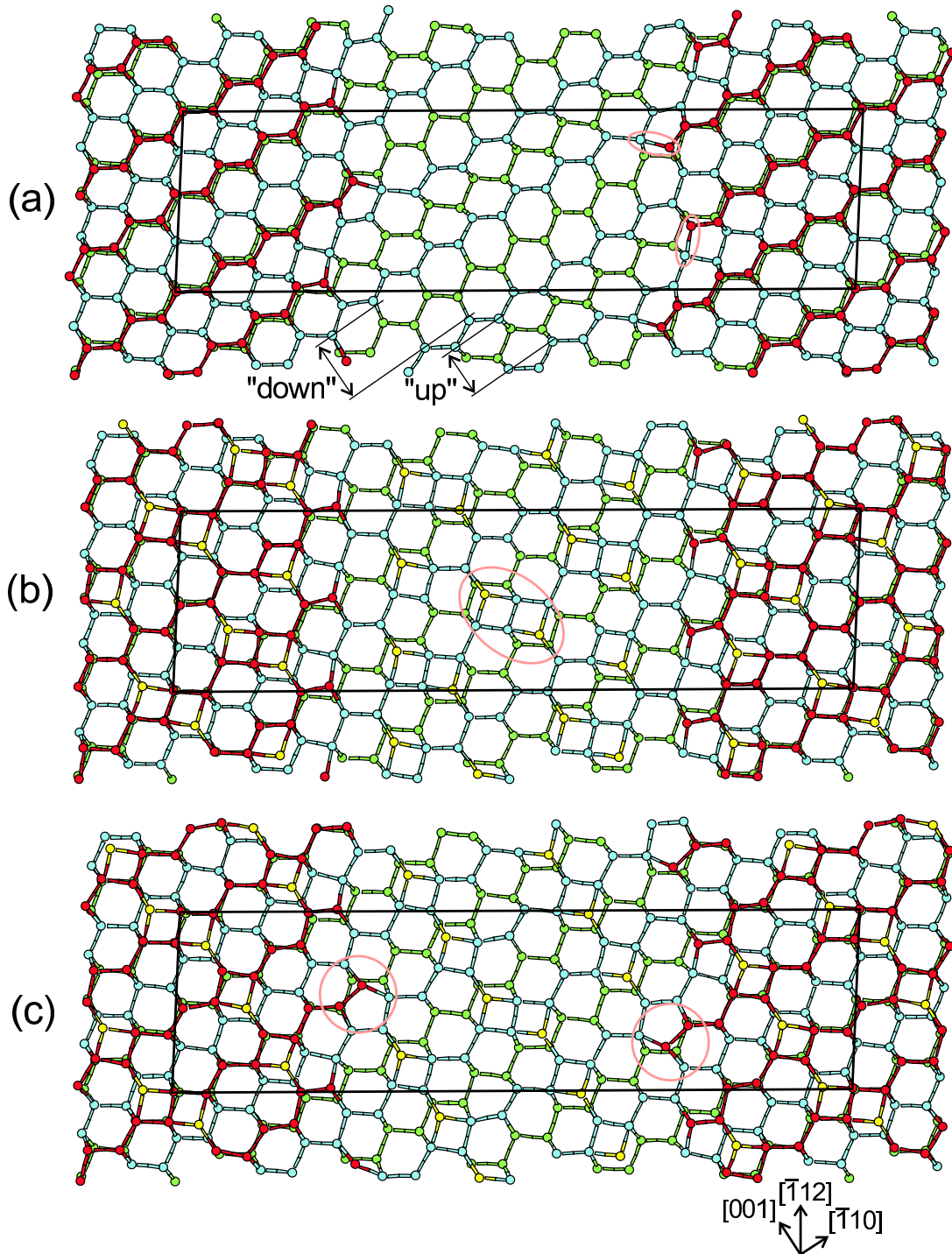


Figure 5.7 Top views of relaxed atomic positions of Si(110)16x2 surfaces: (a) oppositely buckled chain model with steps, (b) adatom-1 model and (c) adatom-2 model. Yellow circles are adatoms; red circles are atoms in the first layer (or upper stripe atoms); blue circles are atoms in the second layer and green circles are atoms in the the third layer. The lateral unit cell is indicated by thin solid lines.

are displaced from the surface towards the vacuum region. The dangling bond of the adatom is more p_z -like. Consequently, more or less one electron is transferred from the adatom to the rest atom. The same tendency is observed for Ge. The vertical differences between adatom and rest atom positions are rather small with 0.31 and 0.26 Å for Si and Ge, respectively.

One attempt to accommodate adatoms in appropriate distances and to saturate all dangling bonds is shown in Fig. 5.4(c). According to a common believe one adatom on a $c(2 \times 2)$ unit cell should allow an arrangement with a complete saturation of the dangling bonds. According to Ref. [86] the adatom is bonded to four different atoms in neighbored chains. Bonds with lengths of 2.4 and 2.6 Å should give rise to an extremely large energy gain of more than $1 \text{ eV}/1 \times$ cell. The results of the careful relaxation of the structure in Fig. 5.4(c) indicate a completely different behavior. The energy gain in Table 5.2 is much smaller; smaller than those of all bond-length-conserving chain reconstructions [e.g. that shown in Fig. 5.4(a) and the 2×1 adatom model]. The structural data are in agreement with the energetical findings. We derive a much larger distance between the adatom and the fourth (most distant) atom that contributes to the seemingly fourfold coordination of the adatom. The different results (with respect to Ref. [86]) can be related to a better convergence concerning the number of atomic layers in the slab, the BZ sampling, and the energy cutoff of the plane-wave expansion. The critical distance between adatom and fourth atom amounts to 2.87 (3.08) Å for Si (Ge), i.e., in between $\frac{a_0}{2}$ and $\sqrt{\frac{3}{2}} \frac{a_0}{2}$. This value is much larger than the characteristic bond length 2.34 (2.44) Å and can be only related to an extremely weak bond. The physical/chemical reasons for the findings are obvious. Si and Ge atoms prefer fourfold coordination with tetrahedral bonding. An arrangement of four nearest neighbors in nearly one plane is rather unfavorable. An adatom with a p_z -like dangling orbital can only have a weak overlap with the dangling bond at the fourth atom. Another configuration with a stronger wave-function overlap would however induce a remarkable strain in the atomic layers below. The situation is similar to the case of adatoms on Si and Ge(111) surfaces (cf. Sect. 3.2) or to the 2×1 adatom reconstruction discussed above. The resulting geometry allows another interpretation. The adatom and the fourth atom, the chain atom in [001] direction with a remaining dangling bond, represent an adatom-rest atom pair but not a pair with true bonding.

Using 3×1 and 3×2 unit cells we have optimized structures where all dangling bonds of the original (110) surfaces are saturated by adatoms. Such 3×1 and 3×2 reconstructions are shown in Figs. 5.4(d) and 5.4(e), respectively. Each adatom is threefold coordinated. There remains only one dangling bond per adatom. The adatom reconstruction models substantially reduce the dangling bond density, the number of dangling bonds per 1×1 unit cell. Instead of two in the 1×2 case with buckled chains or one for the 2×1 and $c(2 \times 2)$ adatom models the dangling bond density is further reduced to $2/3$. However, in contrast to the other adatom reconstructions no rest atoms occur. The 3×1 arrangement of the adatoms following each other in [001] direction [Fig. 5.4(d)] is more favorable from the energetical point of view for Si (cf. Table 5.2). In the Ge case it is less favorable than the 2×1 adatom reconstruction. These contradictory findings are similar to those for the (111) surfaces, where the adatom-rest atom pairs on $c(2 \times 8)$ cells are the most favorable reconstruction elements for Ge but not for Si (cf. Sect. 3.2). Surprisingly, the out-of-phase arrangement of the adatoms within the 3×2 translational symmetry [Fig. 5.4(e)] is much higher in energy (cf. Table 5.2). This fact confirms that Si and Ge(110) surfaces are

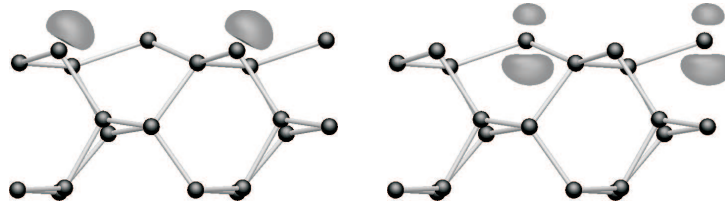


Figure 5.8 Wave-function squares at K for the adatom model of the Si(110) 2×1 surface. Left panel: highest occupied state, right panel: lowest unoccupied state.

“sensitive” with respect to the adatom distributions. To reduce probably the surface stress we also have tested a structure with two adatom-rest atom pairs but in 2×2 unit cells (not shown). It gains 20 meV per 1×1 cell for Si and 50 meV in the case of Ge in comparison with the 3×2 periodicity. However, in both cases the values lie quite far from those for the most favorable adatom reconstructions.

The general weak tendency for a stabilization of a pure adatom structure, in particular for Ge, is understandable in terms of the nearly identical bonding behavior of the adatoms and the resulting bands. It is accompanied with metallic band structures as indicated in Fig. 5.5(c) for both Si and Ge(110) 3×1 adatom structures. The low surface energy of the Si(110) 3×1 adatom reconstruction and its metallic band structure do not contradict the reconstruction rules for semiconductor surfaces [44]. Similar observations have been made for [111] surface orientations. The Si(111) 7×7 surface possesses a metallic band structure but is the energetically most favorable reconstruction. In the Ge(111) case the lowest-energy structure $c(2\times 8)$ is semiconducting (cf. Sect. 3.2). This is in agreement with the fact that the Ge(110) 2×1 adatom reconstruction is also the lowest one in energy (cf. Table 5.2).

A possible 16×2 reconstruction for Si(110) with a trench where adatoms reduce a maximum number of DBs on the terraces is shown in Fig. 5.7(b). The same rebonding mechanism of DBs situated at step atoms is assumed as discussed in the case of Fig. 5.7(a). In the first adatom model these edge atoms form lines exactly along the $[\bar{1}12]$ direction. Excluding the four step atoms with nominally two DBs, 28 DBs occur at the surface atoms on the upper terrace before adatom coverage. The same number of DBs remain on the lower terrace since four DBs are already saturated by rebonding with DBs of step atoms on the upper terrace. In Fig. 5.7(b) eight adatoms have been arranged on each terrace to leave only four rest atoms on each terrace which may contribute to the formation of stripes in the STM images. Together with the unsaturated four DBs at the uppermost edge atoms a total number of 28 DBs remain in a whole 16×2 unit cell instead of the 64 ones in the case of an ideally relaxed (110) surface.

Despite the substantial reduction of the dangling-bond density the model in Fig. 5.7(b) is less stable than a simple bond-rotation relaxation with chains on an unreconstructed Si(110) surface (see Table 3.8). The energy gain due to DB saturation is overcompensated by the stress induced in the surface. Such a tendency has been discussed above. The actual arrangement of adatoms sensitively influences the system energy. This also holds for the structural element with two adatoms marked by a circle in Fig. 5.7(b). It has been proposed previously as a

main structural element on a group-IV (110) surface [72, 83, 184]. Although it may potentially saturate the highest number of DBs within a 16×2 reconstruction, it is rather unfavorable from the energetical point of view.

In Figure 5.7(c) adatoms are arranged almost along the [001] direction according to findings for smaller unit cells. In comparison to the first adatom model [Fig. 5.7(b)] the number of adatoms is reduced with the consequence of a higher number of rest atoms on each terrace. Electron transfer between adatoms and rest atoms and, hence, the accompanying energy gain is more likely. The rebonded steps are modified by attachment of adatoms which keep their character. In particular, as marked by circles in Fig. 5.7(c) rebonded elements can be considered as natural continuations of the preferable adatom arrangements along the [001] direction on the lower terrace. On the other hand it can be also interpreted that a step atom is bonded to an adatom. With the six adatoms on each terrace one counts a total number of 36 DBs. Despite the larger DB density compared with adatom-1 model [Fig. 5.7(b)] the surface energy is drastically lowered (cf. Table 5.2). The energy gain is larger by 80 (10) meV/ 1×1 cell compared with the other adatom model (the terraces with oppositely buckled chains). Three reasons may be mentioned for the substantial energy gain: the favorable arrangement of the adatoms, the electron transfer between adatoms and rest atoms, and the modified step structure.

5.4 Adclusters

Recently, Ichikawa [81] explained the STM images observed for the Ge(110) 16×2 surface by pairs of five-membered adclusters. We have also optimized Si and Ge(110) 6×2 reconstructed geometries which consist of two five-membered adclusters. The structure is presented in Fig. 5.4(f). Each of the clusters has three adatoms and two bridge-site atoms. Two bridge-site atoms belonging to different adclusters form a bond between each other [81]. Along the chain direction in the underlying atomic layer clusters are separated by four atoms at nearly ideal positions. However, the above-described structure is not stable for both Si and Ge. We could not really find local minima on the total-energy surfaces. The atomic forces remain too large. In contrast to Ref. [81] in our calculations the convergence criterion concerning the forces is stronger by one order of magnitude. The reason of the structural instability [44] could be an oversaturation of surface bonds. Two adatoms along the chain in each cluster are located in such a way that they seemingly saturate the dangling bonds of one atom twice. Additionally the two bridge-site atoms weaken a σ chain bond and give rise to four new bonds. Consequently, depending on the starting configuration a bridge-site atom may saturate a dangling bond of the next chain atom or a neighboring adatom.

Simulated STM images of the Ge(110) 16×2 reconstruction with five-membered clusters look similar to the images observed experimentally [81]. This similarity was interpreted as a proof for the existence of the assumed reconstruction element. Our calculated STM images are presented in Fig. 5.9 for the Si(110) 6×2 reconstruction.¹ The images show spot arrangements

¹ The adatoms of the 6×2 reconstruction model take remarkably different vertical positions [cf. Fig. 5.4(f)] and, hence, make it difficult to choose an appropriate plane to compute the constant-height STM images. Moreover, the

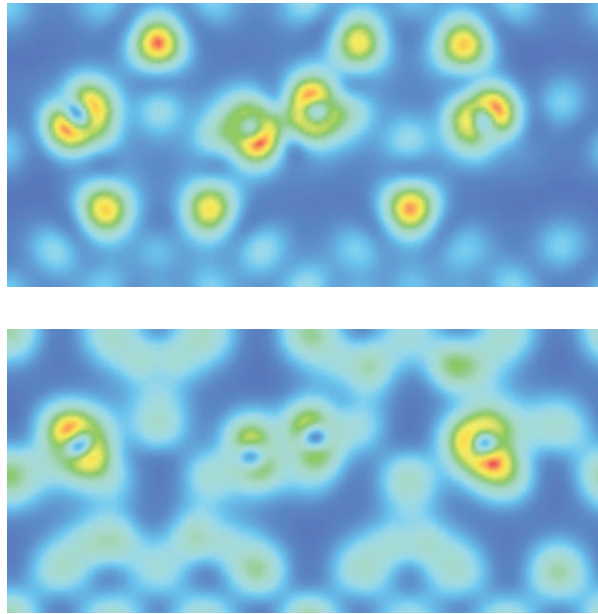


Figure 5.9 Simulated STM images of empty (top panel) and filled (bottom panel) states of the 6×2 five-membered clusters Si(110) surface for voltages corresponding to 2 and -2 eV with respect to the theoretical Fermi level.

similar to the observed pentagon-shaped ones. States originating from all adcluster atoms including the bridge-site atoms contribute to the empty-state image of the 6×2 reconstruction. In contrast, in Fig. 5.9 (bottom panel) occupied states give only contributions at bridge-site atoms and not at the other adatoms. We have also not found any contribution of occupied states which are located at adatoms using a three-dimensional representation of the wave functions. If the plane to plot the constant-height STM images is closer to the surface, it is, however, more probable to see states localized at the four rest atoms belonging to the chain. In general, it is not possible to observe significant pentagon structures in both empty and occupied images for the described Si(110) 6×2 reconstruction. This holds also for Ge.

5.5 Missing rows and adatoms

In order to model the 16×2 reconstruction an additional degree of freedom is due to the possibility of atom removal or even missing rows of atoms [82, 183]. One possible realization was suggested by the filled-state STM images of Si(110) 16×2 with only six protrusions per unit cell on each terrace. According to Packard and Dow [82] the basic building block consists of missing rows of atoms along $[\bar{1}10]$ and adatoms. The corresponding relaxed surface geometry is shown in Fig. 5.10(a). The atom removal along the $[\bar{1}10]$ direction is clearly visible. In comparison to the two adatom models in Figs. 5.7(b) and 5.7(c), there is also another type of

comparison of the images obtained in constant-height mode with measured constant-current mode images is rather problematic. We use a plane which crosses the bridge-site atoms.

adatoms which connect atoms in different atomic layers along [001]. Their situation seems to be reasonable because these atoms take positions similar to the T_4 and H_3 adatoms positions on the Si(111) surface (see Sect. 3.2 and Ref. [44]). Six adatoms form a stretched hexagon [marked by dotted lines in Fig. 5.10(a)] with one adatom in the center. Additionally two so-called dimers [82] marked by elongated circles in Fig. 5.10(a) occur between the second and third atomic layers. These elements have exactly the same bonding nature as the rebonded edge atoms discussed above.

The 16×2 reconstruction in Fig. 5.10(a) results in the highest surface energy for the geometries under consideration. The energy gain amounts to a value being only one half of the gain for a reconstruction with differently buckled chains shown in Fig. 5.10(a) (cf. Table 5.2). Two reasons should be mentioned. Locally the adatom distribution is rather similar as in the $c(2\times 2)$ adatom configuration, which was found to be rather unfavorable. Furthermore, the removal of atoms to generate the missing rows leave dangling bonds in not preferable configurations.

5.6 Tetramers and interstitials

For Si(110) 16×2 the trials to explain the details of the stripes found by STM on different terraces [72, 75, 82] are focused on structural elements which are able to describe both the empty-state and filled-state images. Another guiding principle should be oriented to the insulating behavior observed experimentally for the Si(110) 16×2 surface [184]. Pure adatom reconstructions discussed above with partially occupied bands give rise to a metallic character. Dangling bonds situated at pairs of adatoms and rest atoms may give nonmetallic electronic structures but double the number of structural elements and, moreover, increase the distance of equally filled DBs. At least, they have to be combined with other reconstruction elements such as dimers on Si(100) [44], tetramers on Si(113) (chapter 4) and (114) [165] or pentamers on Si(113) (chapter 4). Indeed, tetramers are able to give rise to different STM images probing empty or filled states. Using such an element this has been demonstrated for the Si(113) 3×2 surface within the ADI model and the Si(114) 2×1 surface reconstruction with dimers, tetramers, and rebonded atoms [165]. For the Si(113) 2×1 surface it has been proven that the pure tetramer structures yield to a surface-state gap independently of buckling/puckering of the tetramers. Buckled pentamers have been predicted to be seen in STM images at negative and positive bias voltages of the Si(113) 3×2 surface with an adatom-interstitial reconstruction.

One may expect the occurrence of qualitatively similar reconstruction elements on the Si(110) 16×2 surface. Based on the idea to explain the STM findings for Si(110) 16×2 surfaces by pentagons which are formed by tetramer and interstitial atoms [75], we have studied such reconstruction elements in 3×2 unit cells. We followed the ideas developed to interpret the 3×2 reconstruction of Si and Ge(113) surfaces by ADI and AI models (cf. chapter 4). The pentagon (or pentamer) in one half of a 3×2 cell consists of four adatoms (tetramer) and one atom belonging to a chain in the first atomic layer. They saturate five of the six surface dangling bonds. The interstitial atom is laterally located at the center of the pentamer but below the pentamer plane. In the second half of the 3×2 cell two additional adatoms saturate the dangling bonds in

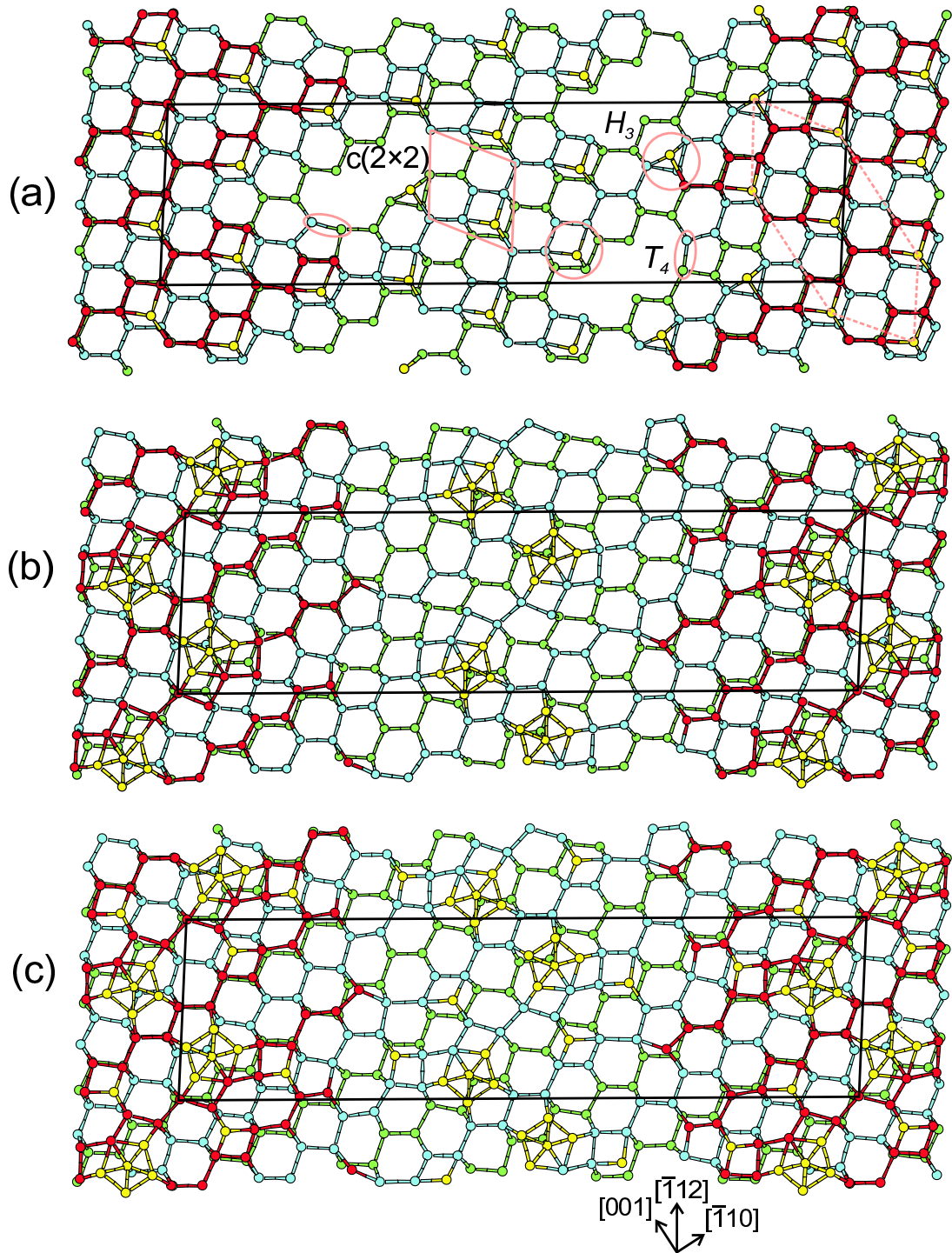


Figure 5.10 Top views of relaxed atomic positions of Si(110) 16×2 surfaces: (a) stretched-hexagon model, (b) tetramer-interstitial model, and (c) adatom-tetramer-interstitial model. Yellow circles are adatoms; red circles are atoms in the first layer (or upper stripe atoms); blue circles are atoms in the second layer and green circles are atoms in the third layer. The lateral unit cell is indicated by thin solid lines.

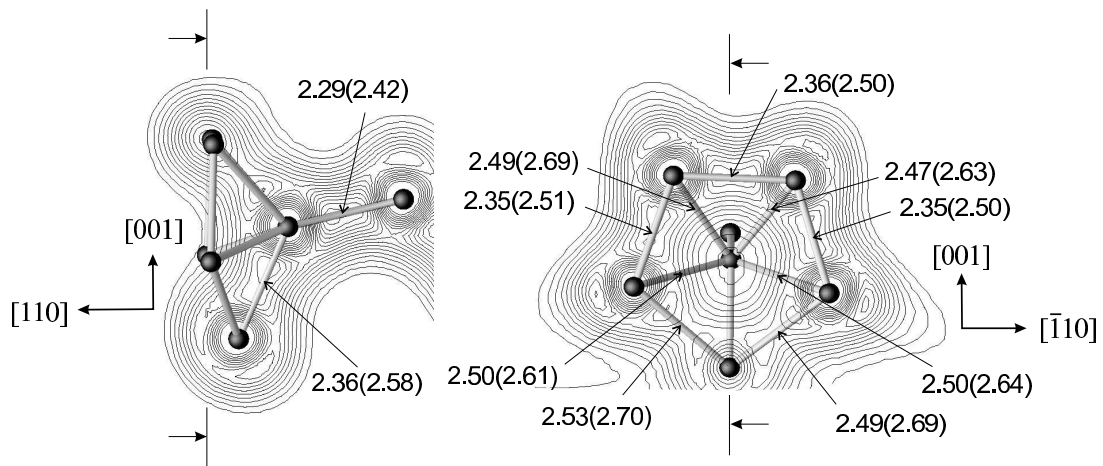


Figure 5.11 Charge density plot around the interstitial and pentamer atoms for the 3×2 adatom-tetramer-interstitial reconstruction of Si(110). Planes used for representation are indicated by arrows. Bond lengths are also given for Ge (in brackets).

such a way that one rest atom is left. The resulting 3×2 adatom-tetramer-interstitial (ATI) reconstruction is drawn in Fig. 5.4(g). Origins of tetramers in the case of Si and Ge(110) surfaces are different from those on Si(113) and Si(114) surfaces which are formed by rebonding of already existing atoms. Up to now we could only find metastable structures with pure tetramers. In contrast to that the total-energy minimizations show that the ATI reconstruction is the same in energy with respect to the most favorable 3×1 adatom Si structure. For Ge the energy gain is also comparable to that calculated for the 2×1 adatom reconstruction. However, the reconstruction with a pentamer and an interstitial atom gains energy only in combination with two adatoms, at least within the 3×2 translational symmetry. For Si the energy difference between the models with and without additional adatoms amounts to 0.21 eV per 1×1 unit cell. The reason will be discussed below describing the band structure.

The interstitial atom is sixfold coordinated. In Fig. 5.11 the strength of the bonds between this atom and its neighbors is discussed in terms of the bond lengths and the electron distribution. The side view in Fig. 5.11 clearly indicates that the interstitial atom creates a strong bond with the atom below in the second-atomic layer. The shortest bond of 2.36 (2.58) Å with the fifth pentamer atom is strong (weak) for Si (Ge). The bonds to the other four pentamer atoms are usually weaker with lengths of about 2.5 (2.6–2.7) Å. At least for Si, three (of five) strong bonds between pentamer atoms are indicated by keeping nearly the bulk bond length. This is also clearly indicated by the electron distribution between the pentamer atoms. The two bonds with the fifth pentamer atom (i.e., a chain atom in the first atomic layer) are weaker. This is a consequence of the fact that this atom has five nearest neighbors [cf. Fig. 5.4(g)]. The four adatoms of the pentagon are fourfold coordinated. However, they do not anymore show an sp^3 hybridization.

An indication for the large energy gains arises from the band structures in Fig. 5.5(d). There is a tendency for the opening of an energy gap between the surface-state bands. The gap of

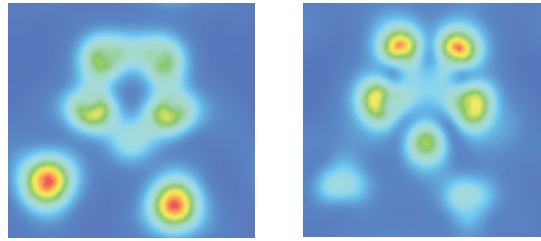


Figure 5.12 Simulated STM images of filled (left panel) and empty (right panel) states of the Si(110) 3×2 adatom-tetramer-interstitial surface for voltages corresponding to -2 and 2 eV with respect to the theoretical Fermi level.

the 3×2 ATI reconstruction is the largest one among all studied Si(110) reconstructions. The opening mechanism is similar to that discussed for the Si(113) 3×2 ADI surface. Due to the weak bonding pentamer atoms donate electrons to the two adatoms in the second half of the 3×2 unit cell. Their dangling bonds are fully occupied with electrons which form lone pairs. As a consequence the filled-state (empty-state) STM images are dominated by adatom (pentamer-atom) electronic states. This is demonstrated in Fig. 5.12. For the Si(110) 3×2 ATI surface the STM images simulated for a bias of -2 V (2 V) mainly show the adatoms (pentamer atoms) in the lower (upper) half of the 3×2 surface unit cell. The STM image simulated for the empty states seems to be similar to the characteristic pentagon-shaped element of the empty-state STM images observed for the Si(110) 16×2 surface.

There is a chance that tetramer-interstitial pairs explain the “pairs of pentagons” as suggested by An et al. [75]. Such a 16×2 tetramer-interstitial (TI) model is represented in Fig. 5.10(b). We adapted the step configuration discussed in Fig. 5.7(a). The connecting line of the chain atom and the interstitial in the resulting centered pentamer is almost parallel to the $[001]$ direction. The uncovered regions of the terraces exhibit the usual bond-rotation relaxation of the surface chains.

The TI reconstruction gives rise to a minimum on the total-energy surface but the resulting surface energy is too high (cf. Table 5.2). The energy gain only amounts to 0.39 eV/ 1×1 cell. The small gain is in agreement with the findings for a 3×2 translational symmetry. For that reason the adsorption of two additional atoms for each pentamer is considered. The resulting 16×2 ATI geometry is represented in Fig. 5.10(c). Indeed, the surface energy is lowered substantially by 100 meV/ 1×1 cell with respect to the TI case without additional adatoms. This strong energy gain is mainly due to the strong s character of the DBs situated at the adatoms which induces an electron transfer from the pentamers resulting in lone pairs of electrons. Instead of the eight adatoms per 16×2 unit cell we have also studied geometries with 12 or four adatoms. The accompanying energy gains were only 10 – 15 meV/ 1×1 cell lower than for the eight-adatom case. Therefore, we conclude that the number of adatoms per pentamer may vary on real surfaces at room temperature (with $k_B T = 25$ eV) and above.

In any case the ATI reconstruction in Fig. 5.10(c) yields the lowest surface energy for models of the Si(110) 16×2 surface with trenches and terraces. However, the corresponding energy

gain of 0.49 eV/ 1×1 cell is still smaller than the gain of 0.54 eV/ 1×1 cell obtained for the ATI reconstruction of the Si(110) 3×2 surface. Since this energy difference is not a consequence of the numerical inaccuracy of the total energy calculations, it has to be discussed physically. Either the 16×2 reconstruction does not represent the equilibrium surface phase or a completely different reconstruction model is needed. Kinetic barriers and hence the surface preparation usually allow the observation of the 16×2 phase only for less doped substrates. Such a preparation dependence is known for the Si(111) surface with the 2×1 reconstruction after low-temperature cleavage and the 7×7 translational symmetry after annealing [44]. Perhaps, a completely new, more complex reconstruction model is needed such as the DAS model with corner holes found for the Si(111) 7×7 surface [62]. At least the total energy investigations of the 16×2 reconstruction models suggested by several authors [75, 82] and the 16×2 geometries lead to surface energies higher than that calculated for the 3×2 translational symmetry.

Besides the surface energy other important arguments for the validity of a certain reconstruction model can be derived from STM images simulated for different bias voltages. Such images are presented in Fig. 5.13 for the 16×2 ATI reconstruction. Because of the constant-height mode used in the simulation only spots from upper terraces are visible. The figure shows that the observed image stripes can really be simulated by an ATI reconstruction. The stripes parallel to $[\bar{1}12]$ consist of pairs of extended reconstruction elements arranged in zigzag form. They are based on pentamers and accompanied by an additional pair of adatoms. The interstitial atoms captured by the pentamers are not seen. Indeed, Fig. 5.13 shows that one and the same reconstruction element gives rise to different spot distributions in the empty-state or filled-state images in agreement with the experimental observation [75].

Each element in the empty-state images consists of nearly five spots and represents directly the pentagon. The filled-state images in Fig. 5.13 show two strong spots due to the filled DBs at the adatoms and four weak spots from the tetramer which may be unified in the simulation varying the distance to the surface. Important features found experimentally can be reproduced but not all. Comparing with the analysis of An et al. [75] (see Fig. 5.14) the fine structure of the pairs seems to be interchanged in the measured and calculated spot distributions. On the other hand, the filled-state images measured by Packard and Dow [82] have been interpreted by an arrangement of spots in a deformed hexagon with a center. In contrast to the images discussed above only six spots belong to one terrace in a 16×2 unit cell. There is also disagreement between experimental results. One explanation for the different findings may be related to the energetics of the adatom-tetramer-interstitial reconstruction mentioned above. The variation of the number of adatoms (which should give rise at least to spots in the filled-state images) does hardly influence the surface energy.

Other points to be discussed concern the visibility of the interstitial atoms and the asymmetry (buckling, puckering) in the pentamer or tetramer structures. Hints follow from the behavior of the Si(113) 3×2 surface. For this surface the ADI model represents a low-energy structure. After addition of one interstitial to each tetramer the AI 3×2 model appears having two pentamers and two adatoms similar to the ATI reconstruction considered in Fig. 5.13(c). Asymmetries between the two pentamers in the Si(113)-AI model allow an additional electron transfer that lowers the energy. It has been shown that the presence of interstitials and asymmetries

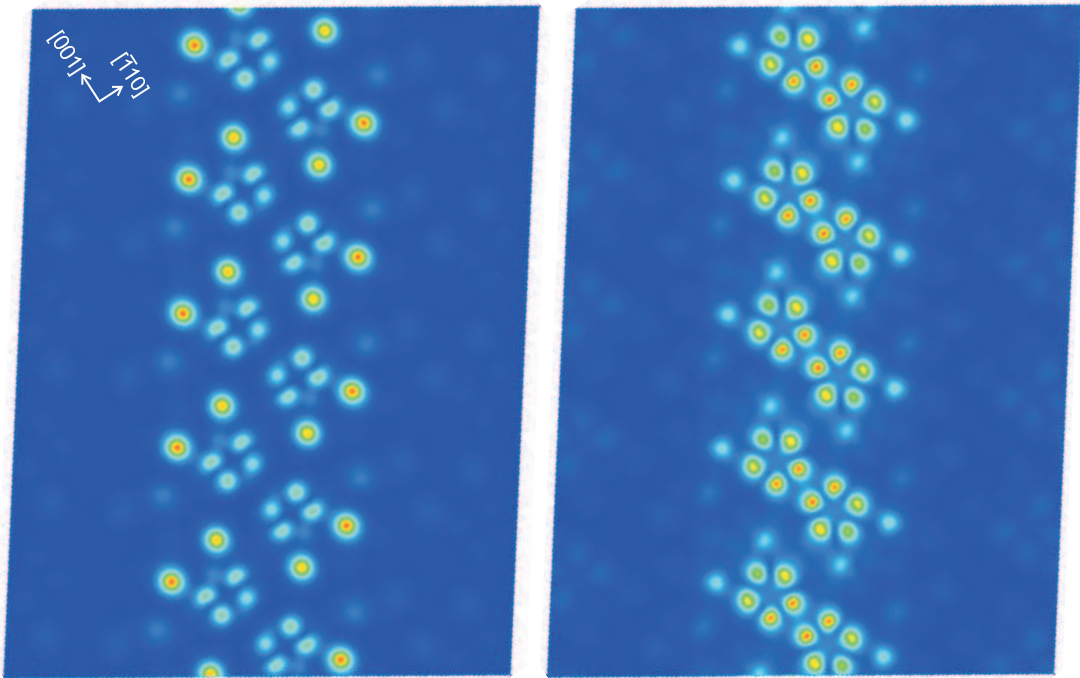


Figure 5.13 Simulated STM images of filled (left panel) and empty (right panel) states of the Si(110)16×2 adatom-tetramer-interstitial reconstruction for bias voltages corresponding to 1 and −1 eV with respect to the theoretical Fermi level. Five unit cells translated along the $[\bar{1}12]$ direction are represented.

significantly changes the STM images for Si(113) surfaces with respect to the number of spots. Another possibility for the variation of spots may be related to the visibility of adatoms, more strictly of their DBs. Such atoms might be hidden in missing rows or holes which cannot be “seen” by an STM tip. For instance, this happens for the DBs of restatoms in corner holes of the Si(111)7×7 surface which are completely filled (cf. Sect. 3.2) but do not contribute to STM as protrusions [68]. In the Si(110)16×2 case such an effect might happen also for the attachment of such an atom at a step.

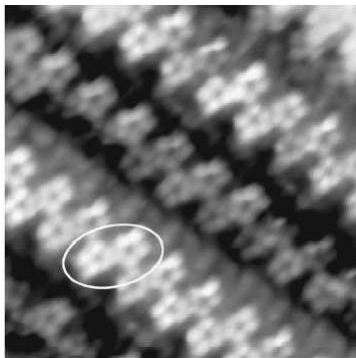


Figure 5.14 High-resolution STM topographic image of the 16×2 structure in the empty states [$V= 1.20$ V, $I=0.20$ nA, 10×10 nm] (from Ref. [75]).

Chapter 6

Shape of free and constrained crystallites: Influence of surface energies

6.1 Absolute Surface Energies

6.1.1 Dependence on orientation and reconstruction

Here we summarize values of absolute surface energies given in previous chapters for the most favorable reconstruction and make comparative studies for different orientations and materials. Resulting values are listed in Table 6.1. If one again imagines cutting a group-IV crystal at some plane, one may expect the energy required to be proportional to the number of bonds cut. In units of a_0^{-2} (a_0 - bulk lattice constant) the dangling-bond density across a $\{111\}$ surface plane is $4/\sqrt{3}$. This is smaller than the density of $2\sqrt{2}$ on a $\{110\}$ surface, $12/\sqrt{11}$ on a $\{311\}$ surface and 4 on a $\{100\}$ surface. With exception of diamond the trends in the energies of the unrelaxed/unreconstructed Si and Ge surfaces follow the dangling-bond densities. However, after inclusion of surface reconstruction the $\{111\}$ surfaces of diamond possess the lowest energy, and therefore one may expect the natural cleavage plane or growth surface to be a $\{111\}$ plane. There are eight such orientations, forming the eight faces of the natural octahedral crystal for the homopolar tetrahedral solids. The ordering of the other surface energies is more complicated to understand. With surface reconstruction the $\{311\}$ faces seem to be favored against the $\{110\}$ planes (cf. e.g. in the case of diamond). This is in agreement with the dangling-bond densities if only the dangling bonds in the uppermost atomic layer of the $\{311\}$ surface are counted. The high surface energies $\gamma(110)$ for silicon and germanium in Table 6.1 reflect the small energy gain of only about $0.5 \text{ eV}/1 \times 1$ unit cell even studying the long-range 16×2 reconstructions. The absolute surface energies of the reconstructed $\{111\}$, $\{311\}$, and $\{100\}$ surfaces of germanium are practically equal. The smaller values for $\{311\}$ and $\{100\}$ of about 0.01 J/m^2 (i.e., about 1%) with respect to the $\{111\}$ cases may be considered as the inaccuracy (more precisely, numerical uncertainties treating slabs with different orientations) of the used *ab initio* calculations (see chapter 2).

The order of magnitude of the values measured for Si [27] (see Table 6.1) agrees very well with the energies calculated for the reconstructed surfaces. This also holds more or less for

Table 6.1 Surface energies γ (in J/m^2) for diamond, Si and Ge (see also Tables 3.1, 3.4, 4.1 and 5.2). The first value represents the unrelaxed $\{hkl\}$ surface, while the second (lower) value corresponds to the reconstructed/relaxed geometry with the lowest energy. In the case of Si the results are compared with those of measurements [27] (the absolute scale is set using the value $\gamma(111)$ from fracture experiments [185]) tight-binding calculations [38], and molecular dynamics with empirical potentials. [39] A reconstruction is not taken into account. Only the measured $\gamma(111)$ value should be related to the 2×1 reconstruction [185].

Crystal	{111}	{110}	{100}	{311}	Reference
Diamond	8.12	7.48	9.72	8.34	
	4.06	5.93	5.71	5.11	present work
Silicon	1.82	2.04	2.39	2.21	
	1.36	1.63	1.41	1.40	present work
	1.23	1.43	1.36	1.38	[27]
	1.41	1.57	1.34	1.98	[38]
	1.41	1.72	1.49	–	[39]
Germanium	1.32	1.51	1.71	1.61	
	1.01	1.14	1.00	0.99	present work

the energetical ordering $\gamma(111) < \gamma(311) < \gamma(100) < \gamma(110)$. Within the experimental results only the sequence of the $\{311\}$ and $\{100\}$ planes is interchanged. However, their energy difference is small in theory and experiment. The ordering obtained in other calculations [38, 39] is the same. The other available experiment [26] found a surprisingly small anisotropy of the surface excess free energy per unit area with a strange hierarchy $\gamma(100) < \gamma(311) < \gamma(110) \leq \gamma(111)$ which is not in agreement with the fact that cleavage happens for $\{111\}$ surfaces. The anisotropy of the surface energies in Table 6.1 is remarkably increased for diamond, while it almost vanishes for germanium.

Table 6.1 also shows that the surface reconstruction and hence the actual surface geometry and preparation should play an important role for the shapes of crystallites or nanopillars. The maximum change with respect to the energy of the surface with a bulk atomic arrangement amounts to 100% for the C(111) surface after a 2×1 reconstruction within the π -bonded chain model. For Si(111) with the most favorable 7×7 reconstruction and Ge(111) with the $c(2 \times 8)$ reconstruction the effect is much weaker. Similar observations are made for the 2×1 (C) or $c(2 \times 4)$ (Si, Ge) reconstructions of a $\{100\}$ surface. The energy of Si and Ge(311) surfaces is substantially lowered by 3×2 ADI reconstructions. Indeed, there are experimental indications for reconstructed $\{311\}$ surfaces on nanostructures. Pyramidal Si islands appearing at finite growth temperature on Si(001) substrates have $\{311\}$ facets with a seemingly 3×1 reconstruction [31]. In the case of C(311) again a deviating behavior is found with a symmetric 2×1 tetramer reconstruction. In the $\{110\}$ cases the surface relaxation within a bond-contraction or a

bond-rotation model lowers the surface energy. Complicated long-range 16×2 reconstructions give only rise to a small additional energy gain (listed for Si) even considering ATI structural elements. In Table 6.1 we present the lowest surface energy values found for 3×2 ATI and 2×1 adatom models for Si and Ge, respectively.

6.1.2 Extrapolation

In order to investigate $\langle 100 \rangle$ -oriented nanocrystals with pyramidal shape, one also needs the surface energies of $\{501\}$ or $\{301\}$ planes. Unfortunately, parameter-free calculations are not available for the absolute surface energies for the surfaces with those orientations. Such calculations [16, 186] are restricted to the reconstruction geometries and the electronic structures. To estimate the $\gamma(501)$ and $\gamma(301)$ values we use the assumption that the surface free energy γ varies only weakly with the surface crystallographic orientation.

We formally consider a two-dimensional crystal in a plane perpendicular to the $[010]$ direction with a vicinal surface plane, i.e., a surface plane which consists of a relatively high number of areas with $[100]$ orientation being separated by steps of a certain height s_n [10]. Such a surface has an orientation angle θ against the $[100]$ direction. Each step is assumed to make a contribution δ to the total surface energy on the vicinal plane. With a step density $\tan \theta / s_n$ one can express the surface energy as

$$\gamma(\theta) = \gamma(100) \cos \theta + \frac{\delta}{s_n} \sin \theta. \quad (6.1)$$

The orientation vector $[101]$ of the closest high-index surface (101) is found for $\theta = 45^\circ$. Assuming a continuous variation of the surface energy between the minima at $[100]$ to $[101]$ [26, 27], one finds $\delta/s_n = \sqrt{2}\gamma(110) - \gamma(100)$. In the case of the $[n01]$ orientation ($n = 5, 3, 1$) it holds $\theta = 11.31^\circ, 18.43^\circ, 45^\circ$. Then expression (6.1) gives $\gamma(n01) = (1/\sqrt{n^2 + 1})[(n - 1)\gamma(100) + \sqrt{2}\gamma(110)]$. One finds the energy values $\gamma(501) = 6.12$ (C), 1.56 (Si), and 1.10 (Ge) J/m^2 and $\gamma(301) = 6.26$ (C), 1.62 (Si), and 1.14 (Ge) J/m^2 using the values for reconstructed low-index surfaces from Table 6.1.

6.2 Equilibrium Crystal Shape

6.2.1 Shape of diamond crystallites

Results of the Wulff construction of the ECS for diamond are plotted in Fig. 6.1. Essentially the surface energies calculated for the reconstructed low-index surfaces from Table 6.1 have been used. Taking into account only the surface with the lowest energy $\gamma(111) = 4.06 \text{ J/m}^2$, the cleavage face, one expects that the equilibrium geometry is a regular octahedron with eight $\{111\}$ facets. However, already the inclusion of one further surface orientation such as $\{100\}$ [as shown in Fig. 6.1(a)] makes the octahedron irregular. The corners of the octahedron are truncated by $\{100\}$ planes. A cubo-octahedron morphology appears with eight nonideal $\{111\}$ hexagons and six $\{100\}$ -oriented squares. Their areas depend on the surface energies, as long

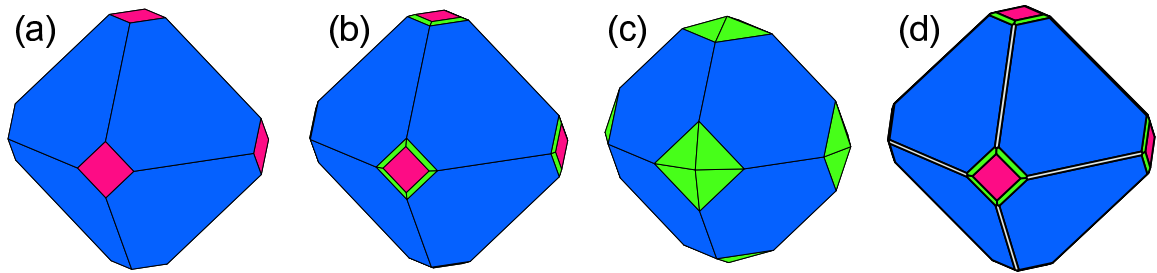


Figure 6.1 Equilibrium shapes of diamond crystals based on the Wulff construction using basically γ values from Table 6.1. In general, four surface orientations are considered, but in (a) only $\{111\}$ and $\{100\}$ facets. (b): Instead of the energy for the 2×1 reconstruction $\gamma(311) = 5.11 \text{ J/m}^2$ that for the 3×1 reconstruction $\gamma(311) = 5.50 \text{ J/m}^2$ is taken into account. (c): Values from Table 6.1. (d): Values as for (b) but the energy of $\{110\}$ facets is reduced to $\gamma(110) = 4.91 \text{ J/m}^2$. The areas with the orientation sequence $\langle 100 \rangle$, $\langle 311 \rangle$, $\langle 110 \rangle$, and $\{111\}$ are red, green, grey, and blue.

as $\sqrt{3}\gamma(111) < \gamma(100)$ [124]. If $\gamma(111)$ is considerably less than $\gamma(100)$ no truncation is expected. In the opposite limit a constant ratio of the plane areas occurs.

Taking into account more surface planes with other orientations, the resulting shape depends very much on the absolute values of the surface energies. This is also clearly demonstrated in Fig. 6.1. Using the energy $\gamma(311) = 5.50 \text{ J/m}^2$ for the symmetric 3×1 AD reconstruction instead of the lower value given in Table 6.1 [Fig. 6.1(b)], the cubo-octahedral shape of the nanocrystallites is basically conserved; but the $\{100\}$ squares are surrounded by stripes corresponding to $\{311\}$ facets. Diamond particles with exactly such a morphology have been observed after deposition by microwave-plasma CVD [35]. Decreasing the surface energy of the $\{311\}$ facets to the value $\gamma(311) = 5.11 \text{ J/m}^2$ (Table 6.1) for the 2×1 reconstruction, the corner truncation does not anymore happen, and no $\{100\}$ facets occur [see Fig. 6.1(c)]. Instead, the octahedron corners are rounded by small square-based pyramids with four $\{311\}$ facets. Another example for the strong influence of the absolute γ values is shown in Fig. 6.1(d). The values constructing Fig. 6.1(b) have been used but the surface energy of the $\{110\}$ planes is reduced to $\gamma(110) = 4.91 \text{ J/m}^2$. In contrast to Fig. 6.1(b) the sharp edges between $\{111\}$ facets disappear, and $\{110\}$ planes form stripes along the former edges. Such a shape with $\{111\}$, $\{100\}$, $\{311\}$, and $\{110\}$ facets has been observed for high pressure–high temperature synthetic diamonds [34]. Their surfaces have major growth sectors of the $\{111\}$ and $\{100\}$ types and some minor sectors of $\{311\}$ and $\{110\}$ types.

Despite the agreement stated for the ECSs in Fig. 6.1 with morphologies observed for grown diamond crystallites, general conclusions are very difficult. There is perhaps not a direct relationship between absolute surface energies of reconstructed clean surfaces and crystallography that the above description suggests. The real surfaces may be contaminated by adsorbed species or influenced by defects. Adsorbates and defects may change the surface reconstruction and, hence, the corresponding surface energy. In addition, the observed crystallite shapes may tend to be dominated by the growth process of the crystal rather than the energetics itself. One fact is

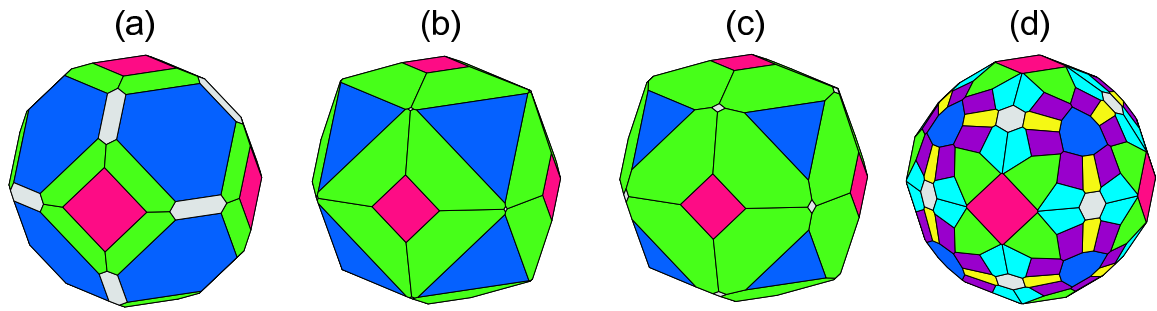


Figure 6.2 Equilibrium shapes of Si (a, b) and Ge (c, d) crystals based on the Wulff construction using (a) experimental values, (b, c) calculated values or (d) equal values γ for many surface orientations in the stereographic triangle [188]. In (a, b, c) four surface orientations are considered. The areas with the orientation sequence $\langle 100 \rangle$, $\langle 311 \rangle$, $\langle 110 \rangle$, and $\langle 111 \rangle$ are red, green, grey, and blue. In (d) more high-index surfaces are taken into consideration. The facets in yellow, violet, and light blue represent $\{331\}$, $\{21\ 9\ 29\}$, and $\{15\ 3\ 23\}$ facets, respectively.

related to the orientation dependence of the growth rate. For instance, there are indications that the CVD growth rate on $\{100\}$ surfaces is faster than that of the $\{111\}$ side-growth rate [187]. The preferential growth along a $\langle 100 \rangle$ direction clearly influences the resulting morphology of a crystallite.

6.2.2 Shape of Si and Ge crystallites

Figure 6.2 shows results of the Wulff construction of the ECS for silicon and germanium. In Figs. 6.2(b) and 2(c) we used calculated parameters of the surface energies $\gamma(hkl)$ for the reconstructed $\{111\}$, $\{110\}$, $\{100\}$, and $\{311\}$ surfaces of silicon and germanium given in Table 6.1. For the purpose of comparison the ECS for Si is presented in Fig. 6.2(a) for measured surface energies [27]. According to energies given in Table 6.1, Fig. 6.2(a) shows that the most stable surfaces have an $\langle 111 \rangle$ orientation with the next lowest ones being $\{100\}$, $\{311\}$, and $\{110\}$ surfaces with similar energies. Large $\{111\}$ facets and smaller $\{100\}$ facets occur on the surface of a crystallite. Between these facets smaller $\{311\}$ and $\{110\}$ facets are observable. No sharp edges between a $\{111\}$ and a $\{100\}$ facet or between two $\{111\}$ facets appear. According to the experimental γ values the equilibrium shape is thus to a good approximation a tetra-kaidecahedron [27]. Taking the calculated γ values into account the $\{110\}$ facets almost vanish as a consequence of the large $\gamma(110)$ value as shown by their small contributions in the corners between four $\{311\}$ facets in Fig. 6.2(b). In addition the areas of the $\{311\}$ facets are increased because of the low value of $\gamma(311)$.

One of the results of the ECS construction is the possible stability evaluation of a surface with a certain orientation. We have checked a possible occurrence of the Si(411) surface on the ECS. A Si(411) 2×1 reconstruction has been observed experimentally. The value of its surface energy calculated within an *ab initio* method lies between those for (111) 2×1 and (100) 2×1 surfaces [165]. Consequently, it has been concluded that Si(114) is a stable planar surface [165].

To be consistent within the computational method used here we assume γ of Si(411) 2×1 to be equal to 1.44 J/m^2 as found for the lowest left buckled π -bonded chain Si(111) 2×1 reconstruction from our calculations. Surprisingly, despite such a low γ the {411} facets do not occur on the ECS indicating that a (114) surface is not stable in the equilibrium in contrast to the (100) or (311) ones. However, narrow stripes would appear between the {100} and {311} facets if an additional reduction of about 0.015 J/m^2 is assumed, what also indicates that the absence of {411} facets might be related to inaccuracy of our approximations. The sensitivity of the ECS with respect to the absolute values of the surface energies again shows that modifications of the facet geometry, e.g. due to reconstruction, may drastically change the surface morphology of a crystal.

The last tendency is enforced for germanium as demonstrated in Fig. 6.2(c). Since the energies for the surface orientations $\langle 111 \rangle$, $\langle 311 \rangle$, and $\langle 100 \rangle$ are nearly the same, large {111}, {311} and {100} facets are visible. However, {311} facets give the largest area. Only small diamond-shaped {110} planes occur between {311} facets (note, larger than in the the case of Si). Nearly equal energies of the most stable surface orientations give a probability that several other high-index orientations have a similar γ and are therefore stable in the Ge case. To check this we include possible candidates with equal γ . In addition to the above-mentioned four surface orientations we also study the high-index surfaces {313}, {15 3 23} and {21 9 29} which have been reported to be stable and, hence, do not facet into other stable surfaces [188]. The resulting ECS is represented in Fig. 6.2(d). All considered surface orientations appear on it. In general, a Ge crystal tries to reach a “sphere” shape. The largest facets are {111}, {311} and {100} ones, while the {110} facets occur with a smaller area. Each of the sets of real high-index {15 3 23} or {21 9 29} surfaces contributes to the 48 facets. The corresponding values of the total area per each family are close to that for {311} facets which take the largest area.

6.3 Shape of Pyramidal Nanocrystals

6.3.1 Total energy and surface energy

The shape of a large, isolated, three-dimensional island grown on a certain substrate is determined by its total energy [9, 189]

$$E_{\text{total}} = E_{\text{elastic}} + E_{\text{surface}} + E_{\text{edge}}. \quad (6.2)$$

For coherently strained or partially relaxed islands the leading terms are the elastic relaxation energy E_{elastic} and the surface energy E_{surface} of the strained object connected with a substrate. E_{elastic} is the gain in deformation energy when the material forms a strained island instead of a biaxially strained film. E_{surface} is the cost in surface energy due to the creation of facets on the sides of the island corrected by the fact that the island base forms an interface to the substrate or the corresponding wetting layer. E_{edge} is the energy cost for the creation of sharp edges. Because of the interplay of local strain distribution and shape the scaling behavior of E_{elastic} with the volume V may also include nonlinear terms in addition to the main linear term.

E_{surface} and E_{edge} scale with the volume as $V^{2/3}$ and $V^{1/3}$, respectively. For an isolated island to form at all in preference to a film with the same volume, E_{total} must be negative.

Still, it is questionable if such a model (6.2) based partially on the macroscopic continuum theory may really apply to nanometer-sized systems. Nevertheless, here we go a step further in the simplifications and discuss trends restricting essentially to the surface energies listed in Table 6.1. Usually, E_{edge} is estimated to be negligible, provided the island size is not too small. In the case of III-V compounds this fact has been shown for nanometer-sized quantum dots [189]. The renormalization of the surface free energies per unit area, γ , due to surface stress is also more or less negligible. Changes up to 11% leave the prediction for the equilibrium shape qualitatively unchanged [189]. The elastic energy E_{elastic} is very important for the absolute value of the total energy of an island. However, for a given qualitative island shape (considering only low-index surfaces) its variation with the geometry parameters is also small, for InAs islands on GaAs(001) less than 10% [190]. For large islands which are not dislocation-free, the energy contribution E_{elastic} should be mainly determined by the elastic energy of a fictitious two-dimensional film with the same volume. As a consequence, in the following we qualitatively discuss the pyramidal shape of islands only on the basis of the surface energies. We are still using the request of a minimum surface energy F_s Eq. (2.37). In addition to the constraint of a fixed volume V Eq. (2.38) we also consider two other constraints, the orientation of the pyramid and the shape of the pyramid base plane. That means, the only considered influence of the substrate used in the epitaxial growth is the normal of the base (parallel to the surface normal of the substrate) and its shape. The nanopyrramids are assumed to be large enough, so that the γ values for reconstructed surfaces in Table 6.1 can be applied. The relationship of the pyramidal geometry and the surface energy is discussed in the following subsection.

6.3.2 Deformation of pyramids

During epitaxial growth and ripening the shape of the islands may change. One example is the truncation of the small pyramids which results in a reduced aspect ratio, i.e., their height h divided by a characteristic base length a . For any regular pyramid the truncation is described by a parameter ($0 < \varepsilon < 1$)

$$\varepsilon = 1 - \frac{\gamma_{\text{top}}}{\gamma_{\text{side}}} \cos \theta \quad (6.3)$$

where θ is the angle between negative orientation of the base (or the orientation of the truncating plane) and one of the side facets. Thereby, we have assumed that the surface energy of the pyramid base is zero as a rough approximation for the interface energy between pyramid and substrate or wetting layer. The deviation $(1 - \varepsilon)$ of the parameter ε Eq. (6.3) from the case of an untruncated pyramid $\varepsilon = 0$ dominates the aspect ratio $h/a = m(1 - \varepsilon) \tan \theta$, where the geometry parameter m is equal to $1/2\sqrt{3}$ and $1/2$ for triangle- and square-based pyramids, respectively. For a pyramid with volume V the minimum surface energy F_s is given by

$$F_s = \frac{s\gamma_{\text{side}}}{\cos \theta} \left(\frac{3}{sm \tan \theta} V \right)^{\frac{2}{3}} (1 - \varepsilon^3)^{\frac{1}{3}} \quad (6.4)$$

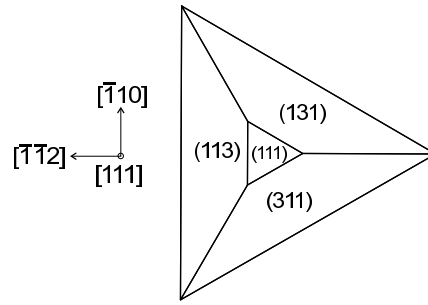


Figure 6.3 Top view of frustum of a [111]-oriented pyramid with {311} facets.

where the geometry parameter s is $\sqrt{3}/4$ for the triangle base and 1 for the square base. The comparison of the total surface energies for a given volume V gives an indication for the favored orientations of the facets and the trend for truncation of the pyramid.

Growth of Ge on Si(111) surfaces leads to nucleation of three-dimensional islands which consist of {113} facets as side walls and a flat top (111) facet [24]. The model of such a pyramidal island is presented in Fig. 6.3 with a $(\bar{1}\bar{1}\bar{1})$ triangle base, a (111) top, and three equivalent (113), (131) and (311) facets. In this case the angle θ is given by $\arccos(5/\sqrt{33})$ [i.e., 29.5°]. During the epitaxial growth the aspect ratio of an island may change as a function of the coverage. However, the form of the island is always a frustum of a tetrahedron and the complete pyramid with {113} facets is never reached [24]. Using values from Table 6.1 one finds for the parameter $\varepsilon = 0.31$ (C), 0.15 (Si), and 0.11 (Ge). The truncation can be interpreted as a consequence of the ECSs presented in Figs. 6.1 and 6.2. They show appearance of large {111} facets for diamond and relatively small {111} facets for Ge. A reduction of the surface energies of (111) faces till values corresponding to a 2×1 reconstruction [i.e., 1.45 (Ge) and 1.05 (Si) J/m²] also fulfills the condition for the truncation. For Ge the aspect ratio h/a results to 0.145 [with $\gamma(111)$ corresponding to $c(2 \times 8)$] or 0.15 [with $\gamma(111)$ corresponding to 2×1]. Indeed, this value varies from 0.1 to 0.135 during the growth [24]. Consequently, taking into account only surface energies, there is a tendency for truncation of a [111]-oriented triangle-based pyramid shown in Fig. 6.3.

At low growth temperatures or low Ge coverages the small Ge islands grown on Si(100) substrates are rectangular-based huts or square-based pyramids with {501} [19–22] or sometimes {301} [16] facets. In the case of InAs quantum dots on GaAs(100) substrates also {101} facets have been studied [9, 190, 191]. In order to model the pure surface energetics of small islands of this type, we consider a $(00\bar{1})$ square base with a $[00\bar{1}]$ normal and four equivalent facets with $[01n]$, $[0\bar{1}n]$, $[10n]$, and $[\bar{1}0n]$ orientations ($n = 1, 3, 5$) [see Fig. 6.4(a)]. The tilt angle θ of the facets is given by $\arccos(n/\sqrt{1+n^2})$ [i.e., 45° , 18.43° or 11.31°]. The truncation of the considered pyramids takes place for all group-IV elements. However, the tendency to cut a pyramid is stronger for the smaller n . For germanium the parameter Eq. (6.3) amounts to $\varepsilon = 0.37$ ($n = 1$), 0.21 ($n = 3$) and 0.11 ($n = 5$). Similar dependencies are found for Si and C. Assuming the value $\gamma(001) = 1.05$ J/m² for Ge, which corresponds to a 2×1 reconstruction, the value of truncation amounts only to $\varepsilon = 0.06$ and the aspect ratio is $h/a = 0.006$. Experi-

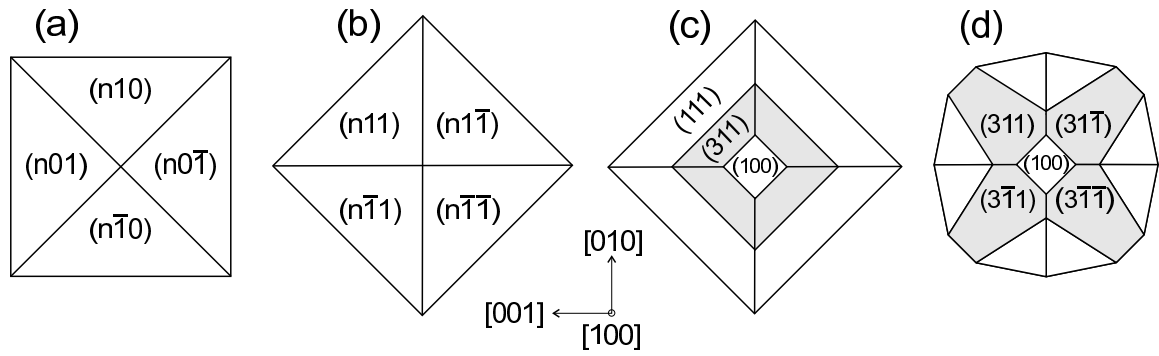


Figure 6.4 Top view of [100]-oriented pyramids or domes with $\{n01\}$ ($n = 5, 3, 1$), $\{n11\}$ ($n = 3, 1$) and $\{100\}$ facets. In (d) the facets without denotation represent $\{15\ 3\ 23\}$ facets.

mentally, the latter quantity was observed equal to 0.1 what nearly corresponds to the complete pyramid.

At higher Ge coverages of Si(100) substrates large Ge islands, so-called domes, appear. The domes are more rounded and display a multifaceted surface [22]. They are bounded by $\{113\}$ and $\{15\ 3\ 23\}$ facets. In the intermediate coverage regime also the occurrence of $\{105\}$ is discussed. Here, we neglect the rounding and only study another type of square-based pyramids with [001] orientation and four equivalent facets with $[11n]$, $[1\bar{1}n]$, $[\bar{1}1n]$, and $[\bar{1}\bar{1}n]$ surface normals where usually $n = 3$ but also other values such as $n = 1$ may be considered [see Fig. 6.4(b)]. Such shapes have been suggested for Si nanocrystallites [30]. In their case the tilt angle θ of the facets $\arccos(n/\sqrt{n^2 + 2})$, i.e., 54.74° ($n = 1$), 25.24° ($n = 3$), and 6.21° ($n = 13$), depends dramatically on the growth time. For short growth times even $\{1\ 1\ 13\}$ facets with $n = 13$ have been observed. They change over into $\{111\}$ facets with $n = 1$ for longer growth time.

Within the simplified picture Eq. (6.4) of the restriction to surface energies, one finds that $\{n11\}$ facets are more favorable than $\{n01\}$ facets. For large Ge nanocrystals, this finding is in agreement with the observation of $\{311\}$ facets instead of surfaces with $\langle 501 \rangle$ orientations [22]. According to Eq. (6.4) the total surface energy is three times smaller in the case of $\{311\}$ facets.

Again, we have to state that the total energy reduction may be also a driving force for the truncation of the pyramids with $\langle n11 \rangle$ facet orientations. The largest parameters ε occur for $n = 1$. Using the values from Table 6.1 one has $\varepsilon = 0.19$ (C) and 0.42 (Si and Ge). Consequently, the tendency for truncation is most pronounced for silicon and germanium. For $n = 3$ for these materials the values of ε with 0.09 (Si) and 0.08 (Ge) are much smaller. Truncation will not happen for $n > 1$ in the diamond case. For Si islands it has been observed that pyramids with $\{111\}$ facets transform into ones with $\langle 311 \rangle$ orientation at elevated temperature. Allowing that both $\{113\}$ and $\{111\}$ facets appear on the side walls the ratio of their heights $h(311)/h(111)$ is given by $2\gamma(001)/[\sqrt{11}\gamma(311) - \sqrt{3}\gamma(111)] - 1$. According to Table 6.1 this results to 0.23 (0.30) for Si (Ge) or 0.32 (0.37) if the energy of (111) surface is reduced to the value for the 2×1 reconstruction.

For Si and Ge the main difference between the ECSs derived by Wulff constructions shown in Fig. 6.2 and pyramid shapes discussed in this section (i.e. models of experimentally observed crystallites) is the number of occurring steep facets. In particular, for [100]-oriented pyramids one may consider another shell of {311} facets. This would give eight additional {311} ones. But they do not appear on islands during epitaxial growth. The reason seems to be related to the very large angle θ of these facets with the $\langle 100 \rangle$ orientation, namely 72.45° . Other facets corresponding to orientations with smaller θ are more likely. Surfaces with $\langle 111 \rangle$ and $\langle 110 \rangle$ orientations with θ equal to 54.74° and 45° , respectively, are good candidates. It is interesting that {110} facets which almost disappear on the ECS [see Figs. 6.2(b) and 6.2(c)] could lead to large facets on the [100]-oriented pyramid in addition to the discussed four {113} facets. For Si and Ge, in this case four facets with $\langle 110 \rangle$ orientation will occur near the bottom of the pyramid and a rounding of the base will take place [cf. Figs. 6.2(a) and 6.2(b)]. Moreover, for Si pyramids {111} facets have indeed been observed. That is not the case for heteroepitaxially grown Ge islands, for which also {110} facets have not been detected. Experimentally observed {15 3 23} facets have only a tilt angle of $\theta = 33.63^\circ$. A model of such a pyramid is shown in Fig. 6.2(d). Taking into account only surface energies the probability for facets with this surface orientation to appear in the corner between two neighboring {311} facets is rather high. It happens if the relation $\gamma(15\ 3\ 23) \lesssim 1.7\gamma(311)$ is fulfilled as the condition for the minimum of the total surface energy. As mentioned above for Ge (the softest material under consideration) surface energies of different orientations do not vary so much. Therefore, other effects than the energetics, e.g. strain, should stabilize such less sloping high-index facets.

For the surface energies given in Table 6.1 with a not too strong variation with the surface orientation we conclude that deviations from the ideal shape of the pyramids, such as truncation or rounding, are favorable within considerations restricted to the pure energetics of the facets. However, these results can only indicate a trend. Taking into account the strain of the pyramids the volume dependence of the total energy (6.2) is changed from $E_{\text{total}} = \alpha V^{\frac{2}{3}}$ to $E_{\text{total}} = \alpha V^{\frac{2}{3}} - \beta V$ [192]. Optimizations of energy functionals of such a type may give modified results. In particular, it is expected that the effects of truncation and rounding depend on the pyramid volume. Consequently, shape transitions as the transition from pyramids to domes observed for Ge on Si(100) can be only described taking into account the strain energy and/or kinetics effects and not only using an equilibrium theory with a restriction to the total surface energy.

Chapter 7

Summary and conclusions

We have presented extensive first-principles studies of the energetics and the reconstructions of the clean low-index (111), (110), (100) and high-index (113) surfaces of the three group-IV semiconductors diamond, silicon, and germanium. The calculations have been performed within DFT using the LDA and the repeated-slab approximation. Different reconstructions including the largest ones observed experimentally such as Si(111) 7×7 and Si(110) 16×2 have been investigated. The atomic geometries have been optimized in order to find the minimum of the total energy. For these atomic structures the electronic band structures have also been calculated. For the most interesting surface reconstructions STM images have been simulated in order to make a “direct” comparison with experimentally observed surface images. A combination of symmetric slabs and slabs with a hydrogen passivation at one side allowed the determination of absolute surface energies not only for unreconstructed surfaces. Such a combination of two different slab approximations makes the computations tractable and not too costly also for reconstructed surfaces with large unit cells.

In the case of (111) surfaces we have presented studies for the basic reconstructions 2×1 , $c(2\times 8)$, and 7×7 . The resulting energetics has been discussed in terms of the most important structural parameters and surface band structures of the π -bonded chain, adatom, and dimer-adatom-stacking-fault models. We found that the 2×1 reconstruction gives the lowest energy only for diamond. Within the theoretical methods used here the strange result of a metallic band structure of the C(111) 2×1 surface (measurements reveal an insulating behavior) cannot be avoided. For Si and Ge, the large 7×7 or $c(2\times 8)$ reconstructions are energetically more favorable. Chemical trends have been derived that indicate clear differences between the carbon atoms with a lack of p - and d -electrons in the core and the bigger Si or Ge atoms. In particular the strong C-C bonding is responsible for the absence of long-range adatom-induced reconstructions on C(111). Si and Ge surface structures gain more energy by the electron transfer between adatoms and rest atoms because of the accompanying smaller subsurface stresses. In the intermediate case of silicon, additional reconstruction elements occur to balance the different tendencies observed for diamond and germanium.

In general, a similar behavior occurs for the (100) surfaces. For Si and Ge, dimers are always asymmetric, the $c(4\times 2)$ reconstructions are lower in energy than the 2×1 ones. We have also found a very small energy difference between the lowest $c(4\times 2)$ phase and the $p(2\times 2)$ one.

In contrast, in the diamond case no asymmetric dimers occur at the (100) face. The tendency for stabilization of symmetric structures on diamond surfaces and the tendency for symmetry reductions at the Si and Ge surfaces are observed not only for the (111) 2×1 and (100) 2×1 translational symmetries but also for the relaxed (110) 1×1 faces, the latter being the ground state in the diamond case. Any buckling of chains or dimers induces a substantial subsurface strain and, hence, makes a symmetry break unlikely in the diamond case. Tilting of chains and dimers on Si and Ge surfaces opens energy gaps between surface states. The accompanying energetical lowering of the occupied bands gives rise to an energy gain. Moreover, such a tilting allows different chain isomers on the Si and Ge(111) surfaces and the $c(4\times 2)$ and $p(2\times 2)$ translational symmetries of the (100) surfaces of Si and Ge.

The 2×1 unit cell with symmetric tetramers has been shown to be the most stable C(113) surface. For the first time, total-energy calculations have been presented for this orientation of diamond crystals. Interestingly, the tetramer band structure exhibits a clear insulating character. The surface energy is even lower than that of the C(001) 2×1 surface. It could make the C(113) surfaces useful for future applications. Also in the Si(113) and Ge(113) cases, the formation of tetramers tends to give rise to a semiconducting surface. In particular, asymmetries due to the puckering of the tetramers support the opening of an energy gap between surface states. However, for Si and Ge the situation is more complicated since 3×1 and 3×2 translational symmetries have been observed experimentally. The presence of adatoms leads to metallic structures for all the materials as a consequence of the half-occupied adatom dangling bonds. No structure with tetramers and adatoms can overcome this problem, even assuming a certain asymmetry of the tetramer as it was proposed by several research groups. The Si and Ge(113) surfaces with 3×1 or 3×2 reconstructions have been confirmed to be stabilized only by subsurface self-interstitials. For germanium two considered interstitial-induced reconstructions, 3×1 AI and 3×2 ADI, can hardly be distinguished from an energetical point of view. The 3×2 AI reconstruction gives rise to a global minimum on the total-energy surface. Nevertheless, the small energy differences indicate that interstitial migration and coexistence of different surface phases should be likely. In the Si(113) case, due to a repulsive interaction of the interstitial atoms on short distances, the 3×2 ADI structure has been found to be most favorable. However, the energy differences to the other interstitial reconstructions remain also small. Within the stable reconstructions of the Si and Ge(113) surfaces only the 3×2 AI and 3×2 ADI structures give rise to insulating (semiconducting) band structures. The calculated electronic structures, in particular that of 3×2 ADI for Si(113), seem to agree with the available experimental data from PES, ARPES and STM. Important facts concern the occurrence of occupied surface states below the VBM and a strong asymmetry in the filled- and empty-state images. The energetics, the gap opening, and the similarities of the STM images suggest to interpret the experimental data available for ordered Si and Ge(113) surfaces in terms of the 3×2 translational symmetry.

We again conclude that the appearance of reconstruction elements on (113) surfaces, such as tetramers or interstitials, depends decisively on the group-IV element, C, Si or Ge. Buckling of the tetramers or subsurface interstitials are completely unfavorable for C(113). This result agrees with the tendency found for C(001) 2×1 and C(111) 2×1 surfaces that subsurface strains cost too much energy and that additional atoms are energetically unfavorable.

In order to understand the driving forces for the long-range Si(110) 16×2 and Ge(110) 16×2 [$c(8\times 10)$] surfaces we have first investigated a variety of reconstruction elements within smaller unit cells. Among the reconstruction elements buckled zig-zag chains, adatoms, rest atoms, dimers, bridge-site atoms, tetramers, pentamers and interstitial atoms have been studied. In general neighboring chains buckled in opposite directions and adatoms arranged along the [001] direction stabilize the (110) surfaces. For Ge adatom-rest atom pairs are the most stable reconstruction elements. In the case of Si the presence of only adatoms can lower the surface energy. For both semiconductors pure dimer structures and saturation of all dangling bonds by fourfold-coordinated adatoms are not possible. The tetramer-interstitial reconstructions on Si and Ge(110) surfaces are stabilized in the presence of additional adatoms. In this case the resulting pentamer atoms donate electrons to adatoms similar to the case of (113) surfaces. Dangling bonds of adatoms are fully occupied, which leads to a semiconducting band structure (at least for Si). Simulated empty-state STM images show pentagon-shaped spot distributions. The reconstruction element with two five-membered rings is completely unfavorable from the energetic point of view for both Si and Ge(110) surfaces, although this metastable structure can reproduce the two pentagons representing the part of a stripe in the empty-state STM images which is nearly equivalent to one unit cell.

For the first time we have performed *ab initio* calculations for the Si(110) surface using the observed 16×2 translational symmetry. Its unit cells nominally contain 64 atoms in each bulk-like atomic layer. We have shown that steps leading to trenches and upper as well as lower terraces are important reconstruction elements. An appropriate rebonding of the step atoms stabilizes the Si(110) 16×2 surface. This has been demonstrated starting from the adatom-like behavior of edge atoms and oppositely buckled zigzag chains on the different terraces. Therefore, the appearance of trenches on Si(110) surfaces in general, has been explained.

In order to model the stripes along the $[\bar{1}12]$ direction as observed by STM on both types of terraces, we have investigated different arrangements of adatoms. Their energetics significantly depends on the adatom distribution. An adatom arrangement in parallel lines along [001] directions with a distance of about $3a_0/\sqrt{2}$ lowers further the surface energy. A combination of stretched adatom-hexagons surrounded by partially removed chains yields a local minimum on the total-energy surface but not to a stable surface reconstruction. A very interesting coverage of the terraces is described by an ATI model. It gives rise to the lowest energy of all geometries studied. Still it is somewhat higher than the energy of the corresponding model studied for a 3×2 translational symmetry.

Within the ATI model, together with an interstitial atom four adatoms form a pentamer that can be combined with a varying number of adatoms. The situation may be more complicated due to the pentamer buckling. Obviously, such pentamers can yield to pentagonal shapes of spot arrangements in the STM images. However, their extent seems to be smaller than observed experimentally. On the other hand, such reconstruction elements can also give rise to spot arrangements with other shapes. It depends on the number and the occupation of the adatoms. Also edge atoms with an adatom character or adatoms in regions of removed chain atoms may drastically change the spot distribution because they may be hidden in the experimental STM images.

The ATI model represents a remarkable progress in explaining the atomic geometry of the Si(110) 16×2 surface. However, the accompanying surface energy gain and the resulting fine-structure of the STM images suggest to search for additional refinements of the reconstruction model. On the other hand, there is also no unique interpretation of the measured STM images. Consequently, more detailed structural, spectroscopic and total-energy studies should be performed. Further STM investigations with real atomic resolution on both upper and lower terraces, in particular near the steps are needed. This holds also for Ge.

Our *ab initio* total-energy and electronic-structure results highlight the physical origins of the reconstruction behavior in dependence on surface orientation and size of the group-IV atoms. We have shown clear evidence for an opposite reconstruction behavior of diamond and Si or Ge surfaces. Adatoms, interstitials, and symmetry-breaking distortions are unlikely for diamond as a consequence of the short interatomic distances and strong bonds. However, such elements of the surface reconstruction occur on Si and Ge surfaces. The complicated interplay of bonding, resulting atomic geometry, and accompanying electronic structure has been derived and used to discuss driving forces for the surface reconstruction.

The understanding of growth, appearance of thin films or nanocrystals, and the possible bridging of microscopic and macroscopic properties of the systems require a knowledge of thermodynamic quantities, in particular surface energies. We have presented a rather complete data base of absolute surface energies γ of group-IV semiconductors. For all the elements, there is a strong tendency to reduce substantially surface energies by taking into account surface reconstructions. In general, diamond surfaces possess large values of γ , while those for Si or Ge are about four or five times smaller, respectively. The dependence of the energies on the surface orientation is also different for diamond, Si and Ge. Apart from diamond, for which the {111} cleavage faces are really energetically favored, the energy variation for surfaces with orientations $\langle 111 \rangle$, $\langle 311 \rangle$, and $\langle 100 \rangle$ is rather weak for Si and Ge. Only the value for {110} facets is substantially larger. Ge surface energies tend to be almost equal independent of the surface orientation.

The absolute surface energies have been used to discuss the equilibrium shapes of three-dimensional crystals and [111]- or [100]-oriented pyramids or domes. We have shown that the ECSs depend very much on the absolute values of the surface energies. As a consequence we observed a shape variation from diamond via silicon to germanium. Interestingly, we have predicted that {311} facets should occur on the ECS of diamond. By contrast, in the case of Ge a more spherical shape has been predicted. The occurrence of high-index surfaces is also quite likely for Ge. Neglecting the influence of energy contributions due to edge bonding and strain, we have generally observed tendencies for [111]- and [100]-oriented pyramids to be deformed, i.e., tendencies towards truncation, base deformation, or faceting. The strength of such a trend depends on the overall shape and the values of γ .

Further steps in the field will have to include investigations of other high-index surfaces, in particular for Ge and Si. Their energetical relations and contributions to the ECSs are needed. Of course, models and a desirably quantitative description of nanocrystals in order to predict shape transitions still remain one of the most interesting topics in modern physics. An important

contribution to this problem has been done in the this work by presenting surface energies. Precise atomic arrangements of semiconductor surfaces obtained here are also necessary for further investigations of surfaces: In particular, optical spectra of Si(113) and Si(110) are very important to learn more about the electronic structure. However, in the case of such spectroscopic investigations self-energy corrections and other many-body effects have to be taken into account. Adsorption of foreign atoms and molecules usually needs an understanding of the clean surfaces at the first stage. Recently, the biofunctionalization of surfaces and nanostructures has become one of the focal points of research. Starting from knowledge about clean systems and nanostructures it will allow to learn more about the interaction between bio-molecules and metal or semiconductor surfaces. In this way, qualitatively new effects and devices will be enabled. The present thesis is thus a step towards the general understanding of such complex systems. It is hoped that its results spur further developments and motivate new experimental work.

Bibliography

- [1] M.A. Green, J. Zhao, A. Wang, P.J. Reece, and M. Gal, *Nature* **412**, 805 (2001).
- [2] L. Pavesi, L. Dal Negro, G. Mazzoleni, G. Franzo and F. Priola, *Nature* 408, **440** (2000).
- [3] A.G. Cullis, L.T. Canham, and P.D.J. Calcott, *Appl. Phys. Rev.* **82** 909 (1997).
- [4] W.L. Ng, M.A. Loenco, R.M. Gwilliam, G. Shao, and K.P. Hoemwood, *Nature* **410**, 192 (2001).
- [5] G. Franzo, S. Coffa, F. Priola, and C. Spinella, *J. Appl. Phys.* **81**, 2784 (1997).
- [6] A. Irrera, D. Pacifici, M. Miritello, *Physica E* **16**, 395(2003).
- [7] G. Franzo, D. Pacifica, V. Vinciguerra, F. Priola, and F. Iacona, *Appl. Phys.Lett.* **76**, 2167 (2000).
- [8] W.H. Chang, A.T. Chou, W.Y. Chen, H.S. Chang, T.M. Hsu, Z. Pei, P.S. Chen, S.W. Lee, L.S. Lai, S.C. Lu and M.-J. Tsai, *Appl.Phys. Lett.* **83** 2958 (2003).
- [9] V.A. Shchukin and D. Bimberg, *Rev. Mod Phys.* **71**, 1125 (1999).
- [10] H. Lüth, *Solid Surface, Interfaces and Thin Films* (Springer-Verlag, Berlin 2001)
- [11] J.A. Venables, *Introduction to Surface and Thin Film Processes* (Cambridge University Press, Cambridge 2000).
- [12] J. Tersoff and F.K. LeGoues, *Phys. Rev. Lett.* **72**, 3570 (1994).
- [13] M. Zinke-Allmang, L.C. Feldman, and M.H. Grabow, *Surf. Sci. Rep.* **16**, 377 (1992), and references therein.
- [14] I. Daruka, J. Tersoff, and A.-L. Barabási, *Phys. Rev. Lett.* **82**, 2753 (1999).
- [15] K.O. Ng and D. Vanderbilt, *Phys. Rev.* **B52**, 2177 (1995).
- [16] P. Raiteri, D.B. Migas, L. Miglio, A. Rastelli, and H.v. Känel, *Phys. Rev. Lett.* **88**, 256103 (2002).
- [17] I.N. Stranski and V.L. Krastanov, *Akad. Wiss. Lit. Mainz Math.-Natur. Kl. Iib* **146**, 797 (1939).
- [18] D.J. Eaglesham and M. Cerullo, *Phys. Rev. Lett.* **64**, 1943 (1990).
- [19] Y.-W. Mo, D.E. Savage, B.S. Swartzentruber, and M.G. Lagally, *Phys. Rev. Lett.* **65**, 1020 (1990).
- [20] A. Vailionios, B. Cho, G. Glass, P. Desjardins, D. Cahill, and J. Greene, *Phys. Rev. Lett.* **85**, 3672 (2000).
- [21] G. Medeiros-Ribeiro, A.M. Bratkovski, T.L. Kamins, D.A.A. Ohlberg, and R.S. Williams, *Science* **279**, 353 (1998).

- [22] F.M. Ross, R.M. Tromp, and M.C. Reuter, *Science* **286**, 1931 (1999).
- [23] A. Malachias, S. Kycia, G. Medeiros-Ribeiro, R. Magalhães-Paniago, T.I. Kamins, and R.S. Williams, *Phys. Rev. Lett.* **91**, 176101 (2003).
- [24] B. Voigtländer, *Surf. Sci. Rep.* **43** 127 (2001).
- [25] K. Komlev, B. Schröter, and W. Richter, private communication.
- [26] J.R. Bermond, J.J. Métois, X. Egéa, and F. Floret, *Surf. Sci.* **330**, 48 (1995).
- [27] D.J. Eaglesham, A.E. White, L.C. Feldman, N. Moriya, and D.C. Jacobson, *Phys. Rev. Lett.* **70**, 1643 (1993).
- [28] H. Hirayama, M. Hiroi, and T. Ide, *Phys. Rev.* **B48**, 17331 (1993).
- [29] L. Vescan, K. Grimm, and C. Dieker, *J. Vac. Sci. Technol.* **B16**, 1549 (1998).
- [30] M. Shibata, Y. Nitta, K. Fujita, and M. Ichikawa, *Phys. Rev.* **B61**, 7499 (2000).
- [31] V. ShklyaeV and V. Zielasek, *Surf. Sci.* **541**, 234 (2003)
- [32] H. Baumgärtner, F. Kaesen, H. Gossner, and I. Eisele, *Appl. Surf. Sci.* **130-132**, 747 (1998).
- [33] J.E. Field, *The properties of Natural and Synthetic Diamond* (Academic, London 1992)
- [34] G. Kowalski, M. Moore, G. Gledhill, and Z. Maričić, *Diamond and Rel. Materials* **5**, 1254 (1996).
- [35] K.W. Chae and Y.-J. Baik, *Diamond and Related Materials* **8**, 1261 (1999).
- [36] S.T. Lee, H.Y. Peng, X.T. Zhou, N. Wang, C.S. Lee, I. Bello, and Y. Lifshitz, *Science* **287**, 104 (2000).
- [37] J.J Métois, P. Müller, *Surf. Sci.* **548**, 13 (2004).
- [38] J.H. Wilson, J.D. Todd, and A.P. Sutton, *J. Phys. Condens. Matter* **2**, 10259 (1990); **3**, 1971 (1991).
- [39] G.H. Gilmer and A.F. Bakker, *Mater. Res. Soc. Symp. Proc.* **209**, 135 (1991).
- [40] T. Takai, T. Halicioglu, and W.A. Tiller, *Surf. Sci.* **164**, 327 (1985).
- [41] G. Kern, J. Hafner, and G. Kresse, *Surf. Sci.* **366**, 445 + 464 (1996).
- [42] G. Kern and J. Hafner, *Phys. Rev.* **B56**, 4203 (1997).
- [43] G. Wulff, *Z. Kristallogr. Mineral* **34**, 449 (1901).
- [44] F. Bechstedt, *Principles of Surface Physics* (Springer, Berlin 2003).
- [45] D.J. Chadi, *Phys. Rev. Lett.* **43**, 43 (1979).
- [46] W. Mönch, *Semiconductor Surfaces and Interfaces* (Springer, Berlin 2001).
- [47] C. Kress, M. Fiedler, W.G. Schmidt, and F. Bechstedt, *Phys. Rev.* **B50**, 17697 (1994).

- [48] P. Krüger and J. Pollmann, *Phys. Rev. Lett.* **74**, 1155 (1995).
- [49] S. Sagisaka, D. Fujita, and G. Kido, *Phys. Rev. Lett.* **91**, 146103 (2003).
- [50] Y. Takagi, Y. Yoshimoto, K. Nakatsuji, and K. Komori, *J. Phys. Soc. Jpn.* **72**, 2425 (2003).
- [51] K.C. Pandey, *Phys. Rev. Lett.* **47**, 1913 (1981); **49**, 223 (1982).
- [52] J.E. Northrup and M.L. Cohen, *Phys. Rev. Lett.* **49**, 1349 (1982).
- [53] S. Iarlori, G. Galli, F. Gygi, M. Parinello, and E. Tosatti, *Phys. Rev. Lett.* **69**, 2947 (1992).
- [54] B.N. Davidson and W.E. Pickett, *Phys. Rev.* **B49**, 11253 (1994).
- [55] A. Scholze, W.G. Schmidt, and F. Bechstedt, *Phys. Rev.* **B53**, 13725 (1996).
- [56] S.-H. Lee and M.-H. Kang, *Phys. Rev.* **B54**, 1482 (1996).
- [57] M. Rohlfing, M. Palumbo, G. Onida, and R. Del Sole, *Phys. Rev. Lett.* **85**, 5440 (2000).
- [58] N. Takeuchi, A. Selloni, A.I. Shkrebtii, and E. Tosatti, *Phys. Rev.* **B44**, 13611 (1991).
- [59] H. Hirayama, N. Sugihara, and K. Takayanagi, *Phys. Rev.* **B62**, 6900 (2000).
- [60] R.E. Schlier and H.E. Farnsworth, *J. Chem. Phys.* **30**, 917 (1959).
- [61] P.W. Palmberg and W.T. Peria, *Surf. Sci.* **6**, 57 (1967).
- [62] K. Takayanagi, Y. Tanishiro, M. Takahashi, and S. Takahashi, *J. Vac. Sci. Technol.* **A3**, 1502 (1985); *Surf. Sci.* **164**, 367 (1985).
- [63] G.-X. Qian and D.J. Chadi, *Phys. Rev.* **B35**, 1288 (1987).
- [64] K.D. Brommer, M. Needels, B.E. Larson, and J. Joannopoulos, *Phys. Rev. Lett.* **68**, 1355 (1992).
- [65] I. Stich, M.C. Payne, R.D. King-Smith, and J.-S. Lin, *Phys. Rev. Lett.* **68**, 1351 (1992).
- [66] R.S. Becker, B.S. Swartzentruber, J.S. Vickers, and T. Klitsner, *Phys. Rev.* **B39**, 1633 (1989).
- [67] N. Takeuchi, A. Selloni, and E. Tosatti, *Phys. Rev. Lett.* **69**, 648 (1992).
- [68] M. Koike, Y. Einaga, H. Hirayama, and K. Takayanagi, *Phys. Rev.* **B55**, 15444 (1997).
- [69] N. Takeuchi, *Phys. Rev.* **B57**, 6255 (1998).
- [70] D. Vanderbilt, *Phys. Rev.* **B36**, 6209 (1987).
- [71] P.G. Lurie and J. M. Wilson, *Surf. Sci.* **65**, (1977) 453.
- [72] Y. Yamamoto, *Phys. Rev.* **B50**, 8534 (1994).
- [73] Y. Yamamoto, T. Sueyoshi, T. Sato, and M. Iwatsuki, *Surf. Sci.* **466**, 183 (2000).
- [74] H. Ampo, S. Miura, K. Kato, Y. Ohkawa, and A. Tamura, *Phys. Rev.* **B34**, 2329 (1986).
- [75] T. An, M. Yoshimura, I. Ono, and K. Ueda, *Phys. Rev. B* **61**, 3006 (2000).

- [76] B.A. Nesterenko, A.V. Brovii, and A.T. Sorokovykh, *Surf. Sci.* **171**, 495 (1986).
- [77] E.J. van Loenen, D. Dijkkamp, and A.J. Hoeven, *J. Microsc.* **152**, 487 (1988).
- [78] B.X. Olshanetsky, A.M. Kepinsky, and A.A. Shklyaev, *Surf. Sci.* **64**, 224 (1977).
- [79] Z. Gai, R.G. Zhao, and W.S. Yang, *Phys. Rev. B* **57**, R6795 (1998).
- [80] H. Noro and T. Ichikawa, *Jpn J. Appl. Phys.* **24**, 1288 (1985).
- [81] T. Ichikawa, *Surf. Sci.* **544**, 58 (2003).
- [82] W.E. Packard and J.D. Dow, *Phys. Rev.* **B55**, 15643 (1997).
- [83] A.I. Shkrebtii, C.M. Bertoni, R. Del Sole, and B.A. Nesterenko, *Surf. Sci.* **239**, 227 (1990).
- [84] J. Dabrowski, H.-J. Müssig, and G. Wolff, *Phys. Rev. Lett.* **73**, 1660 (1994).
- [85] M. Menon, N.N. Lathiotakis, and A.N. Andriotis, *Phys. Rev.* **B56**, 1412 (1997).
- [86] N. Takeuchi, *Surf. Sci.* **494**, 21 (2001).
- [87] H. Omi and T. Ogino, *Phys. Rev.* **B59**, 7521 (1999).
- [88] W. Ranke, *Phys. Rev.* **B41**, 5243 (1990).
- [89] J. Knall, J.B. Pethica, J.D. Todd, and J.H. Wilson, *Phys. Rev. Lett.* **66**, 1733 (1991).
- [90] U. Myler, P. Althainz, and K. Jacobi, *Surf. Sci.* **251/252**, 607 (1991).
- [91] J. Schreiner, K. Jacobi, and W. Selke, *Phys. Rev.* **B49**, 2706 (1994).
- [92] J. Dabrowski, H.-J. Müssig, and G. Wolf, *Surf. Sci.* **331-333**, 1022 (1995).
- [93] H. Sakama, D. Kunimatsu, M. Kageshima, and A. Kawazu, *Phys. Rev.* **B53**, 6927 (1996).
- [94] H. Hibino and T. Ogino, *Phys. Rev.* **B56**, 4092 (1997).
- [95] Z. Gai, R.G. Zhao, and W.S. Yang, *Phys. Rev.* **B56**, 12303 (1997).
- [96] T. Suzuki, H. Minoda, Y. Tanishiro, and K. Yagi, *Surf. Rev. Lett.* **5**, 249 (1998).
- [97] H. Vogler, A. Iglesias, W. Moritz, and H. Over, *Phys. Rev.* **B57**, 2315 (1998).
- [98] H. Ikeda, Y. Oshima, H. Hirayama, K. Takayanagi, *Surf. Sci.* **433-435**, 632 (1999).
- [99] A. Iglesias, M. Gierer, D. Wolf, and W. Moritz, *Surf. Sci.* **442**, 357 (1999).
- [100] C.C. Hwang, H.S. Kim, Y.K. Kim, J.S. Kim, C.Y. Park, K.J. Kim, T.-H. Kang, and B. Kim, *Phys. Rev.* **B59**, 14864 (1999).
- [101] C.Y. Chang, Y.C. Chou, and C.M. Wei, *Phys. Rev.* **B59**, R10453 (1999).
- [102] K.S. An, C.C. Hwang, H.S. Kim, C.-Y. Park, I. Matsuda, H.W. Yeom, S. Suga, and A. Kakizaki, *Surf. Sci.* **478**, 123 (2001).
- [103] M. Takeguchi, M. Tanaka, H. Yasuda, and K. Furuya, *Surf. Sci.* **482-485**, 1385 (2001).

- [104] C.C. Hwang, H.S. Kim, Y.K. Kim, K.W. Ihm, C.Y. Park, K.S. An, K.J. Kim, T.-H. Kang, and B. Kim, *Phys. Rev.* **B64**, 045305 (2001).
- [105] C.C. Hwang, K.-J. Kim, T.-H. Kang, B. Kim, Y. Chung, and C.Y. Park, *Surf. Sci.* **514**, 319 (2002).
- [106] J. Wang, A.P. Horsfield, D.G. Pettifor, and M.C. Payne, *Phys. Rev.* **B54**, 13744 (1996).
- [107] J. Dabrowski, H.-J. Müssig, and G. Wolff, *J. Vac. Sci. Technol.* **B13**, 1597 (1995).
- [108] A. Laracuente, S.C. Erwin, and L.J. Whitman, *Phys. Rev. Lett.* **81**, 5177 (1998).
- [109] D.M. Bird, L.J. Clarke, R.D. King-Smith, M.C. Payne, I. Stich, and A.P. Sutton, *Phys. Rev. Lett.* **69**, 3785 (1992).
- [110] K.A. Feng, X.M. Hu, Z. Lin, and Y.R. Xing, *Appl. Surf. Sci.* **120**, 94 (1997).
- [111] Y.P. Feng, T.H. Wee, C.K. Ong, and H.C. Poon, *Phys. Rev.* **B54**, 4766 (1996).
- [112] C.B. Duke, *Chem. Rev.* **96**, 1237 (1996).
- [113] M.D. Pashley, *Phys. Rev.* **B40**, 10481 (1989).
- [114] M. Born and J.K. Oppenheimer, *Ann. Physik* **84**, 457 (1927).
- [115] J.C. Slater, *Phys. Rev.* **34**, 1293 (1929).
- [116] D.R. Hartree, *Proc. Cambridge Phil. Soc.* **24**, 89 (1928); *Mem. Manchester Phil. Soc.* **77**, 91 (1932-1933).
- [117] V. Fock, *Z. Physik* **61**, 126 (1930).
- [118] P. Hohenberg and W. Kohn, *Phys. Rev.* **136**, B864 (1964).
- [119] W. Kohn and L.J. Sham, *Phys. Rev.* **140**, A1133 (1965).
- [120] R.M. Dreizler and E.K.U. Gross *Density Functional Theory* (Springer Publ., Berlin 1990)
- [121] D.M. Ceperley and B.I. Alder, *Phys. Rev. Lett.* **45**, 566 (1980).
- [122] J.P. Perdew and A. Zunger, *Phys. Rev.* **B23**, 5048 (1981).
- [123] J.P. Perdew, in *Electronic Structure of Solids '91*, ed. by P. Ziesche and H. Eschrig (Akademie-Verlag, Berlin 1991).
- [124] W.A. Harrison, *Electronic Structure and the Properties of Solids* (Dover Publ., New York 1989).
- [125] A. Görling, *Phys. Rev. A* **54**, 3912 (1996); *Phys. Rev. Lett.* **85**, 4229 (2000).
- [126] R.W. Godby, M. Schlüter, and L.J. Sham, *Phys. Rev. B* **37**, 10159 (1988).
- [127] M.S. Hybertsen and S.G. Louie, *Phys. Rev. Lett.* **55**, 1418 (1985); *Phys. Rev.* **B34**, 5390 (1986).
- [128] R.W. Godby, M. Schlüter, and L.J. Sham *Phys. Rev. Lett.* **56**, 2415 (1986); *Phys. Rev.* **B35**, 4170 (1987).

- [129] J. Tersoff and D.R. Hamann, Phys. Rev. **B31**, 805 (1985).
- [130] H. Hellmann, *Einführung in die Quantenchemie*, Deuticke, Leipzig (1937).
- [131] R.P. Feynmann, Phys. Rev. **B56**, 340 (1939).
- [132] M. Scheffler, J.P. Vigneron, and G.B. Bachelet Phys. Rev. **B31**, 6541 (1985).
- [133] D.J. Chadi and M.L. Cohen, Phys. Rev. **B8**, 5747 (1973).
- [134] H.J. Monkhorst and J.D. Pack, Phys. Rev. **B13**, 5189 (1976).
- [135] R.A. Evarestov and V.P. Smirnov, Phys. Status Solidi b **119**, 9 (1983).
- [136] M.H. Cohen and V. Heine, Phys. Rev. **122**, 1821 (1961).
- [137] J.C. Phillips and L. Kleinman, Phys. Rev. **116**, 287 (1959).
- [138] D.R. Hamann, M. Schlüter, and C. Chiang Phys. Rev. Lett. **43**, 1494 (1979).
- [139] S.G. Louie, S. Froyen, and M.L. Cohen, Phys. Rev. **B26**, 1738 (1982).
- [140] H.S. Greenside and M. Schlüter, Phys. Rev. **B28**, 535 (1983).
- [141] Wenzien, P. Käckell, and F. Bechstedt, Surf. Sci. **989**, 307 (1994).
- [142] D. Vanderbilt, Phys. Rev. **B41**, 7892 (1990).
- [143] G. Kresse and J. Hafner, J. Phys.: Condens. Matter **6**, 8245 (1994).
- [144] J. Furthmüller, P. Käckell, F. Bechstedt, and G. Kresse, Phys. Rev. **B61**, 4576 (2000).
- [145] G. Kresse and J. Furthmüller, Comput. Mater. Sci. **6**, 15 (1996), Phys. Rev. **B54**, 11169 (1996).
- [146] [http : //cms.mpi.univie.ac.at/CMSPage/main](http://cms.mpi.univie.ac.at/CMSPage/main)
- [147] M.P. Teter, M. C. Payne, and D. C. Allan Phys. Rev. **B40**, 12225 (1989).
- [148] D.M. Bylander, L. Kleinman, and S. Lee Phys. Rev. **B42**, 1394 (1990).
- [149] E.R. Davidson, *Methods in Computational Molecular Physics* edited by G.H.F. Diercksen and S. Wilson Vol. **113 NATO advanced Study Institute, Series C** (Plenum, New York, 1983), p. 95.
- [150] B. Liu, in *Report on Workshop "Numerical Algorithms in Chemistry: Algebraic Methods"* edited by C. Moler and I. Shavitt (Lawrence Berkley Lab. Univ. of California, 1978), p. 49.
- [151] D.M. Wood and A. Zunger, J. Phys. A, **18** 1343 (1985).
- [152] D.D. Johnson, Phys. Rev. **B38**, 12087 (1988).
- [153] S. Blügel, PhD Thesis, RWTH Aachen (1988).
- [154] P. Pulay, Chem. Phys. Lett. **73**, 393 (1980).
- [155] L. Landau, E. M. Lifshitz, *Statistical physics*, Vol. 5 (Pergamon, Oxford 1959).

- [156] M.-C. Desjonquères, D. Spanjaard: *Concepts of Surface Physics* (Springer, Berlin 1996).
- [157] J.W. Gibbs, *The Scientific Papers*, Vol. 1 (Dover, New York 1961)
- [158] C. Herring, Phys. Rev. **82**, 87 (1951).
- [159] C. Herring: *The Use of Classical Macroscopic Concepts in the Surface-Energy Problem*, in: *Structure and Properties of Solid Surfaces*, ed. by R. Gomer and C.S. Smith (University of Chicago Press, Chicago 1953), p. 5.
- [160] <http://www.ctcms.nist.gov/wulffman>
- [161] K. Inoue, Y. Morikawa, K. Terakura and M. Nakayama, Phys. Rev. **B49**, 14774 (1994).
- [162] A. Ramstad, G. Brocks, and P.J. Kelly, Phys. Rev. **B51**, 14504 (1995).
- [163] J. Fritsch, and P. Pavone, Surf. Sci. **159**, 344 (1995).
- [164] K. Seino, W.G. Schmidt, and F. Bechstedt, Phys. Rev. Lett. (in press).
- [165] S.C. Erwin, A.A. Baski, and L.J. Whitman, Phys. Rev. Lett. **77**, 687 (1996)
- [166] W.G. Schmidt, A. Scholze, and F. Bechstedt, Surf. Sci. **351**, 183 (1996).
- [167] J.E. Northrup, M.S. Hybertsen, and S.G. Louie, Phys. Rev. Lett. **66**, 500 (1991).
- [168] F. Bechstedt, W.G. Schmidt, and A. Scholze, Europhys. Lett. **35**, 585 (1996).
- [169] H.J. Gossmann, J.C. Bean, L.C. Feldman, E.G. McRae, and I.K. Robinson, Phys. Rev. Lett. **55**, 1106 (1985).
- [170] P. Molinas-Mata, A.J. Mayne, and G. Dujardin, Phys. Rev. Lett. **80**, 3101 (1998).
- [171] J. Furthmüller, J. Hafner, and G. Kresse, Phys. Rev. **B53**, 7334 (1996).
- [172] J.J. Gilman, J. Appl. Phys. **31**, 2208 (1960).
- [173] S.Y. Tong, H. Huang, C.M. Wei, W.E. Packard, F.K. Men, G. Glander, and M.B. Webb, J. Vac. Sci. Technol. **A6**, 615 (1988).
- [174] R.J. Hamers, R.M. Tromp, and J.E. Demuth, Phys. Rev. Lett. **56**, 1972 (1986).
- [175] T. Uchihashi, Y. Sugawara, T. Tsukamoto, M. Ohta, S. Morita, and M. Suzuki, Phys. Rev. **B56**, 9834 (1997).
- [176] S.H. Ke, T. Uda, and K. Terakura, Phys. Rev. **B62**, 15319 (2000).
- [177] K.D. Brommer, M. Galván, A. Dal Pino, and J.D. Joannopoulos, Surf. Sci. **314**, 57 (1994).
- [178] W. Ranke and Y.R. Xing, Phys. Rev. **B31**, 2246 (1985).
- [179] U. Myler and K. Jacobi, Surf. Sci. **220**, 353 (1989).
- [180] S.M. Sholz, J. Schreiner, and K. Jacobi, Surf. Sci. **331**, 402 (1995).
- [181] U. Grossner, J. Furthmüller, and F. Bechstedt, Phys. Rev. **B58**, R1722 (1998).

- [182] M. Yoshimura, T. An, and K. Ueda, *Jpn. J. Appl. Phys.* **39**, 4432 (1999).
- [183] E.G. Keim, H. Wormeester, and A. van Silfhout, *J. Vac. Sci. Techn. A* **8**, 2747 (1990).
- [184] A. Cricenti, B. Nesterenko, P. Perfetti, and C. Sebenne, *J. Vac. Sci. Technol. A* **14**, 2448 (1996).
- [185] R.J. Jaccodine, *J. Electrochem. Soc.* **110**, 524 (1963).
- [186] Y. Fujikawa, K. Akiyama, T. Nagao, T. Sakurai, M.G. Lagally, T.Hashimoto, Y. Morikawa, and K. Terakura, *Phys. Rev. Lett.* **88**, 176101 (2002).
- [187] C.-S. Yan, Y.K. Vohra, H.-K. Mao, and R.J. Hemley, *Proc. Nat. Acad. Sci.* **99**, 12523 (2002).
- [188] Z. Gai, W.S. Yang, R.G. Zhao, and T. Sakurai, *Phys. Rev.* **B59**, 15230 (1999).
- [189] Q.K.K. Liu, N. Moll, M. Scheffler, and E. Pehlke, *Phys. Rev.* **B60**, 17008 (1999).
- [190] N. Moll, Ph.D. thesis (Technical University Berlin, Berlin 1998).
- [191] L.G. Wang, P. Kratzer, N. Moll, and M. Scheffler, *Phys. Rev.* **B62**, 1897 (2000).
- [192] F.M. Ross, J. Tersoff, and R.M. Tromp, *Phys. Rev. Lett.* **80**, 984 (1998).

Publications

Some results contained in this thesis have already been published in the following articles:

1. *Origin of the different reconstructions of diamond, Si, and Ge(111) surfaces*,
F. Bechstedt, A.A. Stekolnikov, J. Furthmüller, and P. Käckell,
Phys. Rev. Lett. **87**, 016103, (2001).
2. *Surface energies of Ge and Si and consequences for nanocrystallites*,
A.A. Stekolnikov, J. Furthmüller, P. Käckell, and F. Bechstedt,
in *Physics, Chemistry and Application of Nanostructures*, ed. by V.E. Borisenko et al., pp.160-163
(World Scientific, Singapur 2001).
3. *Absolute surface energies of group-IV semiconductors:
Dependence on orientation and reconstruction*,
A.A. Stekolnikov, J. Furthmüller, and F. Bechstedt,
Phys. Rev. B **65**, 115318 (2002).
4. *Adatoms, dimers, and interstitials on group-IV(113) surfaces: First-principles
studies of energetical, structural, and electronic properties*,
A.A. Stekolnikov, J. Furthmüller, and F. Bechstedt,
Phys. Rev. B **67**, 195332 (2003).
5. *Tetramers on diamond, Si, and Ge(113) surfaces: Ab initio studies*,
A.A. Stekolnikov, J. Furthmüller, and F. Bechstedt,
Phys. Rev. B **68**, 205306 (2003).
6. *Structural elements on reconstructed Si and Ge(110) surfaces*,
A.A. Stekolnikov, J. Furthmüller, and F. Bechstedt,
Phys. Rev. B **70**, 045305 (2004).
7. *Long-range surface reconstruction: Si(110)16×2*,
A.A. Stekolnikov, J. Furthmüller, and F. Bechstedt,
Phys. Rev. Lett. **93**, 136104 (2004).
8. *Shape of free and constrained group-IV crystallites: Influence of surface energies*,
A.A. Stekolnikov and F. Bechstedt,
Phys. Rev. B (submitted).

Zusammenfassung

Auf der Basis erster Prinzipien haben wir umfangreiche Untersuchungen der Energetik und der Rekonstruktionen von sauberen Oberflächen der drei Gruppe-IV-Halbleiter Diamant, Silizium und Germanium mit den niedrigen Indizierungen (111), (110), (100) bzw. mit dem hohen Index (113) vorgestellt. Die Rechnungen wurden im Rahmen der Dichtefunktionaltheorie (DFT) unter Verwendung der Näherung der lokale Dichte (LDA) und periodisch wiederholten Schichten durchgeführt. Es wurden unterschiedliche Rekonstruktionen untersucht, einschließlich der größten experimentell gefundenen Si(111)7×7- und Si(110)16×2-Rekonstruktionen. Die atomare Geometrie wurde im Hinblick auf die Minimierung der Gesamtenergie optimiert. Für die daraus erhaltenen Oberflächen Strukturen wurden ferner die elektronischen Bandstrukturen berechnet, und für die interessantesten Rekonstruktionen wurden auch STM-Bilder simuliert, um sie unmittelbar mit experimentell beobachteten Bildern der Oberflächen zu vergleichen. Eine Kombination symmetrischer Schichten und solchen, die auf einer Seite mit Wasserstoff passiviert sind, ermöglicht die Bestimmung absoluter Oberflächenenergien nicht nur für die unrekonstruierten Oberflächen. Eine solche Kombination der unterschiedlichen Schichtnäherungen führt zu handhabbaren Rechnungen, die auch für rekonstruierte Oberflächen mit großen Einheitszellen nicht zu aufwendig werden.

Für die (111)-Oberflächen haben wir Untersuchungen der grundlegenden 2×1-, *c*(2×8)-, und 7×7-Rekonstruktionen vorgestellt. Die resultierende Energetik wurde in Hinblick auf die wichtigsten strukturellen Parameter und die Oberflächenbandstruktur der Modelle mit Ketten π -gebundener Atome, Adatome bzw. Dimer-Adatom-Stapelfehler diskutiert. Es wurde festgestellt, daß die 2×1-Rekonstruktion nur für Diamant die niedrigste Gesamtenergie besitzt. Für Silizium und Germanium sind die großen 7×7- bzw. *c*(2×8)-Rekonstruktionen energetisch günstiger. Die abgeleiteten chemischen Trends weisen auf deutliche Unterschiede zwischen den Kohlenstoffatomen, die keine *p*- und *d*-Elektronen im Rumpf haben, und den größeren Silizium- bzw. Germaniumatomen hin. Insbesondere die starke C-C-Bindung ist dafür verantwortlich, daß es keine von Adatomen erzeugten langreichweitigen Rekonstruktionen der Diamant-(111)-Oberflächen gibt. Silizium- und Germaniumoberflächenstrukturen hingegen erfahren einen Energiegewinn durch Elektronentransfer zwischen Adatomen und Restatomen, weil dies nur mit kleinen Verspannungen unterhalb der Oberflächen verbunden ist. Im intermediären Fall des Silizium treten zusätzliche Rekonstruktionselemente auf, die die unterschiedlichen Tendenzen, wie sie für Diamant und für Germanium vorgestellt wurden, ausbalancieren.

Im allgemeinen tritt ein solches Verhalten auch bei den (100)-Oberflächen auf. Weil die Si- und Ge-Dimere immer asymmetrisch sind, ergibt sich für die *c*(2×4)-Rekonstruktionen immer eine niedrigere Energie als für die 2×1-Rekonstruktionen. Wir haben außerdem eine sehr kleine Energiedifferenz zwischen der niederenergetischen *c*(2×4)- und der *p*(2×2)-Phase gefunden. Im Gegensatz dazu treten für Diamant keine asymmetrischen Dimere auf der (100)-Oberfläche auf. Die Tendenz zur Stabilisierung symmetrischer Strukturen bei Diamantoberflächen und bei Si- und Ge-Oberflächen tritt nicht nur bei den (111)2×1- und (100)2×1-, sondern auch bei den (100)2×1- und den relaxierten (110)1×1-Oberflächen auf. Letztere stellt den Grundzustand bei Diamant dar. Jegliche Verkippung von Atomketten oder Dimeren bewirkt eine er-

hebliche Verzerrung unterhalb der Oberfläche, die mit einer Erhöhung der elastischen Energie verbunden ist und daher bei Diamant einen Symmetriebruch unwahrscheinlich macht. Bei Si- und Ge-Oberflächen führt eine Verkippung von Atomketten bzw. Dimeren zu Energielücken zwischen Oberflächenzuständen. Die damit verbundene energetische Absenkung der besetzten Bänder bewirkt einen Energiegewinn. Darüberhinaus ermöglicht die Verkippung das Vorkommen verschiedener isomerer Ketten auf den Si- und Ge(111)-Oberflächen sowie von $c(4 \times 2)$ - und $p(2 \times 2)$ -Symmetrien auf (100)-Oberflächen von Si und Ge.

Die 2×1 -Einheitszelle mit symmetrischen Tetrameren wurde als Element der stabilsten C(113)-Oberfläche identifiziert. Zum ersten Mal wurden Gesamtenergierechnungen für diese Oberflächenorientierung von Diamant vorgestellt. Interessanterweise zeigt die Bandstruktur der Tetramere eindeutig einen isolierenden Charakter. Die zugehörige Oberflächenenergie ist sogar niedriger als die der C(001) 2×1 -Oberfläche. Dies könnte die C(113)-Oberfläche für zukünftige Anwendungen interessant machen. Auch bei Si(113)- und Ge(113)-Oberflächen führt die Bildung von Tetrameren zu einer halbleitenden Oberfläche. Insbesondere die mit der Verzerrung der Tetramere verbundene Asymmetrie unterstützt die Öffnung von Bandlücken zwischen den Oberflächenzuständen.

Die Situation ist bei Si und Ge jedoch komplizierter, weil auch 3×1 - und 3×2 -Symmetrien beobachtet wurden. Adatome führen bei allen untersuchten Materialien zu metallischen Strukturen infolge der halbbesetzten freien Bindungen der Adatome. Keine Struktur mit Tetrameren und Adatomen kann dieses Problem beseitigen, selbst wenn man eine gewisse Asymmetrie der Tetramere annimmt, wie es von verschiedenen Gruppen vorgeschlagen wurde. Es wurde bestätigt, daß die Si- und Ge(113)-Oberflächen mit 3×1 - und 3×2 -Rekonstruktionen nur durch die Besetzung von Zwischengitterplätzen unterhalb der Oberfläche stabilisiert werden. Bei Germanium können zwei derartige Rekonstruktionen, das 3×1 -AI- und das 3×2 -ADI-Modell, energetisch kaum unterschieden werden. Die 3×2 -AI-Rekonstruktion führt zu einem globalen Minimum auf der Gesamtenergiefläche. Jedoch weisen die kleinen Energiedifferenzen darauf hin, daß eine wechselnde Besetzung der Zwischengitterplätze durch Migration sowie die Koexistenz verschiedener Rekonstruktionen wahrscheinlich ist. Im Fall von Si(113) ist die 3×2 -ADI-Struktur aufgrund einer abstoßenden Wechselwirkung der Zwischengitteratome für kleine Abstände energetisch bevorzugt. Andererseits fallen auch hier die Energieunterschiede zu den anderen auf Zwischengitteratomen beruhenden Rekonstruktionen gering aus. Von den stabilen Rekonstruktionen der Si- und Ge(113)-Oberfläche sind nur die 3×2 -AI- und die 3×2 -ADI-Strukturen halbleitend. Die berechneten elektronischen Strukturen, insbesondere die der Si(113) 3×2 -ADI-Rekonstruktion, stimmen augenscheinlich mit experimentellen Ergebnissen überein, die aus PES-, ARPES- und STM-Messungen erhalten wurden. Wichtig sind dabei das Auftreten besetzter Oberflächenzustände unterhalb des Valenzbandmaximums sowie eine deutliche Asymmetrie zwischen den STM-Bildern für besetzte und leere Zustände. Insgesamt sprechen die Energetik, das Auftreten von Bandlücken und die Ähnlichkeiten der STM-Bilder für eine Interpretation der experimentellen Befunde bei geordneten Si- und Ge(113)-Oberflächen im Sinne einer 3×2 -Symmetrie.

Wir kommen damit wiederum zum Schluß, daß das Auftreten unterschiedlicher Rekonstruktionselemente (wie etwa Tetramere oder die Besetzung von Zwischengitterplätzen) bei (113)-Oberflächen stark vom Gruppe-IV-Element C, Si oder Ge abhängt. Verkippung der Tetramere oder Zwischengitteratome unterhalb der Oberfläche sind vollkommen unvorteilhaft für C(113).

Dieses Ergebnis stimmt mit den für $C(001)2 \times 1$ und $C(111)2 \times 1$ gefundenen Tendenzen überein, daß Deformationen unterhalb der Oberfläche zu energieaufwendig sind und daß zusätzliche Atome energetisch unvorteilhaft sind.

Um die treibenden Kräfte für die großen $Si(110)16 \times 2$ - und $Ge(110)16 \times 2/c(8 \times 10)$ -Rekonstruktionen zu verstehen, haben wir zunächst einige Rekonstruktionselemente in kleineren Einheitszellen untersucht, darunter verkippte Zick-Zack-Ketten, Adatome, Restatome, Dimerre, Atome auf Brückenplätzen, Tetramere, Pentamere und Atome auf Zwischengitterplätzen. Im allgemeinen stabilisieren benachbarte Ketten, die in entgegengesetzte Richtungen verkippt sind, sowie entlang der $[001]$ -Richtung angeordnete Adatome die (110) -Oberflächen. Für Germanium stellen Paare aus Adatomen und Restatomen das stabilste Rekonstruktionselement dar. Bei Silizium wird die Oberflächenenergie abgesenkt, wenn nur Adatome vorhanden sind. Reine Dimerstrukturen sowie Sättigung aller freien Bindungen durch vierfach koordinierte Adatome treten bei beiden Halbleitern nicht auf. Wir haben festgestellt, daß die Tetramer-Zwischengitterplatz(TI)-Rekonstruktion bei Si- und $Ge(110)$ -Oberflächen in Anwesenheit zusätzlicher Adatome stabilisiert wird. In diesem Fall gibt es einen Elektronentransfer von den resultierenden Pentameratomen zu den Adatomen, ähnlich wie bei (113) -Oberflächen. Freie Bindungen der Adatome sind vollständig besetzt, was – zumindest für Silizium – zu einer halbleitenden Bandstruktur führt. Berechnete STM-Bilder zeigen pentagonförmige Intensitätsverteilungen. Das Rekonstruktionselement mit zwei fünfatomigen Ringen ist energetisch vollkommen unvorteilhaft sowohl für die Si- als auch für die $Ge(110)$ -Oberfläche, obwohl diese metastabile Struktur die beiden Pentagone reproduzieren kann, die jenen Teil des Streifens im STM-Bild der unbesetzten Zustände ausmachen, der in etwa einer Einheitszelle entspricht.

Zum ersten Mal haben wir *ab-initio*-Rechnungen für die $Si(110)$ -Oberfläche mit einer 16×2 -Periodizität durchgeführt. Die zugehörige Einheitszelle umfaßt 64 Atome in jeder Lage des Volumenmaterials. Wir haben gezeigt, daß Stufen, die zu Grabenstrukturen mit oberen und unteren Terrassen führen, wichtige Rekonstruktionselemente sind. Eine geeignete Bindungsgeometrie der Stufenatome stabilisiert die $Si(110)16 \times 2$ -Oberfläche. Dies wurde anhand des adatomartigen Verhaltens der Kantenatome und entgegengesetzt verkippter Zick-Zack-Ketten auf den verschiedenen Terrassen gezeigt.

Um die in STM-Aufnahmen auf beiden Terrassenarten beobachteten Streifen in $[\bar{1}12]$ -Richtung zu modellieren, haben wir unterschiedliche Anordnungen von Adatomen untersucht. Ihre Energetik hängt empfindlich von der Verteilung der Adatome ab. Eine Anordnung der Adatome in parallelen Linien längs der $[001]$ -Richtung und im Abstand von etwa $3a_0/\sqrt{2}$ führt zu einer weiteren Absenkung der Oberflächenenergie. Eine Kombination gestreckter Hexagone aus Adatomen, umgeben von teilweise entfernten Reihen, führt zu einem lokalen Minimum der Gesamtenergiefläche, nicht aber zu einer stabilen Oberflächenrekonstruktion. Eine besonders interessante Bedeckung der Terrassen stellt ein ATI-Modell dar, das zur niedrigsten Energie aller untersuchten Geometrien führt. Diese Energie ist immer noch etwas höher als die des entsprechenden Modells einer 3×2 -Translationssymmetrie. Im Rahmen des ATI-Grabenstruktur-Modells formen vier Adatome zusammen mit einem Atom auf einem Zwischengitterplatz einen Pentamer, der wiederum mit einer unterschiedlichen Anzahl weiter Adatome kombiniert werden kann. Diese Geometrie kann durch eine Verkipfung des Pentamers verkompliziert werden. Offensichtlich können solche Pentamere zu pentagonalen Anordnungen der Intensitätsmaxima von STM-Bildern führen. Jedoch scheint ihre Ausdehnung kleiner zu sein, als es experimen-

tell beobachtet wird. Andererseits können derartige Rekonstruktionselemente auch zu Intensitätsverteilungen mit anderen Mustern führen. Ihr Auftreten hängt von der Anzahl und der Absättigung der Adatome ab. Auch Kantenatome, die Adatomcharakter haben, sowie Adatome in Bereichen, in denen Kettenatome entfernt wurden, können einen drastischen Einfluß auf die Intensitätsverteilung haben, da sie in den experimentellen STM-Bildern unbemerkt bleiben können.

Das ATI-Modell stellt einen bemerkenswerten Fortschritt zur Erklärung der Geometrie der Si(110) 16×2 -Oberfläche dar. Jedoch weisen der zugehörige Gewinn an Oberflächenenergie und die Feinstrukturen der STM-Aufnahmen darauf hin, daß das Rekonstruktionsmodell wahrscheinlich weiter verfeinert werden muß. Andererseits ist eine eindeutige Interpretation der gemessenen STM-Bilder nicht möglich. Daher sind weitere detaillierte strukturelle, spektroskopische sowie Gesamtenergieuntersuchungen erforderlich. Am meisten würden wir STM-Untersuchungen mit echter atomarer Auflösung sowohl auf der oberen als auch der unteren Terrasse, insbesondere in der Nähe der Stufenkanten, begrüßen.

Unsere *ab-initio*-Gesamtenergie- und -Elektronenstrukturergebnisse weisen auf wesentliche die Modifikation von physikalischen Ursachen für die Abhängigkeit der Rekonstruktion von der Oberflächenorientierung und der Größe der Gruppe-IV-Atome hin. Wir haben eindeutig gezeigt, daß sich das Rekonstruktionsverhalten von Diamantoberflächen einerseits und von Silizium- und Germaniumoberflächen andererseits stark unterscheidet. Adatome, Besetzung von Zwischengitterplätzen und symmetriebrechende Deformationen sind bei Diamant aufgrund der kleineren atomaren Abstände und der stärkeren Bindungen unwahrscheinlich. Jedoch treten solche Rekonstruktionselemente bei Si- und Ge-Oberflächen auf. Das komplizierte Zusammenspiel von Bindung, resultierender atomarer Geometrie und zugehöriger elektronischer Struktur wurde aufgezeigt und zur Diskussion der treibenden Kräfte der Oberflächenrekonstruktionen verwendet.

Die präzisen atomaren Anordnungen der Halbleiteroberflächen, die in dieser Arbeit erzielt wurden, sind darüberhinaus für weitere Untersuchungen erforderlich. Insbesondere sind optische Spektren der Si(113)- und Si(110)-Oberflächen wichtig, um mehr Informationen über ihre elektronische Struktur zu erhalten. Für die Beschreibung der Adsorption von Fremdatomen und Molekülen (wie zB. Biomolekülen) ist zunächst ein Verständnis der unbedeckten Oberfläche erforderlich. Eine Bedeckung von Si-Substraten mit einer oder wenigen Monolagen Ge-Atomen deutet auf das Auftreten ähnlicher Rekonstruktionselemente hin, wie etwa Dimere auf sauberen (100)- und Pentamere auf unbedeckten (113)-Oberflächen.

Die absoluten Oberflächenenergien wurden verwendet, um die Gleichgewichtsform (ECS) dreidimensionaler Kristallite sowie [111]- bzw. [100]-orientierter Pyramiden und Inseln zu beschreiben. Wir haben gezeigt, daß die ECS empfindlich von den absoluten Werten der Oberflächenenergien abhängt. Als Konsequenz haben wir eine Variation der Kristallform beim Übergang von Diamant über Silizium zu Germanium festgestellt. Wir haben vorhergesagt, daß interessanterweise {311}-Facetten an der ECS von Diamant beteiligt sind. Für Germanium wurde dagegen eine stärker sphärische Form abgeleitet. Das Auftreten von Oberflächen mit großen Indizes ist bei Germanium ebenfalls recht wahrscheinlich. Unter Vernachlässigung des Einflusses der Kanten und der Deformation haben wir allgemeine Tendenzen für die Modifikation [111]- und [100]-orientierten Pyramiden festgestellt, die sich durch Kappung, Deformation der Grund-

fläche oder Facettierung bemerkbar machen. Die Stärke der jeweiligen Deformation hängt von der Form der gesamten Pyramide sowie den Werten der Oberflächenenergie γ ab.

Acknowledgments

I would like to thank many people who helped me during my Ph.D. time in Jena:

First of all I thank my supervisor, Prof. Friedhelm Bechstedt. He always has many good ideas, which I could partially realize in the present thesis. I am really grateful to him for many discussions and, in particular, for his great ability to always be easily reachable and find time to discuss scientific as well as private issues.

I will never forget my first day in Jena, my first day abroad, when Jürgen Furthmüller, my second supervisor, picked me up at the train station and drove me to the hostel. Afterwards I realized that his fast driving and good mood is the way how he also helps in solving technical and physical problems.

Special acknowledgments are devoted to Jan-Martin Wagner for his assistance with L^AT_EX and for permanently improving my German as well English languages. I am also grateful to Jan-Martin for many consultations in the preparation for my final defence as well as the examinations.

For the good time and a lot of various discussions I would like to thank people with whom I shared the room in the institute in the different periods: Luis Ramos, Christophe Raffy, Ulrike Großner, and Andreas Zywietz. Moreover, I would like to thank our friendly and helpful group, in particular Karsten Hannewald, Hans-Christian Weißker, Peter Käckell, our system administrator Marion Fiedler, and our secretary Sylvia Hofmann.

For the great inspiration of my work I am grateful to my wife Natalja and our daughter Nastja, who was born during my Ph.D. time. A lot of power I have got from my relatives in Minsk, my friends and colleagues there. I would like to thank Prof. Victor Borisenko, Alexander Kholod, and Andrey Filonov for introducing me to the scientific world.

Finally I would like to thank the DFG for financial support of my work.

Lebenslauf

Name	Andrey Stekolnikov
Geburtstag	25. Januar 1977
Geburtsort	Minsk
Staatsangehörigkeit	Belarus
1982–1993	Allgemeinbildende Schule N53 Minsk (Klasse mit mathematischem Schwerpunkt) Abitur: June 1993
1993–1998	Studium in der Belarussischen Staatlichen Universität für Informatik und Radioelektronik (früher: Minsker Institut für Radiotechnik), Fachrichtung “Mikroelektronik”
Juni 1998	Diplom-Ingenieur (mit Auszeichnung)
1998-2000	Wissenschaftlicher Mitarbeiter im Belarussischen Staatlichen Universität für Informatik und Radioelektronik, Labor für Nanoelektronik
Seit Oktober 2000	Wissenschaftlicher Mitarbeiter am Institut für Festkörpertheorie und -optik der Friedrich-Schiller-Universität Jena

Jena, den 7. Juli 2004

Ehrenwörtliche Erklärung

Ich erkläre hiermit ehrenwörtlich, daß ich die vorliegende Arbeit selbständig, ohne unzulässige Hilfe Dritter und ohne Benutzung anderer als der angegebenen Hilfsmittel und Literatur angefertigt habe. Die aus anderen Quellen direkt oder indirekt übernommenen Daten und Konzepte sind unter Angabe der Quelle gekennzeichnet.

Bei der Auswahl und Auswertung des Materials haben mir die nachstehend aufgeführten Personen in der jeweils beschriebenen Weise unentgeltlich geholfen:

1. Prof. Dr. Friedhelm Bechstedt (als betreuender Hochschullehrer),
2. Dr. Jürgen Furthmüller (Betreuung in bezug auf die Numerik).

Weitere Personen waren an der inhaltlich-materiellen Erstellung der vorliegenden Arbeit nicht beteiligt. Insbesondere habe ich hierfür nicht die entgeltliche Hilfe von Vermittlungs- bzw. Beratungsdiensten (Promotionsberater oder andere Personen) in Anspruch genommen. Niemand hat von mir unmittelbar oder mittelbar geldwerte Leistungen für Arbeiten erhalten, die im Zusammenhang mit dem Inhalt der vorgelegten Dissertation stehen.

Die Arbeit wurde bisher weder im In- noch im Ausland in gleicher oder ähnlicher Form einer anderen Prüfungsbehörde vorgelegt.

Die geltende Promotionsordnung der Physikalisch-Astronomischen Fakultät ist mir bekannt.

Ich versichere ehrenwörtlich, daß ich nach bestem Wissen die reine Wahrheit gesagt und nichts verschwiegen habe.

Jena, den 7. Juli 2004